SULFUR-CONTAINING LIGANDS TO 3D TRANSITION METALS: SYNTHESIS, SPECTROSCOPY, AND APPLICATIONS

A Dissertation

by

CHRISTOPHER RYAN DELANEY

Submitted to the Graduate and Professional School of
Texas A&M University
in partial fulfillment of the requirements for the degree of

DOCTOR OF PHILOSOPHY

Chair of Committee,	Marcetta Y. Darensbourg
Committee Members,	Frank Raushel
	David Powers
	Vishal Gohil
Head of Department,	Simon North

December 2021

Major Subject: Chemistry

ABSTRACT

Thiolates and their metal complexes have long been central to biological and inorganic chemistry. In addition to their ability to form unidentate complexes, thiolates are well known to act as bridges between metal centers and can be readily modified by oxidation, alkylation, and acetylation, facilitating the construction of highly modified metal complexes. The work described here focuses on the utility of thiolate-based ligands to serve as a platform for investigations into the solution-phase properties of nickel complexes, as well as the inhibition of SARS-CoV-2 by metal-thiolates.

While molecular structures obtained via X-ray Diffraction (XRD) are often the benchmark for inorganic structural determination, other techniques can offer insights not readily available in the solid-state. Various synthetic routes to a self-assembled tetrameric nickel cage with carboxylate linkages, $[Ni(N_2S'O)I(CH_3CN)]_4{}^0$, $[\mathbf{Ni\text{-}I}]_4{}^0$, were explored with the differences between the solid state and solution-phase aggregation investigated. In each case, hexacoordinate nickel units ligated by N_2S-thioether, iodide, and two carboxylate oxygens, one of which is the bridge from the adjacent nickel unit in $[\mathbf{Ni\text{-}I}]_4{}^0$, were observed in the molecular structure. In solution however, there is dissociation into (presumed) monomers with coordinating solvents occupying the 6th coordination site $[Ni(N_2S'O)I(solv)]^0$, $[\mathbf{Ni\text{-}I}]^0$. Hydrodynamic radii (r_H) determined from ^{1}H DOSY NMR data supports this hypothesis, with the r_H in both D_2O and CD_2Cl_2 matching that of a monomeric unit from the tetrameric solid-state structure. These studies point to the importance of using techniques such as DOSY to interrogate the solution-phase properties of inorganic complexes that may be unavailable in the solid state.

Numerous organic molecules are known to inhibit the main protease of SARS-CoV-2, ($SC2M^{pro}$), a key component in viral replication of the 2019 novel coronavirus. We explore the hypothesis that zinc ions, *long used as a medicinal supplement and known to support immune function*, bind to the $SC2M^{pro}$ enzyme in combination with lipophilic tropolone and thiotropolone ligands, **L**, block sub-

strate docking, and inhibit function. This study combines synthetic inorganic chemistry, in vitro protease activity assays, and computational modeling. While the ligands themselves have half maximal inhibition concentrations, IC_{50}, for $SC2M^{pro}$ in the 8-34 μM range, the IC_{50} values are ca. 100 nM for $Zn(NO_3)_2$ which are further enhanced in Zn-**L** combinations (59-97 nM). Isolation of the $Zn(\mathbf{L})_2$ binary complexes and characterization of their ability to undergo ligand displacement is the basis for computational modeling of the chemical features of the enzyme inhibition. Blind docking onto the $SC2M^{pro}$ enzyme surface using a modified Autodock4 protocol found preferential binding into the active site pocket. Such Zn-**L** combinations orient so as to permit dative bonding of $Zn(\mathbf{L})^+$ to basic active site residues.

With the emergence of new variants of SARS-CoV-2 that have been shown to have increased virulence, the search for effective inhibitors remains a priority. Expanding on our previous work, other first row transition metals (Fe-Cu) and their complexes with L are compared to that of $Zn(\mathbf{L})_2$, known inhibitors of $SC2M^{pro}$ in an effort to identify potential therapeutics. It was determined that none of the other metals, neither as MCl_x salts (K_i values between ca. 170 - 640 μM), nor as complexes with **L** (K_i's ca. 30 - 75 μM), provide the same level of inhibition as $Zn(\mathbf{L})_2$ (K_i values ca. 430 - 900 nM). The effects of changing coordination environment around Zn^{II} are also explored, with a 2S dithiotropolone ligand (**L4**) being compared with the previously investigated SO-donor thiotropolones. Here, the additional S-donor results in poorer inhibitory activity for the $Zn(\mathbf{L4})_2$ complex (K_i ca. 41 μM). Native Mass Spectrometry studies point to formation of $Zn(\mathbf{L})$-$SC2M^{pro}$ adducts as a potential mode of inhibition.

DEDICATION

To my mother and father, Patricia Kinch DeLaney and Scott DeLaney Sr., this would have never happened without out you. No matter what life has thrown as me, I have always considered myself fortunate to be called your son. To my brothers, Ryan and Scott DeLaney Jr., you were my anchors through some of the darkest portions of my life. Finally, to my grandmother Sally Kinch. Your will and spirit are a boundless source of inspiration for me.

ACKNOWLEDGMENTS

I would like to thank my advisor, Dr. Marcetta Y. Darensbourg, for giving my graduate education a second life by giving me the chance to work in her lab. I would also like to thank her for all the input she has given me over the years; it has helped me grow as a scientist and person. Finally, I would like to thank her for giving me the opportunity to work on the SARS-CoV-2 project despite my prior struggles. It has opened so many doors for me and wouldn't have been possible without her belief in my potential as a researcher. In the same vein, I would like to thank my lab mates past and present for all the constructive criticism, experiment ideas, and support. In particular, seeing Trung, Kyle, and Manuel every weekend in lab was heartening while we all worked towards our doctorates. Finally, to my two longest tenured lab mates, Dr. D. Chase Pectol, and Dr. Xuemei Yang, thank you for sharing this experience with me. We made it!

I would be remiss if I did not acknowledge my committee members, Dr. David Powers, Dr. Vishal Gohil, and Dr. Frank Raushel. Thank you for your input during my prelim, for challenging me to think more critically, and the contributions you have each made to my intellectual growth. I would also like to thank my collaborators, Dr. Wenshe R. Liu, Dr. Carol A. Fierke, Dr. Thomas Meek, Dr. Aurthur Laganowsky, and each of their respective students for facilitating the pursuit of our shared SARS-CoV-2 projects. In particular, I would like to thank Dr. Meek for giving me the opportunity to work in his lab alongside Jiyun Zhu. The two of you were incredible to collaborate with and I am so fortunate to have been able to learn under your guidance. Finally, I would like to thank Dr. Edward Lee for being an excellent teaching mentor during my time here at Texas A&M.

I would also like to thank a few specific teachers I have had at different points during my education. Mrs. Pesek, thank you for not letting me off the hook for things. I needed a little focus in my life. Ms. Mechling, you piqued my curiosity in the sciences. They continue to enthrall me. Mrs. Cook, the joy you brought to teaching was infectious. You made chemistry exciting and remain one of the main reasons I chose to pursue this degree. To my undergraduate Chemistry/Biology professors, Dr. Rose Clark, Dr. Balzas Hargittai, Dr. Justin Merry, Dr. Pedro

Muiño, Dr.Susan Reimer, Dr. John Trimble, and Dr. Edward Zovinka, thank you for making undergraduate experience so rewarding. You each contributed to my decision to undertake this intellectual journey and I hope to one day return to Saint Francis to present my research.

Thank you to the friends I have made here. There are so many I would like to thank but hopefully I can do it in person and not just in text. I would like to acknowledge some members of my cohort Dr. David Parobek, Dr. D. Chase Pectol, Dr. Jeremy Willman, Dr. Christopher Mallis, Dr. Jordon Benzie, Andrew Jefferies, Dr. Drew Harding, Richard Caranza, and Dr. Adam Kabza. From intellectual conversations over a beer to incoherent yelling over video games, you have all made this experience memorable despite the challenges we each faced. I would specifically like to thank Dr. David Parobek for helping me find gainful employment and for getting up at the crack of dawn 3 mornings a week with me for years to lift weights in absolute silence. I would also like to give a shout out to Dr. Adam Kabza and his partner Gayle Bornovski for having my back through a particularly difficult stretch in my life. It is one of the kindest things anyone has ever done for me, bar none. From the bottom of my heart, thank you. I would also like to thank my friends back on the east coast, specifically Richard Somiari, Kyle Penney, and Christopher Mills for keeping me sane and grounded. I look forward to having more time and money to see each of you. Finally, I would like to thank my ever-faithful dog, Bubba for his relentless tail-wagging and strange noises. You brought my life levity and never ceased to amuse me.

Finally, I would like to thank my family: Grandma, Mom, Dad, Ryan and Scotty. None of this would have been possible without your endless encouragement and love. From late night emergency room visits to early morning phone calls you have supported me the entire way through this process, going back to long before I ever decided I wanted to be a chemist or put Dr. in front of my name. I love you.

CONTRIBUTORS AND FUNDING SOURCES

Contributors

This work was supported by a thesis committee consisting of Professor Marcetta Y. Darensbourg (advisor), Professor Frank M. Raushel, Assistant Professor David Powers of the Department of Chemistry, and Professor Vishal M. Gohil of the Department of Biochemistry & Biophysics.

The data collection and analyses depicted in Chapter III were conducted in part by Yan Sheng, Dr. D. Chase Pectol, Dr. Erol Vantansever, Dr. Wenshe R. Liu of the Texas A&M Department of Chemistry, and Dr. Carol A. Fierke of the Brandeis University Department of Biochemistry. They were published in (2021) in an article listed in the Biographical Sketch. The data collection and analyses depicted in Chapter IV were conducted in part by Dr. D. Chase Pectol, Jiyun Zhu, Yun Zhu, Dr. Aurthur Laganowsky and Dr. Thomas D. Meek of the Department of Biochemistry & Biophysics and were incorportated into a manuscript that is currently under preparation. The data collection and analyses depicted in Chapter V were conducted in part by Dr. Xuemei Yang, Kyle Burns, and Dr. Lindy C. Elrod. They were published in (2021) in an article listed in the Biographical Sketch. I would also like to thank Dr. Yohannes H. Rezenom for the mass spectrometric data collection and analysis as well as Dr. Gregory P. Wylie and Dr. Doug Elliott for assistance with nuclear magnetic resonance experiments.

All other work conducted for the thesis (or) dissertation was completed by the student independently.

Funding Sources

Graduate study was financially supported by the R.A. Welch Foundation Grant A-0924.

NOMENCLATURE

Tosyl-**L1**	7-Oxocyclohepta-1,3,5-trien-1-yl 4-methylbenzenesulfonate
Tosyl-**L2**	4-(1-Methylethyl)-2-[[(4-methylphenyl)sulfonyl]oxy]-2,4,6-cycloheptatrien-1-one
Tosyl-**L3**	6-(1-Methylethyl)-2-[[(4-methylphenyl)sulfonyl]oxy]-2,4,6-cycloheptatrien-1-one
L1	2-hydroxyl-cyclohepta-2,4,6-triene-1-thione
L2	7-Hydroxy-3-isopropylcyclohepta-2,4,5-triene-1-thione
L3	2-Hydroxy-4-isopropylcyclohepta-2,4,6-triene-1-thione
L4	2-mercaptocycloheptatrienethione
MeOH	Methanol
MeCN	Acetonitrile
ET_2O	diethyl ether
DCM	Dichloromethane
$CHCl_3$	Chloroform
$CDCl_3$	Chloroform-D
DMSO	Dimethyl sulfoxide
IC_{50}	50% inhibitory concentration
K_i	Inhibition Constant
EC_{50}	half maximal effective concentration
N_2SH	1-(2-mercaptoethyl)-methyl-1,4-diazacycloheptane
DNIC	Dinitrosyl Iron Complex
TGTA	1-thio-β-d-glucose tetraacetate
TG	1-thio-β-d-glucose

trop	tropolone
HK	hinokitiol
AD4	Autodock4
PT	pyrithione
RRE	Roussin's Red Ester
bipy	2,2′-bipyridine
CO	carbon monoxide
NO	nitric oxide
TDT	1,2-toluenedithiolate
IR	Infrared Spectroscopy
NMR	Nuclear Magnetic Resonance
MS	Mass Spectrometry
ESI	Electrospry Ionization
ACPI	Atmospheric Pressure Chemical Ionization
UV-Vis	Ultraviolet-Visible spectroscopy
BSA	Bovine Serum Albumin
EA	Elemental Analysis
XRD	X-ray Diffraction
Da	Dalton
PDB	Protein database
HIV	human immunodeficiency virus
SC2	SARS-CoV-2
SC1	SARS-CoV-1
$SC2M^{pro}$	main protease of SARS-CoV-2
$SC1M^{pro}$	main protease of SARS-CoV-1

RdRp	RNA-dependent RNA polymerase
PL^{pro}	Papain-like protease
DMT1	divalent metal transporter 1
MFRN1	mitochondrial iron import protein mitoferrin
hCA	human carbonic anhydrase
HDAC	histone deacetylase
MBP	metal binding pharmacophores
MDRB	multidrug-resistant bacteria
MRSA	Methicillin-resistant Staphylococcus

TABLE OF CONTENTS

Page

LIST OF FIGURES

FIGURE Page

LIST OF TABLES

TABLE Page

1. INTRODUCTION

1.1 Thiolates and Their Metal Complexes

The contents of this dissertation will be divided into two sections, both centered around the use of thiolate ligands to modulate the properties of metal complexes. The first section will discuss the investigation of thiolated tropolone ligands for the inhibition of the main protease of SAR-CoV-2, an important target in the viral replication cycle of the infectious agent at the center of the ongoing pandemic.[1] My work has led to an initial publication, described in Chapter III, examining the use of Zn-thiotropolone complexes as inhibitors of the main protease of SARS-CoV-2.[2] In follow-up work, given in Chapter IV, the potential mechanism of this inhibition along with its applicability in infected cells is addressed. The second section will focus on the acetylation of thiolates in nickel coordination complexes which results in unique solution phase and solid state properties that were investigated using Diffusion Ordered Spectroscopy (DOSY) NMR, highlighted in Chapter V.[3] Finally, Chapter VI provides a brief summary of my work followed by a perspective that explores further potential applications of these results.

Sulfur containing thiolate ligands are ubiquitous, both in natural and synthetic systems. Thiolates have numerous properties that make them desirable ligands to metal centers. They are soft Lewis bases, allowing them to form strong dative bonds, especially with soft Lewis acids such as Copper ($Cu^{I/II}$), molybdenum (Mo) in various redox levels and most critically for this dissertation, Zinc (Zn^{II}) and Nickel (Ni^{II}).[4, 5] Thiolates can act as sulfur bridges between multiple metal centers, facilitating the construction of bi- and multi-metallic species.[6] Nature exploits this to great effect in the construction of enzyme active sites. These include Diiron hydrogenase, Nickel-iron hydrogenase, and Acetyl-CoA synthase.[5] There are 9 known Ni-containing enzymes, the majority of which include Cysteinyl thiolates as ligands. These will be described in greater detail in the second section of my disertation.

While the number of Ni-containing proteins to this point appears to be limited, Zn is ubiquitous

in the proteome.[7]. In fact, somewhere between 4 and 10% of all proteins contain a Zn-binding domain. The thiophilicity of Zn means that many proteins use thiolates to bind the metal as is seen in the structural motif known as a zinc finger. Zinc fingers provide stability to the protein and are found in numerous eukaryotic transcription factors.[8, 9] In these proteins the most commonly encountered coordination environments are depicted in **Figure 1.1**, and include (**A**) $Zn(Cys\text{-}S)_4$, (**B**) $Zn(His\text{-}N)_2(Cys\text{-}S)_2$, and (**C**) $Zn_2(Cys\text{-}S)_6$. Cysteine is present in each case, an illustration of how critical thiolates are to Zn-containing proteins.[8] Because of the prevalence of Zn is in the proteome, it has begun to attract attention as a therapeutic target. By chelating out zinc, the structure and function of many critical bacterial,[10] oncological,[11] and viral[12] proteins can be abrogated. The utility of such approaches along with specific examples will be discussed in greater detail in coming sections.

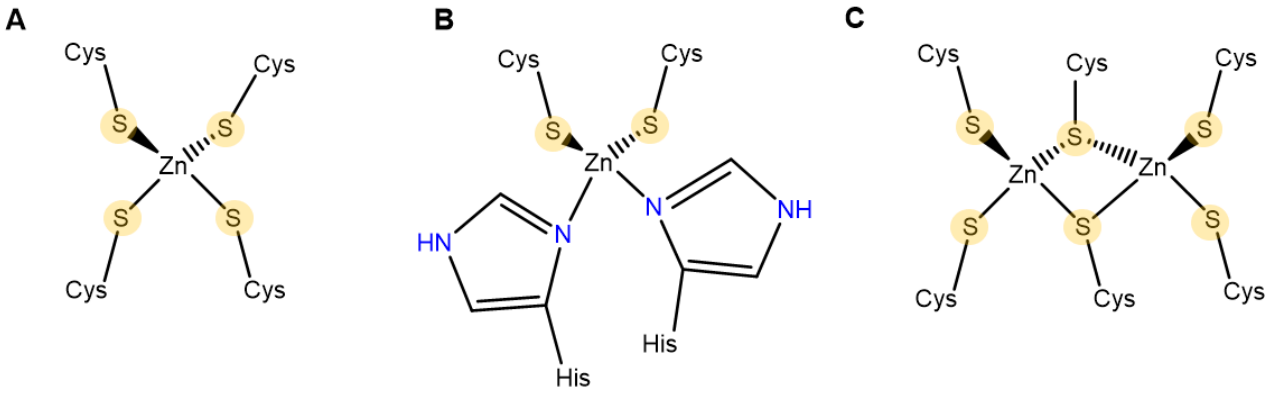

Figure 1.1: ChemDraw representations of the thiol-containing primary coordination spheres of Zinc-finger proteins. The most commonly encountered motifs, (**A**) $Zn(Cys\text{-}S)_4$, (**B**) $Zn(His\text{-}N)_2(Cys\text{-}S)_2$, and (**C**) $Zn_2(Cys\text{-}S)_6$, each containing cysteinyl thiolates.

The redox levels associated with S-donors also contribute to their versatility, including non-innocence in certain cases. Thiolates also readily undergo chemical modification such as oxygenation, methylation, and acetylation.[13, 14] These modifications, such as the oxygenation to sulfenic and sulfinic donors observed at the active-site of the Fe-containing Nitrile Hydratase,[15, 16, 17,

18] serve as another means to tune the ligand environment around the metal. In doing so the donor ability of the ligand field is modulated, altering the reactivity of the resulting complexes. Given the breadth of properties that thiolates can confer to the metals they bind to, they serve as an excellent platform for synthetic chemistry investigations.

1.2 Tropolones

1.2.1 History of Tropolones

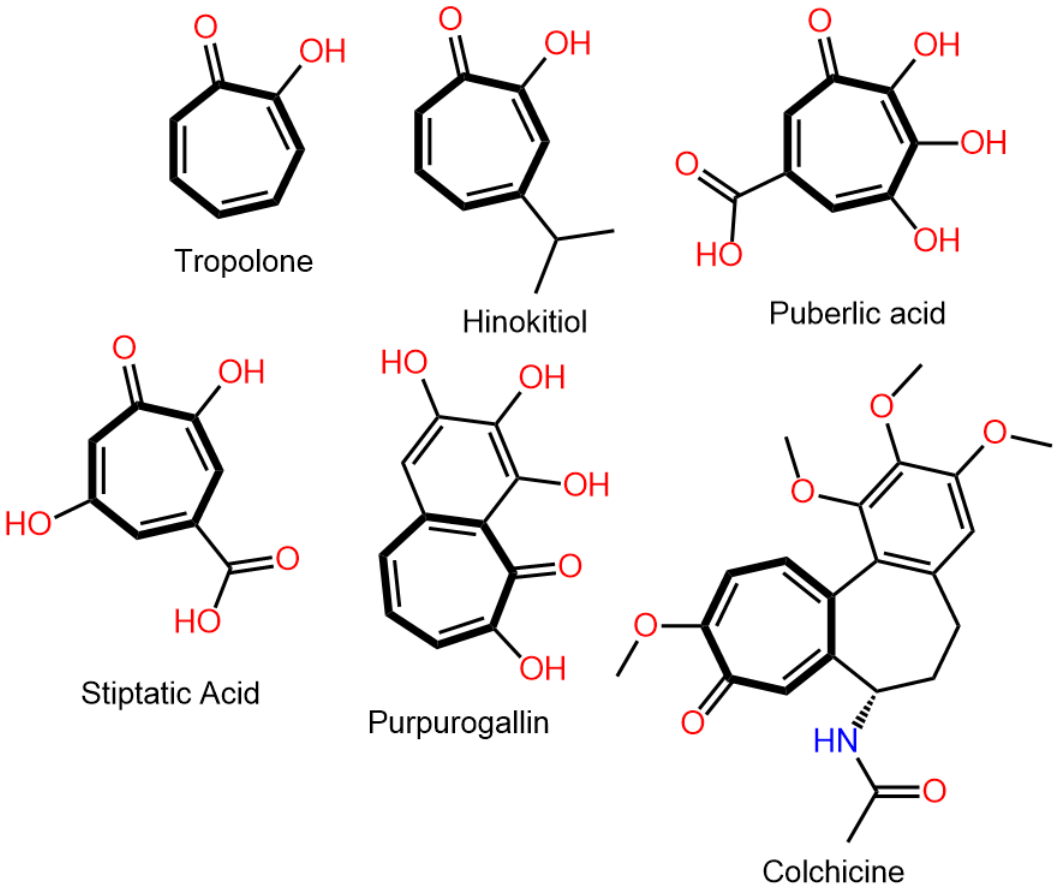

Figure 1.2: Selection of troponoid natural products with the seven-membered ring core structures highlighted.

The first reported troponoid, purpurogallin, was synthesized in 1869 by Girard with the chem-

ical formula $C_{11}H_8O_5$ **Figure 1.2**.[19] The arrangement of atoms in purpurogallin however was not immediately clear and would remain unsolved for some time. Nearly 60 years later, the first tropolonoid natural products, puberulonic acid and puberluric acid, were isolated from the fungi Penicillium puberlumum in 1932.[20] In the following decade, a number of other troponoids such hinokitiol (HK)[21] and stipitatic acid[22] were isolated from natural souces. However, the structure of these compounds remained elusive. It was not until 1945 that the aromatic seven-membered 2-hydroxy-2,4,6-cycloheptatrien-1-one or tropolone (trop) core structure common to all of these compounds was proposed by Michael Dewar.[23] It was this realization that also allowed Dewar to correctly surmise the make-up of colchicine, a troponoid natural product that has been used medicinally since antiquity and was first isolated in 1820.[24] Dewar coined the term "tropolone" to describe this seven-membered non-benzoid aromatic configuration, the core structure of which is highlighted in each of the molecules depicted in **Figure 1.2**. It should be noted that Tetsuo Nozoe, one of the pioneers of troponoid chemistry, purportedly proposed a similar seven-membered ring in 1941 following his isolation of HK. However the interruption in scientific communication between the allied and axis powers caused by World War II meant knowledge of this was largely confined to his immediate colleagues in Japan.[25] The antimicrobial properties of these compounds, first observed in HK in 1948, further cemented their importance.[26] This flurry of activity resulted in the synthesis and characterization of the parent compound, trop, in 1950 by three groups.[27, 28] By the time a comprehensive review on these compounds was written in 1955, it required nearly 500 references to encompass the expansion of the literature pertaining to troponoids and their derivatives.[25] Today, over 200 tropolonoid natural products have been identified and the libraries of their synthetic derivatives continues to grow.[29]

1.2.2 Properties of Tropolones

Tropolones have a number of unique properties that drove the initial boom in research interest surrounding them; they are often compared to another group of aromatic acids, phenols. As mentioned previously, tropolones provided the first examples of non-benzoid aromaticity and expanded the way organic chemists viewed aromaticity. In its protonated state, trop exists as two

tautomers, with the proton being shared equally between the two oxygens.[30, 31] X-ray crystallography studies show that the C-C bonds within the C_7 ring have nearly equivalent bond distances at ca. 1.40 Å and identical C-O bonds.[32, 33, 34] This results in tropolone being significantly more acidic (pH ca. 7 in H_2O) than phenol (pH ca. 10) as deprotonation results in a 10 π-electron system that satisifes Hückel's 4n+2 rule.[35] This aromaticity results in substitutional chemistry that is very simlar to phenols, although tropolones generally undergo di-substitution when exposed to eletrophilic reagents such as bromine while phenolic compounds become tri-substituted.[25, 36]

Just as observed with phenols, tropolones are known to form a wide array of complexes with metal ions. Coordination complexes of tropolones with transition metals are prominent in the literature, forming both chelate and π-complexes.[37, 36] In fact, HK was first isolated from the heartwood of *Chamaecyparis taiwanensis* (Taiwan Hinoki) tree as a ferric-iron complex of formula $Fe(C_{10}H_{11}O_2)_3$.[21] This ability to bind metals is one of the key features of tropolones and is of import to their medicinal properties. These will be covered in greater detail in coming sections. Reaction chemistry of the heteroatoms also features prominently, with one or both of the O-atoms being replaced by halogens,[38], amines,[39, 40] alkoxides,[41] and thiolates[42, 43, 40, 41, 44] allowing for the generation of numerous unique chelates that continue to draw attention today.[45, 46, 47]

1.2.3 Metal Complexes of Tropolone and its Derivatives

In the mid 1960's, the ability of trop to form stable complexes with main group elements,RN357 transition metals,[48] lanthanides,[49] and actinides[50] was explored in great detail in a series of papers by E.L. Muetterties *et al*. The bidentate nature of trop coupled with its planarity allowed Muetterties to achieve ten-coordinate complexes with thorium and uranium, a feat that had been first reported by M.D. Lind and coworkers in 1965.[51] In this series of reports, Muetterties and coworkers also began to explore the effects of altering the donor atoms present on the tropolones, such as aminotroponimine an N-N chelate.[39] This work culminated in a study where derivatives with O-N, S-O, and S-N were synthesized then compared and contrasted.[40] The S-O chelate, known as 2-mercaptotropone or thiotropolone, was first synthesized in 1953 by Nozoe

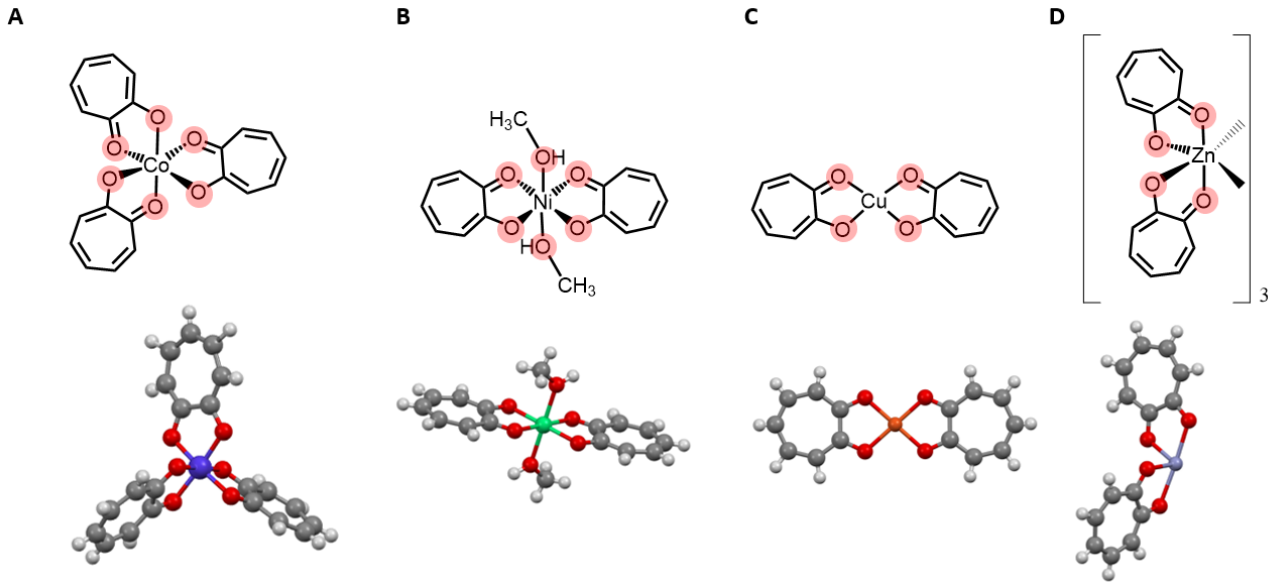

Figure 1.3: Molecular structures as determined by XRD of first-row transition metals and tropolone as follows: Cobalt (**A**), Nickel (**B**), Copper (**C**), and Zinc (**D**). ChemDraws with primary coordination sphere highlighted depicted above for clarity. Crystal structures generated using Mercury.

and coworkers,[42] and will be explored in greater detail in coming sections due to its biological activity is of interest, particularly in combination with metals.[46, 52, 53] The S-S chelate, dithiotropolone, along with metal complexes of the ligand and Ni^{II}, Pt^{II}, Pd^{II}, Zn^{II}, and Cd^{II} were reported in 1968 by C.E. Forbes and R.H. Holm.[41] Following this initial effort, a much more extensive investigation of the properties of the S-S ligand and its complexes with divalent metals was published in 1970.[44] This S-S ligand was compared and contrasted to another class of dithiolate-containing ligands that were garnering significant attention at the time, dithiolenes.[54]

Dithiolene-metal complexes display a high degree of covalency between metal and ligand in addition to their redox non-innocence.[55] In comparing the properties of these two, it was found that the metal-dithiotropolones were not reduced as easily as the analogous dithiolenes, generally having reduction potentials 0.2-0.8 V more negative than their counterparts. In addition, these reductions were less likely to be reversible than those observed in dithiolenes. Meanwhile molecular structures, determined by X-Ray Diffraction (XRD), of the first row transition metals (Sc, Mn-Zn) complexed to trop have been reported. A selection of these are given in

Figure 1.3.[56, 57, 58, 59, 60, 61, 62, 63, 64] The crystal structures of a number of heavier elements[65, 66, 67] along with complexes of other tropolones such as HK[68, 69, 64, 70] continue to be added. Relatively speaking however, there are far fewer reports of the full characterization of modified tropolones and their complexes.[39, 71, 41, 44] These structures are of interest as metal-tropolone combinations have been shown to be a means of importing metals into the cell, a process that will be discussed in greater detail in coming sections. The isolation and characterization of some of these complexes was a major aim of my studies.

1.3 Medicinal Applications of Tropolones

1.3.1 Tropolones as Chelates

While initial interest in tropolones was sparked by their unique chemistry and properties, it is the medicinal properties of these compounds that continues to drive research. Since the initial report of the antimicrobial activity of HK in 1948,[26] numerous tropolone derivatives have been found to inhibit bacterial growth.[53, 72] The emergence of multidrug-resistant bacteria (MDRB), such as the infamous Methicillin-resistant Staphylococcus aureus (MRSA), continues to motivate identification of new antibiotics that combat such MDRB.[73] Work by Cao *et al.* demonstrates the utility of tropolone derivatives for this, with troponoids displaying activity against *Staphylococcus aureus*, *Escherichia coli*, *Acinetobacter baumannii*, and *Pseudomonas aeruginosa*.[52] The results for *S. aureus* were particuarly promising, with two of the lead compounds inhibiting 18 different MRSA strains. One of the key ways in which tropolones act in this capacity is via chelation and extraction of ions out of metalloproteins. An excellent example of this is anthrax lethal factor, a zinc-containing metalloprotein from the pathogenic *Bacillus anthracis* which has been shown to be critical to lethality.[74] In screenings of potential inhibitors by Cohen *et al.*, troplone was found to inhibit this metalloprotease with 50% inhibitory concentration (IC_{50}) values of ca. 300 μM.[75]

Beyond the antimicrobial properties of tropolone and its derivatives, they have also been found to show activity as antifungal, antiviral, and antiproliferative agents. Mushroom tyrosinase, a di-copper enzyme that catalyzes the conversion of phenolic compounds to the corresponding quinones,

is also inhibited by tropolone.[76, 77] This enzyme is responsible for food browning and is the target of many antifungals added to consumer products. Surprisingly, this inhibition does not appear to occur via chelation of the Cu out of the enzyme active site, but rather by formation of a pre-Michaelis complex with the enzyme as seen in the crystal structure of tropolone-bound tyrosinase from *Agaricus bisporus*.[76]

Tropolones have displayed antiviral activity against a number of infections,[78] such as human immunodeficiency virus (HIV),[79] hepatitis[80], and herpes simplex virus.[81] Studies on HIV focused on the action of α-hydroxy tropolones against two Mg^{2+}-dependent enzymes that drive virulence, reverse transcriptase (RT) and integrase (IN). *In vitro* studies on RT and IN gave IC_{50} values as low as 570 nM and 250 nM respectively for these α-hydroxy tropolone derivatives. Blocking of the chelate by addition of a methyl-group to the O-donors abolishes inhibition, pointing to the importance of chelation for antiviral activity in this system. Inhibition of viral replication *in vivo* was also observed, though the applicability of these compounds is hampered by cytotoxicity in the cell lines tested. This ability to chelate Mg^{2+} is a common thread among these viral studies.[78]

One of the largest growth fields in tropolone research over the past two decades is investigations into their antiproliferative activity. This function stems in part from their ability to inhibit a class of proteins known as histone deacetylases (HDACs).[82] There are a number HDAC isozymes within the cell, with class subdivisions indicating their respective molecular targets. These enzymes catalyze the removal of acetyl groups from lysine residues present on histones, impacting the structure of the chromatin and thus accessibility of the DNA associated with it. Given that the acetylation level of histones is one of the primary ways in which gene expression is modulated,[83] aberrant HDAC activity can lead to the emergence of cancer. In class I and II HDACs, this deacetylation activity requires a catalytic zinc ion. A proposed mechanism for this can be seen in **Figure 1.4**, where Zn^{II} activates water towards nucleophillic attack on the ketone carbon of the acetylated-lysine residue. Removal of zinc from the active site deactivates HDAC, meaning metal chelates that can effectively associate with the active site and bind Zn^{II} are attractive targets for the development of novel therapeutics. Numerous chelates have been investigated for HDAC inhibition,

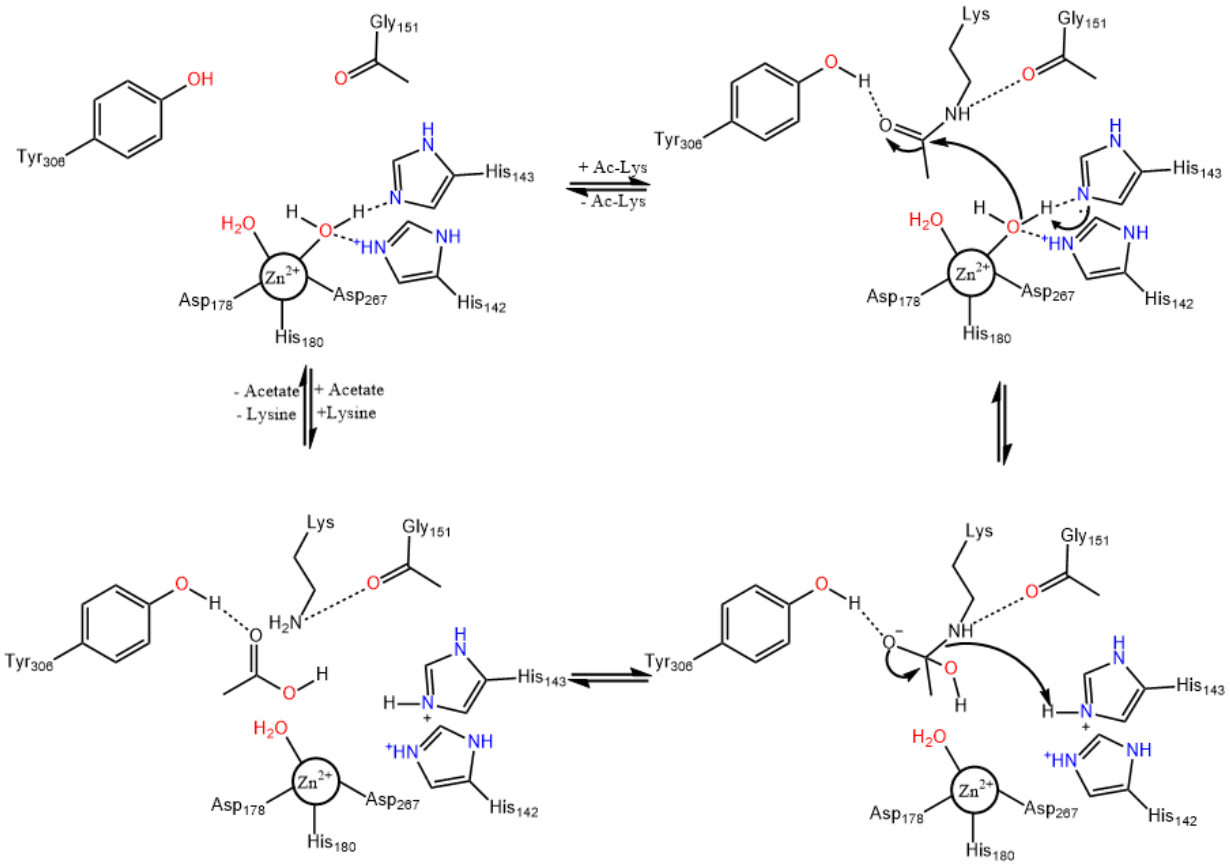

Figure 1.4: Proposed reaction mechanism of the Histone Deacetylase 8 isozyme with pertinent residues labeled. Reaction proceeds by Lewis acidic activation of water by Zn^{2+} on acetylated lysine, followed by collapse of the tetrahedral intermediate, and subsequent elimination of acetate. Dissociation of reaction products, lysine and acetate, completes the cycle. Loss of Zn^{2+} from this site inactivates the enzyme.

with tropolone derivatives displaying particular promise.[82] Starting with a set of 12 compounds, Ononye *et al.* investigated the efficacy of these substituted tropolones against six different HDAC isozymes. Seven of them were found to be potent inhibitors of the target isozyme, HDAC2, with a high degree of selectivity for it versus the other HDACs. The most efficacious of these was found to have an IC_{50} of 0.04 nM. As with previous studies, blocking one of the O-chelates by methylation abolished inhibition. Computational docking studies using Surflex-Dock found that the tropolones associated favorably with the Zn-containing active site, with the O-donors well positioned to bind

to the Zn ion. These compounds were then examined for their ability to inhibit growth of various cancer cell lines, with select derivatives achieving half maximal growth inhibition values in the μM range.

Human Carbonic anhydrases (hCAs) are another target for tropolone anticancer therapeutics.[84] They catalyze the interconversion of CO_2 and HCO_3^- and play a pivotal role in the maintenance of cellular pH balance. Of the 15 isozymes, 12 are known to require a zinc ion for activity. This makes them an attractive target for the design of metal binding pharmacophores (MBPs) such as tropolones.[11] In work by Cohen *et al.* in 2017 three MBPs, tropolone, thiotropolone, and 1-hydroxypyridine-2(1H)-thione were compared for inhibition of the hCAII isozyme,[11] a target of cancer therapeutics that is often upregulated in highly tumorigenic breast cancer cells.[85] It was found that replacement of one of the O-donors of tropolone with an S-donor in 2-mercaptotropone dramatically improved inhibition, dropping the IC_{50} from ca. 1350 μM in the 2-O tropolone to ca. 100 μM for the S-O 2-mercaptotropone. The authors attribute this improvement to the known thiophilicity of Zn^{II},[4] as well as the greater tolerance for non-ideal metal-ligand bond angles in S-donors when compared to O-donors. Taken together, these studies demonstrate the potential of chelates like tropolones to inhibit or inactivate medicinally relevant metalloproteins. They also point to the importance of ligand selectivity and affinity when working in complex biological systems.

1.3.2 Tropolones as Ionophores

Beyond chelating metals out of proteins, tropolones have also been investigated for their ability to bring metals into the cell. Ligands that bind metals and facilitate their transfer across lipid membranes are known as ionophores, and many tropolones display this property. Metal-tropolone combinations, as separate components or intact complexes, have shown promise as antianemic,[70] antiviral,[86] anticancer,[87, 88] antimicrobial,[68] and antidiabetic therapies[46] due in part to the lipophilicity they engender.

An excellent example of this can be found in work published in 2017 by Grillo *et al.* which demonstrated the utility of HK to increase intracellular iron concentrations in organisms with aber-

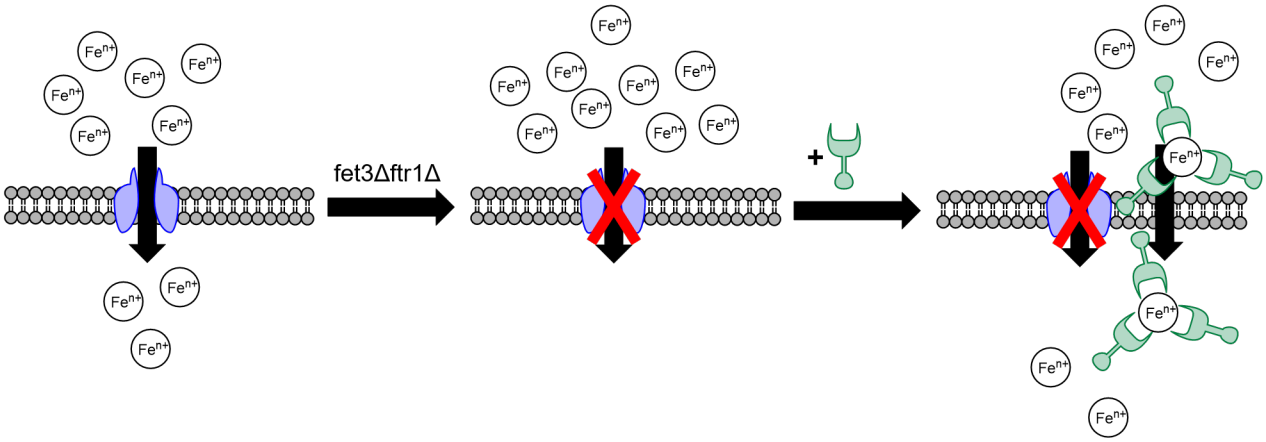

Figure 1.5: (Left) In wild-type *S. cerevisiae* iron (represented as Fe^{n+}) import is carried out by the iron-transporting complex Fet3Ftr1 represented in blue. (Center) In the iron-transporting complex deficient (fet3Δfrt1Δ) mutants, this pathway is no longer operative. Iron cannot enter the cell, resulting in diminished growth or lethality. (Right) When the fet3Δfrt1Δ cells are grown in media supplemented with hinokitiol (HK), represented in green, this lethal phenotype is rescued. Fe-transport is restored by HK binding to the metal ion and promoting its diffusion through the cell membrane and into the cytoplasm. Figure adapted from Grillo *et al* ref. 70.

rant import pathways, and promote the transport of iron between different organelles within the cell.[70] In each these organisms, the hydrophillic iron ions were unable to diffuse through cellular membranes in the absence of critical iron transport proteins. Deletions of the genes associated with the iron-transporting complex Fet3Ftr1, a fet3Δfrt1Δ mutant, resulted in deleterious, sometimes lethal iron deficiencies in *Saccharomyces cerevisiae*. However, when the media that *S. cerevisiae* was cultured on was supplemented with HK, [Fe] within the cell rose and the fatal phenotype was rescued. Tracking iron import using ^{55}Fe content of cells in the presence and absence of HK, it was found that supplementation with HK restored Fe-content to near wild-type levels for the fet3Δfrt1Δ cells. The proposed mechanism for this observed activity is shown in **Figure 1.5**. Investigation of the solution-phase properties confirmed that Fe forms a 1:3 complex with HK, $[Fe(HK)_3]^0$, with binding of Fe^{3+} to HK substantially increasing its lipophilicity as determined by partitioning experiments. This strategy was also effective to restoring Fe-transport within the cell, rescuing a lethal mutation to a mitochondrial iron import protein mitoferrin (MFRN1). This result was extended to multicellular organisms, with HK supplementation improving gut absorption of Fe

in both divalent metal transporter 1- (DMT1-) deficient rats as well as ferreportin-deficient mice. Finally, HK was found to restore hemoglobinization in DMT1- and MFRN1-deficient zebrafish. Taken together, these results point to the ability of HK and other tropolones to use concentration gradients to promote the diffusion of cations across otherwise impermeably hydrophobic membranes. This activity is abolished if one of the 2 O-atom donors of the chelate is removed/blocked and points to the importance of ligand affinity for Fe in this application.

In an earlier study on the effect of Zn^{2+} on viral infections by Krenn *et al*. it was found that ionophores, such as HK, improve antiviral activity when administered alongside Zn^{II} relative to simple metal salts alone for three different infections: human rhinovirus, coxsackievirus, and mengovirus.[89] As was the case with the previous study, this effect depends on the ability of the ionophore to increase intracellular metal concentrations. All three ionophores tested were shown to increase the intracellular ^{65}Zn concentration in radiometric measurements. It is noteworthy that of the three ionophores investigated HK actually performed the poorest, requiring the highest concentration of added ionophore needed to achieve the increase in cellular ^{65}Zn levels required for antiviral activity. This was attributed to the higher affinity of pyrrolidine-dithiocarbamate and pyrithone (PT) for Zn^{II}.[89] Again, this study points to the importance of ligand affinity for the target metal to maximize the desired effect.

In situ formation of metal-tropolone complexes isn't the only means of achieving efficacy however. Intact complexes also display biological activity. An excellent example of this is the use of Zn-ionophore complexes as therapuetics for diabetes. Zinc has long been known to have insulin-mimetic effects.[90] This effect is further enhanced when administering Zn as a complex with ionophoric ligands, such as HK, when compared to Zn salts alone.[91, 92] Selection of the appropriate ligand scaffold for this purpose is critical for maximizing efficacy, as changes to both the primary coordination sphere,[93, 94, 46] and the backbone groups of the ligands have been shown to have a marked effect on the activity of the resulting complex.[46, 95, 93] This effect is in part due to the ability of ionophores like tropolone to increase the lipophilicity of Zn. A study by Murakami *et al*. in 2012 compared the anti-diabetic activity of six Zn-bistropolonato complexes,

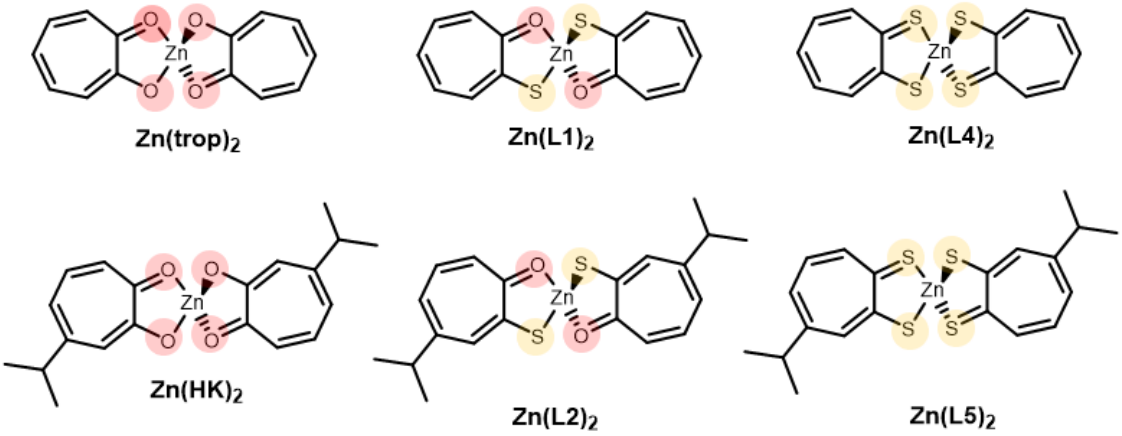

Figure 1.6: Structures of the six Zn-bistropolonato complexes investigated by Murakami *et al*. for their antidiabetic activity. The most effective, Zn(**L1**)$_2$, posses and S2O2 coordination mode.

Zn(trop)$_2$, Zn(HK)$_2$, and their thiolated derivatives Zn(**L**)$_2$; the structures of these are displayed in **Figure 1.6**.[46] In doing so the importance of the coordination mode provided by the tropolone, O4, S2O2, and S4, was evaluated in terms of the complex's ability to mimic the activity of insulin type-2 diabetic mice. The O-O chelates are expected to have the lowest relative affinity for Zn, the S-O chelates have an intermediate affinity, and finally the S-S has the most robust binding.[4] $ZnSO_4$ alone displayed an EC_{50} of ca. 176 μM for the enhancement of glucose uptake *in vitro*. This was enhanced in the O4 chelated Zn(trop)$_2$ and Zn(HK)$_2$ with EC_{50} values of 72 μM and 62 μM respectively. This activity is improved further in the S2O2 chelated Zn(**L1**)$_2$ and Zn(**L2**)$_2$, giving EC_{50} values of 0.1 μM and 5 μM. However, the S4 chelated Zn(**L4**)$_2$ and Zn(**L5**)$_2$ actually showed poorer activity than their S2O2 counterparts, giving EC_{50} values of 19 μM and 31 μM respectively. Unlike in previous examples where the biological activity of the tropolone is enhanced with increasing Zn affinity, here there is a sweet spot for maximal activity. This result is mirrored *in vivo* with the S2O2 containing Zn(**L1**)$_2$ outperforming the O4 Zn(trop)$_2$ for controlling blood glucose levels over the course of 25 days in the diabetic mice.

While tropolones are known to act as stand-alone antiproliferative activity, metal-tropolone complexes have also demonstrated such activity.[87] A report by Chen *et al*. in 2017 purported

Compound	Activity	Reference
$Zn(HK)_2$	Anti-viral	[89]
$Zn(HK)_2$	Anti-diabetic	[96]
$Zn(\mathbf{L})_2$	Anti-diabetic	[46]
$Ag(HK)_2$	Anti-bacterial	[68]
$Fe(HK)_3$	Anemia Rescue	[70]
$Cu(HK)_2$	Inhibits Human Inflenza Virus *in vivo*	[86, 97]
$Cu(HK)_2$	Paratosis Promotion	[88]
$Cu(trop)_2$	Anti-cancer	[87]

Table 1.1: Table highlighting a selection of the studies on metal-tropolone complexes as medicinals.

that Copper-bishinokitiol [$Cu(HK)_2$] could be used to induce paraptosis, a form of programmed cell death, in human cancer cells.[88]. $Cu(HK)_2$ was also found to have antiviral activity. [98, 97] Exposure of human influenza virus infected Madin–Darby canine kidney cells to $Cu(HK)_2$ resulted in a reduction in apoptosis relative to untreated cells, cells treated with copper alone, and cells treated with HK alone. Apoptosis results in the release of additional virions from the infected cell, and is thus a key mechanism in influenza's replication cycle. This antiapoptotic effect was found to be directly related to increasing intracellular [Cu^{II}]. A bimetallic complex [Ag(HK)]2 was also found to be effective against a range of bacteria in a 2004 study by Nomiya *et al.*[68] These results parallel the activity of Zn-HK combinations on viral infected cells reported from by Krenn *et al.* and discussed above.[89] **Table 1.1** gives a summary of the results of this discussion, along with the corresponding reference. The antiviral activity of metal-tropolone combinations is of even greater import currently due to the emergence of a new virus in late 2019, SARS-CoV-2, that led to an ongoing global pandemic.[99]

1.4 SARS-CoV-2

1.4.1 Background

Since its emergence in late 2019 a novel coronavirus, SARS-CoV-2 (SC2), caused an uptick in cases of pneumonia in Wuhan, China and has since led to a pandemic on a scale not witnessed since the 1918 Spanish flu.[100, 101, 102] This global public health crisis has led to a massive scientific

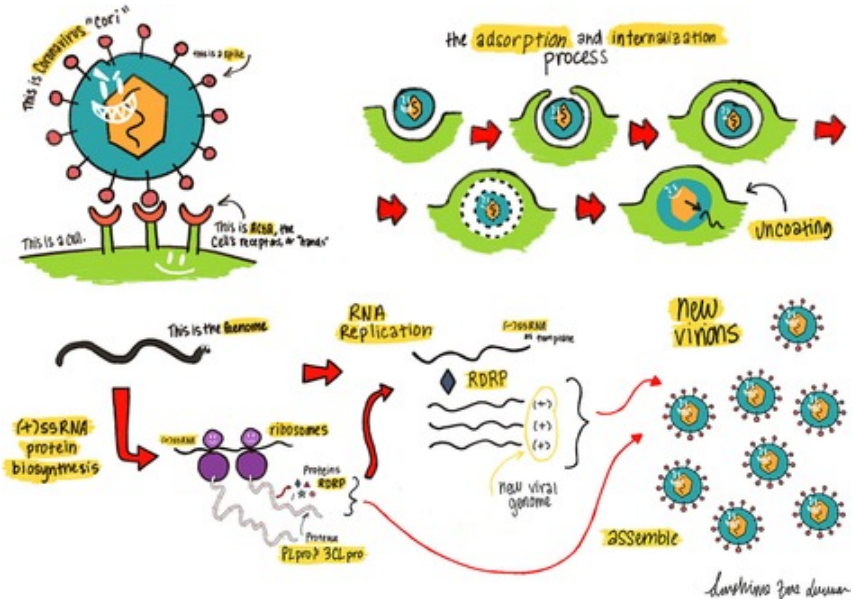

Figure 1.7: Cartoon of the life cycle of SARS-CoV-2 with important critical therapeutic targets the spike protein (S), RNA-depenpendent RNA-polymerase (RdRp), Papain-like protease (PL^{pro}), and the main protease (M^{pro}) are given. This graphic is reprinted from J. S. Morse, T. Lalonde, S Xu and W. R. Liu ref. 101.

effort to better understand the virus in the hopes of developing or re-purposing therapeutics to improve the outcomes for individuals who became infected.[101, 103, 104]

While vaccination provides a long-term solution, small molecule inhibitors provide the first line of defense against emerging pathogens. Due to its similarity to another well known coronavirus, SARS-CoV-1 (SC1), that caused an outbreak in 2003 researchers quickly identified a number of potential therapeutic targets from the previous infection which served as a basis for investigation. The level of genetic similarity between the two coronaviruses is striking. There is 82% sequence identity for the entire genome, and over 90% for a number of critical proteins that are among the aforementioned drug targets. A selection of these are highlighted in the cartoon from an early review by Liu *et al.* in **Figure 1.7**.[101] The four most prominent are the spike protein (S), RNA-dependent RNA-polymerase (RdRp), Papain-like protease (PL^{pro}), and the main protease (M^{pro}) the structures of which can be seen in **Figure 1.8**.[101] Each serves an important role in the viral replication cycle, and presents unique challenges for researchers attempting to block their respec-

tive actions.

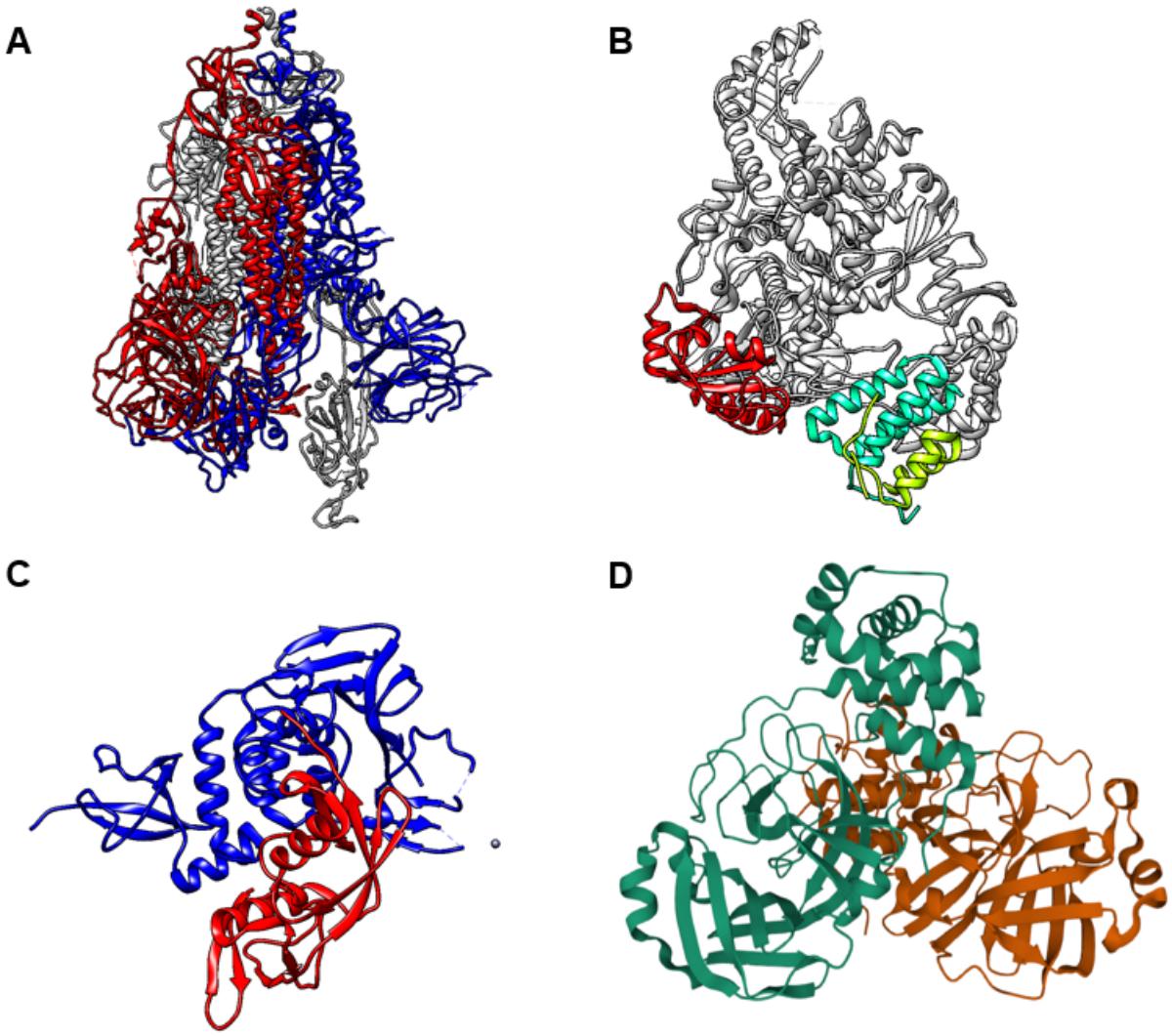

Figure 1.8: The crystal structures of (A) the spike protein (S) (PDB: 7DDN) (B) the RNA dependent RNA polymerase (RdRp) (PDB: 6M71) (C) the papain-like protease (PL^{pro} (PDB: 6YVA) and (D) the main protease (M^{pro}) (PDB:7K3T) of SARS-CoV-2 displayed as ribbons with unique chains delineated by color. Structures downloaded from the protein database (PDB) and made using UCSF chimera ref. 127.

The spike protein of SARS-CoV-2 (SC2S) (**Figure 1.8 A**) is a dimeric protein composed of two subunits, S1 and S2. The SC2S a allows the virus to associate with the surface of the host cell and subsequently infect it.[105] The first subunit, S1 is responsible for the association of the virus to the

host. S1 binds to a cell surface protein known as angiotensin-converting enzyme 2, an important regulator of blood volume and pressure.[106] As such, it is widely expressed within the cardio-respiratory system, and provides an excellent path for this virus to infect its host's respiratory system. Meanwhile, S2 carries out the fusion of the viral and host cell membranes. This process is depicted int the top left of the cartoon of the viral replication cycle in **Figure 1.7**. This allows the virus to enter the cytosol and carry out the infection cycle. SC2S, along with viral messenger RNA, have become the principle targets for vaccine development.[107]

RNA dependent RNA polymerase (RdRp) (**Figure 1.8 B**) catalyzes the polymerization of viral RNA, thus allowing SC2 to reproduce its genetic material. This protein bears a 96% sequence identity to the SC1RdRp. This signifies that known SC1RdRp inhibitors such as Remdesivir, an oligonucleotide analogue originally designed to inhibit Ebola, was quickly brought forward as a potential inhibitor of the infection.[101]

Earlier work by van Hemert *et al.* involving SC1RdRp demonstrated that Zn^{II} was an effective inhibitor of the polymerase both *in vitro* and in vivo.[108] It was found that the well known zinc medicinal, zinc-bispyrithione ($Zn(PT)_2$), reduced viral loading in Vero E6 cells infected with SC1 when compared to untreated control cells.[108] $Zn(PT)_2$ has numerous uses as a medicinal, from anti-dandruff shampoos, to anti-fungal ointments, and has even displayed activity against both gram positive and gram negative bacteria.[109] $Zn(PT)_2$ The antiviral activty of $Zn(PT)_2$ was found to stem in part from the ability of $Zn(PT)_2$ to block the binding of template RNA strands to RdRp, preventing replication of the viral genetic material. This result was echoed in earlier studies by Krenn *et al* mentioned above.[89] Their group also reported that various ionophores, in addition to the $Zn(PT)_2$ complex, were able to reduce replication of a number of different picnoviruses *in vivo*.[110, 89, 111] This antiviral effect correlated well with increasing intracellular Zn concentrations, a result of $Zn(PT)_2$'s ability to serve as a lipophilic source for Zn in all cases.

The Papain-like protease (PL^{pro}) (**Figure 1.8 C**) serves two major roles for the virus within the cell. First, it assists in the cleavage of the viral polyprotein, although the bulk of this activity is carried out by M^{pro}. In addition, it also possesses deubiquitinating activity, removing ubiquitin

from viral proteins. Ubiquitin is one of the ways the cell marks proteins for degradation, and therefore the action of PL^{pro} enables the virus to evade the immune system. This protease bears 83% sequence similarity to the homologous protein in SC1 but has received considerably less attention in terms of drug development relative to the three other targets mentioned. One of the challenges in designing PL^{pro} inhibitors is that human deubiquitinases carry out the same function, and therefore achieving selectivity for the viral deubiquitinase is difficult. The first selective inhibitor for this protease was actually reported in mid 2021 by Tan *et al*.[112] Interestingly, one of the controls for validating the efficacy of their proposed inhibitor was again the famililar $Zn(PT)_2$. This is the second instance in which a Zn-ionophore combination has been found to be effective against a critical viral protein.

The main protease of SARS-CoV-2 ($SC2M^{pro}$) (**Figure 1.8 D**) is responsible for polyprotein processing, cleaving its substrate at 11 sites. $SC2M^{pro}$ contains a catalytic Cys145-His41 dyad that carries out amide bond cleavage, a potential mechanism for which can be seen in **Figure 1.9**.[113] Upon substrate binding, the sp^2 nitrogen of the His41 imidazole sidechain deprotonates Cys145, allowing for nucleophilc attack of the thiolate on the amide ketone of the substrate. Subsequent elimination of the amine leads to cleavage the polyprotein chain, deprotonating His41 in the process. This free amine then deprotonates a nearby water molecule which in turn attacks the ketone carbon, resulting in the canonical tetrahedral intermediate. This intermediate collapses, eliminating the Cys145 thiolate which is protonated in the process. Dissociation of the two products, the halves of the polyprotein, regenerates the resting state of $SC2M^{pro}$.

This catalytic dyad is an attractive target for therapeutics, as blocking the catalytically active Cys145 would deactive the protease. $SC2M^{pro}$ shares 96% sequence homology with the main protease of SARS-CoV-1 ($SC1M^{pro}$).[101] In addition to the re-purposing of previously reported $SC1M^{pro}$ inhibitors, novel $SC2M^{pro}$ inhibitors have also rapidly proceeded to clinical trials.[114] Organic moieties are not the only option for inhibition of $SC2M^{pro}$ however, metal complexes have also been shown to inhibit $SC1M^{pro}$. Some of the most potent are coordination complexes of Zn^{II} and Hg. In studies by Wang *et al*. in 2004, it was found that by selecting the appropriate ligands to

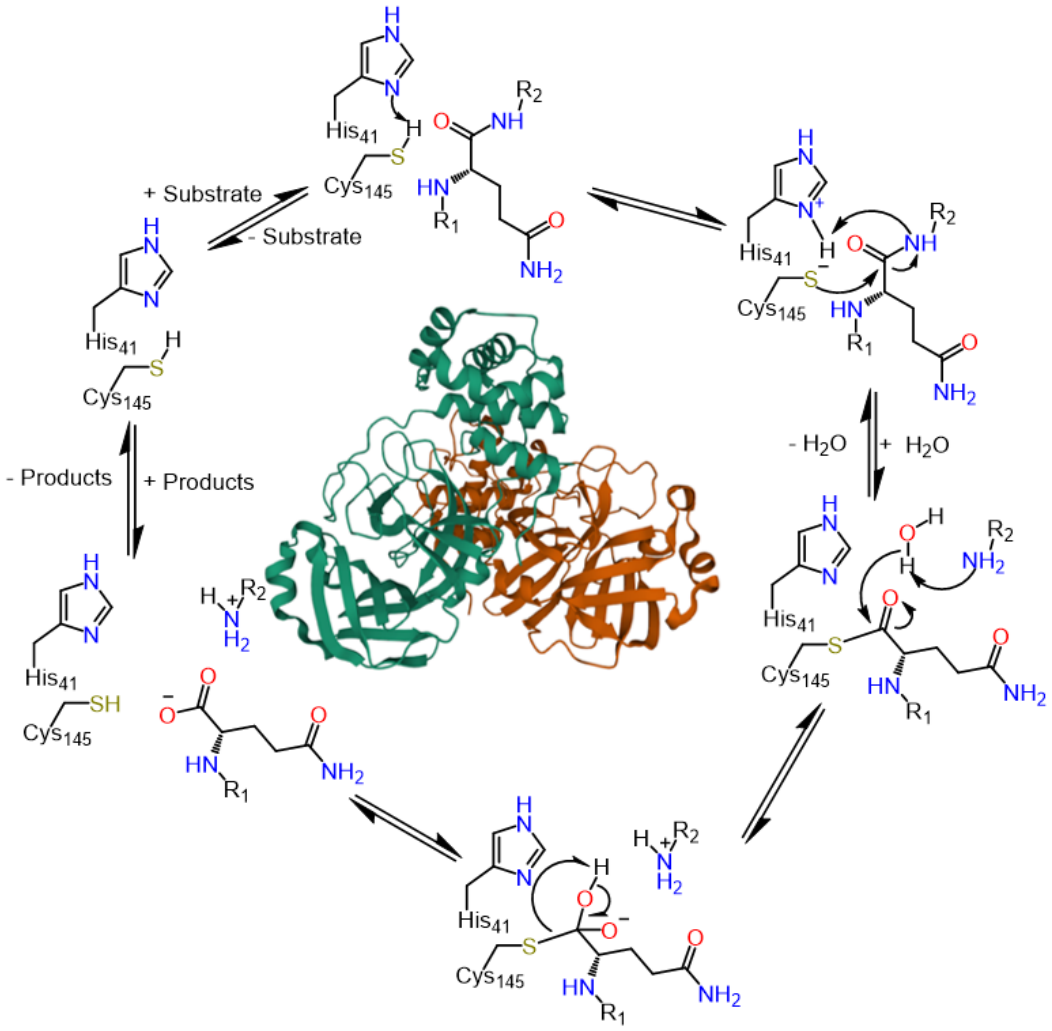

Figure 1.9: The proposed catalytic cycle of the main protease of SARS-CoV-2 (SC2M^{pro}) with the structure of SC2M^{pro}. Figure adapted from Ramos *et al* ref. 113.

surround Zn^{II} 20-fold improvements of *in vitro* inhibition constants (K_i) could be achieved when compared to simple salts that serve as solvated Zn^{II} sources.[115] This also served to change the mode of inhibitory activity from non-competitive for solvated Zn^{II} to competitive. This switch to competitive inhibition likely indicates binding at the active site.[116] Follow-up studies reported in 2007 led to the determination of a number of crystal structures of metal-complexes bound at the SC1M^{pro} active site, with the best resolved revealing a Zn-(1,2-toluenedithiolate) [Zn(TDT)] metallofragment coordinated to the Cys145-His41 dyad.[117] This crystal structure is shown later in **Figure 3.2 B**. These studies provide another example of the potential efficacy of Zn against

SC2M^{pro}.

In the brief description above, it is evident that metals such as zinc may provide alternative warheads, a means of targeting viruses that is currently under explored. Zinc, long used as a medicinal supplement because of its role in immune health,[118, 119, 120, 121] has already been shown to have activity against three of the four major drug targets identified for SC2. It is for this reason that the design, synthesis, and characterization of zinc-based inhibitors was undertaken in our work. Chapter III focuses on the initial investigations of of trop, HK, and their thiolated derivatives in combination with Zn for the inhibition of SC2M^{pro}.[2] Chapter IV expands these studies to first row transition metals as well as variable coordination spheres for the inhibition of SARS-CoV-2, examining the effect of metal identity and coordination mode on the efficacy of these inhibitors to determine their respective importance to activity. My contributions to the determination of the efficacy of another class of thiolate-containing metal complexes with potential as inhibitors, Dinitrosyl Iron Complexes (DNICs), is also given in Chapter IV as these studies use the same SC2M^{pro} activity assay.[122]

2. GENERAL EXPERIMENTAL DETAILS

2.1 General Procedures

2.1.1 General materials and techniques

All air sensitive reactions were carried on a double manifold Schlenk vacuum line under N_2 with the resulting compounds stored under N_2 or Ar in a glovebox. Chloroform ($CHCl_3$), Dichloromethane (DCM), diethylether (Et_2O), hexanes, pentane, acetonitrile (MeCN), toluene, and methanol (MeOH) were freshly purified by an MBraun Manual solvent purification system packed with Alcoa F200 activated alumina desiccant. Reagents were purchased from commercial sources and used as received. Syntheses for 6-(1-Methylethyl)-2-[[(4-methylphenyl)sulfonyl]oxy]-2,4,6-cycloheptatrien-1-one (Tosyl-**L3**),[53] 4-(1-Methylethyl)-2-[[(4-methylphenyl)sulfonyl]oxy]-2,4,6-cycloheptatrien-1-one (Tosyl-**L2**),[53] 2-Mercaptotropone (**L1**),[53] 2-Hydroxy-4-isopropyl-cyclohepta-2,4,6-triene-1-thione (**L3**),[53] 7-Hydroxy-3-isopropylcyclohepta-2,4,5-triene-1-thione (**L2**),[53] $Zn(trop)_2$,[64] $Zn(HK)_2$,[64] 4(5)-(2-haloethyl)imidazole hydrochloride,[123] and 4(5)-(2(S-thiouronium)ethyl)imidazole hydrochloride (NS-mimic)[123], Dithiotropolone (2-Mercapto-cycloheptatrienethione or **L4**),[46] Bis-(dithiotropolonato)zinc(II) ($Zn(\mathbf{L4})_2$)[46], [1-(2-mercapto-ethyl)-methyl-1,4-diazacycloheptane] (N_2SH),[124] and the resulting $[NiN_2S]_2[BF_4]_2$[124] were carried out according to established procedures.

2.1.2 Physical Measurements

^1H and ^{13}C Nuclear Magnetic Resonance Spectroscopy were carried out using a 400MHz NMR spectrometer. Ultraviolet-visible spectroscopy was performed on a Shimadzu UV-2450 spectrophotometer. Solution infrared spectra were recorded on a Bruker Tensor 37 Fourier transform IR (FTIR) spectrometer using a CaF2 cell with a 0.2 mm path length. The Pike MIRacle attachment from Pike Technologies was used for Attenuated Total Reflectance Infrared Spectra for solid-state samples. Solid-state UV measurements were performed by the Materials Characterization Fa-

cility at Texas A&M University. Mass Spectrometry (ESI-MS and ACPI-MS) were performed in the Laboratory for Biological Mass Spectrometry at Texas A&M University. Data collections for X-ray structure-determination were carried out BRUKER Quest X-ray (fixed-Chi geometry) diffractometer with a PHOTON II detector with X-ray radiation generated by a Mo-Iμs X-ray tube (Kα = 0.71073Å). Crystals were coated in paraffin oil and mounted on a nylon loop, and placed under streaming N_2 (110/150K). Integrated intensity information for each reflection was obtained by reduction of the data frames with the program APEX3.The structure was refined (weighted least squares refinement on F2) to convergence. Mercury and OLEX were employed for the final data presentation and structure plots.[125] Full data for the crystal structures can be found in the supplementary files.

2.2 Experimental Details for Chapter III

2.2.1 Lipophilicity determination for Zn complexes

Octanol-water partition coefficients were obtained as following established protocols.[126, 70] For **L1**, a stock solution in 1-octanol (pre-equilibrated with Phosphate Buffered Saline pH = 7.4) was created and used to establish a standard curve. Partition experiments were conducted by shaking 5 mL the 1-octanol solutions of **L1** with an equal volume of Phosphate Buffered Saline (PBS) for 1 hour, followed by separation for an additional hour. The absorbance at 420 nm of the organic layer was measured as was that of the PBS layer. This was repeated with fresh solutions, with 0.5 eq of $Zn(OAc)_2$ dissolved in the PBS before partition. The ratio of the absorbance in the organic and aqueous layers was used to calculate the partition coefficients. For the intact complexes, a standard curve of known concentrations of each Zn-complex was established in PBS saturated 1-octanol. Next, 5 mL aliquots of the most concentrated $Zn(\mathbf{L})_2$ solutions were transferred to separatory funnels, at which point 45 mL of the pre-equilibrated PBS was added for a total volume of 50 mL. These flasks were shaken for 1 hour before being allowed to rest for an additional hour to ensure separation of the phases. A sample of the organic layer was taken for analysis via UV-Vis

and the partition coefficient calculated as previously described. All trials were completed in triplicate.

2.2.2 Computational Methods

AutoDock4 was used for blind docking and for the generation of binding poses. The protein used in this study was the monomer of the SC2M^{pro} (PDB:6W63) with the inhibitor X77 and water removed. For each potential inhibitor, **L**, Zn(**L**)$^+$, and Zn(**L**)$_2$, the genetic algorithm-based calculation was performed with 20 runs for the blind docking, and 100 runs for the active site docking with the output being in Lamarckian Genetic Algorithm form. The rest of the parameters are as follows: Population Size: 150, Max. number of evaluations: 2.5 million, Max. number of generations 27000, rate of crossover: 0.8. The **L** and Zn(**L**)$^+$ molecules used in these simulations were truncated forms of the Zn(**L**)$_2$ crystal structures for **L1** and **L2**. The charges on all potential inhibitors were generated using an AM1-BCC forcefield. For the coordinatively unsaturated Zn(**L**)$^+$, the charge of the ligand was calculated, and then charge was assigned to the metal to align with the charge of the fragment (i.e., if the total charge of the **L** was -1, and the known charge of the metal-containing fragment was +1, then the charge assigned to the Zn would be +2). Since no crystal structures exist for the Zn(**L3**)$_2$ complex, the bis-ligated complex was generated using the Structure Editing tools in UCSF Chimera.[127] This Zn(**L3**)$_2$ was then truncated in an analogous manner to generate **L3** and Zn(**L3**)$^+$.

2.2.3 Syntheses

Zn(2-Mercaptotropone)$_2$ [Zn(**L1**)$_2$]

This preparation was adapted from Murakami *et al.* A methanolic solution containing 205 mg (0.94 mmol) of Zn(OAc)$_2$·2H$_2$O was added via cannula to a stirred methanolic solution of **L1** (288 mg, 2.07 mmol). The resulting solution was then heated to 60°C and stirred vigorously for

3h before being allowed to cool to 22°C with stirring overnight. Stirring ceased and the orange precipitate was allowed to settle. The supernatant was then decanted via and the solid washed 2 times with additional methanol. The remaining solid was taken to dryness under vacuum and the resulting yellow/orange solid suspended in minimal diethyl ether. Cold (-20°C) pentane was then added to precipitate a yellow solid. The supernatant was then removed via canula and the solid was then washed twice more with cold pentane to remove excess ligand followed by purging with N_2 before drying *in vacuo*. (yield: 256 mg (80.2%)) Crystals suitable for XRD were obtained by slow evaporation of a filtered DCM solution saturated with the compound. $^{+}$APCI-MS (m/z): 338.94. $[M+H]^{+}$ ^{1}H NMR (400MHz CDCl3): δ 8.68(1H, m), 7.58(1H, d) 7.48(1H, m) 7.26(2H, m). Elemental Analysis: Calc'd for $C_{14}H_{10}S_2O_2Zn$: C, 49.50 H, 2.97 S, 18.87; Found: C, 48.72 H, 3.02 S, 18.33.

Zn(7-Hydroxy-3-isopropylcyclohepta-2,4,5-triene-1-thione)$_2$ [Zn(**L2**)$_2$]

A methanolic solution containing 46 mg (0.2 mmol) of $Zn(OAc)_2{\cdot}2H_2O$ was added via cannula to a stirred methanolic solution of **L2** (75 mg, 0.4 mmol). The resulting solution was then heated to 60°C and stirred vigorously for 3h before being allowed to cool to 22°C with stirring overnight. Stirring ceased and the orange precipitate was allowed to settle. The supernatant was then decanted via cannula and the solid washed 2 times with additional methanol. The remaining solid was taken to dryness under vacuum and the resulting yellow/orange solid suspended in minimal diethyl ether. Cold (-20°C) pentane was then added to precipitate a yellow solid. The supernatant was then removed via canula and the solid was then washed twice more with cold pentane to remove excess ligand followed by purging with N_2 then drying *in vacuo* (yield: 46.5 mg (53%)). Crystals suitable for XRD were obtained by slow evaporation of a filtered $CDCl_3$ solution of the compound. $^{+}$APCI-MS (m/z): 423.04. $[M+H]^{+}$ ^{1}H NMR (400MHz, CDCl3) δ 8.72(1H, s), 7.39(2H, m), 7.10(1H, d), 2.87(1H, m), 1.24(6H, d). Elemental Analysis: Calc'd for $C_{20}H_{22}S_2O_2Zn$: C, 56.67 H, 5.23 S, 15.13; Found: C, 56.50 H, 5.16 S, 14.96.

Zn(2-Hydroxy-4-isopropylcyclohepta-2,4,6-triene-1-thione)$_2$ [Zn(**L3**)$_2$]

A methanolic solution containing 140 mg (0.64 mmol) of Zn(OAc)$_2$·2H$_2$O was added via cannula to a stirred methanolic solution of **L3** (234 mg, 1.3 mmol). The resulting solution was then heated to 60°C and stirred vigorously for 3h before being allowed to cool to 22°C with stirring overnight. Stirring ceased and the orange precipitate was allowed to settle. The supernatant was then decanted via cannula and the solid washed 2 times with additional methanol. The remaining solid was taken to dryness under vacuum and the resulting yellow/orange solid suspended in minimal diethyl ether. Cold (−20°C) pentane was then added to precipitate a yellow solid. The supernatant was then removed via canula and the solid was then washed twice more with cold pentane to remove excess ligand followed by purging with N_2 then drying *in vacuo* (yield: 137.5 mg (51%)). $^+$APCI-MS (m/z): 423.04. $[M+H]^+$ ^{1}H NMR (400MHz, CDCl3) δ 8.53(1H, s), 7.57(1H, s) 7.17(2H, s), 2.88(1H, m), 1.24(6H, d).

[Zn(**L1**)(Histidine)]

This reaction is representative of the displacement reactions used to probe the lability of **L1** in the Zn(**L1**)$_2$ complex. A methanolic solution containing 60 mg (0.4 mmol) of L-Histidine was added via cannula to a stirred methanolic suspension of Zn(**L1**)$_2$ (34 mg 0.1 mmol). This suspension was allowed to stir overnight at 50°C resulting in an orange solution. This solution was taken to dryness *in vacuo* and the resulting orange solid washed with copious amounts of diethyl ether and then chloroform till washes were clear. Purging with N_2 followed by drying *in vacuo* resulted in a yellow powder (yield: 15 mg (42.1%)). $^+$ESI-MS (m/z): 356.00. $[M]^+$ ^{1}H NMR (400MHz, MeOH-d4) δ 8.61(1H, s), 7.91(1H, s) 7.72(1H, s), 7.48(1H, m), 7.41(1H, d), 7.22(2H, m), 7.01(1H, s) 3.85(1H, m), 3.21(2H, m).

2.3 Experimental Details for Chapter IV

2.3.1 SC2M^{pro}-Zn complex binding by Native Mass Spectrometry (Native MS)

Sample preparation

Protein was buffer exchanged into 200 mM ammonium acetate (AA) aqueous buffer (pH = 7) using a centrifugal desalting column. Zn-complex stock solutions were prepared by dissolving 1 mg Zn-complex in 10 L of DMSO. Ten-fold dilution of each stock solution in 200 mM AA was performed. Protein solution was mixed with Zn-complex solution at 4:1 (v/v) ratio and incubated at room temperature for 1 min prior to mass spectrometry analysis.

Native Mass Spectrometry (Native MS)

Samples were loaded into borosilicate glass capillary needles and examined by Q Exactive UHMR Hybrid Quadrupole-Orbitrap mass spectrometer (ThermoFisher Scientific). Electrospray voltage was applied through a platinum wire that was inserted directly into the solution. Instrument was set to 1.4 kV for spray voltage, 100 °C for capillary temperature. In-source trapping was set to on with -50 V desolvation voltage. HCD event was set to 3 ms for HCD time, 20 ms for purge time, 2 V for C-trap exit lens purge, 200 V for HCD field gradient, and 5 for trapping gas pressure. Spectra were collected from 3000 m/z to 8000 m/z with 1 microscan and 500 ms maximum inject time at a resolution of 12,500 for 2 min.

Data processing

Spectra were deconvoluted using UniDec[128] software with no smoothing, range from 4000 to 7000 m/z, charge states range from 8 to 15, mass sampling of every 1 Dalton (Da), and a peak FWHM of 0.1.

2.3.2 Inhibition Assays

Expression and purification of SC2M^{pro} and synthesis of FRET substrate Abz-SAVLQSGFRK-(Dnp)-NH_2 were described in Mellott *et al.*[102] To avoid metal chelation from the buffering reagent, a final concentration of 20 mM HEPES (pH 7.5) was used as the buffering reagent. All enzyme assays were carried out in 96-well plates (Greiner, half-area, black wells with clear bot-

toms) at 25°C, in the presence of 30 μM Abz-SAVLQSGFRK(Dnp)-NH_2 substrate (K_m = 30 μM, Figure Sx), 150 mM NaCl, 0.5 mg/mL bovine serum albumin (BSA, Amresco incorporation), 1 mM tris(2-carboxyethyl)phosphine (TCEP) as the reducing reagent, and 10% DMSO (v/v). Assays were initiated by the addition of 15 nM $SC2M^{pro}$, and fluorescence increase from product formation was measured using a SpectraMax M2 (Molecular Devices) microplate reader, with wavelengths of excitation at λ_{ex} = 320 nm and emission atλ_{em} = 420 nm. Time courses of fluorescence change were recorded for 20 minutes.

Data processing of enzyme assays: Steady-state reaction rates were acquired from the linear phases of fluorescent reading relative fluorescence units (RFU) versus time by fitting to eq. **S1**, in which y_0 is the background RFU value, t is time (sec), v is the steady-state rate of fluorescence change in the presence of inhibitors, or DMSO as the blank control.

(**S1**): $RFU = v * t + y_0$

Inhibition constants (Ki) were obtained by fitting values of v_i/v_0 to eq. **S2**, where v_0 is the steady-state reaction rate in the presence of DMSO as blank control, and v_i is the reaction rate in the presence of varying concentrations of inhibitors. [A] is the concentration of substrate (30 μM), and [I] is the concentrations of inhibitors. Km is the Michaelis constant of Abz-SAVLQSGFRK(Dnp)-NH_2 (30 μM).

(**S2**)$v_i/v_0 = 1/(1 + (K_m/(K_m + [A])) * (([I])/K_i))$

2.3.3 Syntheses

Fe(2-Mercaptotropone)$_3$ [Fe(**L1**)$_3$]

Methanol (25 mL) was added via cannula to a degassed shlenk flask containing **L1** (87 mg, 0.6 mmol) and $FeCl_2$ (26 mg, 0.1 mmol) and allowed to stir overnight at 22°C. After stirring ceased, a dark precipitate was observed and the supernatant decanted. The solid was then washed with copious amount of MeOH before drying by purging N_2. It was then dissolved in dichloromethane (DCM) and passed through a glass frit layered with celite before being taken to dryness *in vacuo*

(yield: 36 mg (38.5%)). $^{+}$ESI-MS (m/z): 329.95 .[M-**L1**]$^{+}$ Elemental Analysis: Calculated for $C_{21}H_{15}S_3O_3Fe$: C, 53.97 H, 3.24 S, 20.58; Found: C, 53.84 H, 3.30 S, 20.62

Co(2-Mercaptotropone)$_3$ [Co(**L1**)$_3$]

Methanol (25 mL) was added via cannula to a degassed shlenk flask containing 83 mg of **L1** (0.6 mmol) and 25 mg (0.2 mmol) of $CoCl_2$ and allowed to stir overnight at 22°C. After stirring ceased, a dark precipitate was observed and the supernatant decanted. The solid was then washed with copious amount of MeOH before drying by purging N_2. It was then dissolved in DCM and passed through a glass frit layered with celite before being taken to dryness *in vacuo* (yield: 18 mg (18.9%)). Crystals suitable for XRD were obtained by slow evaporation of a filtered $CDCl_3$ solution of the compound. $^{+}$ESI-MS (m/z): 332.95 [M-**L1**]$^{+}$. Calc'd for $C_{21}H_{15}S_3O_3Co$: C, 53.61 H, 3.21 S, 20.44; Found: C, 53.55 H, 3.16 S, 20.46

Ni(2-Mercaptotropone)$_2$ [Ni(**L1**)$_2$]

A methanolic solution containing 30 mg (0.18 mmol) of $Ni(OAc)_2$ was added via canula to a stirred solution of **L1** (64 mg, 0.46 mmol) in MeOH. This mixture was allowed to stir overnight at 22°C, resulting in the formation of a dark precipitate. The supernatant was decanted and the purple solid washed with copious amounts of MeOH before being taken to dryness by purging N_2. The solid was then dissolved in DCM and passed through a glass frit layered with celite before being taken to dryness *in vacuo* (yield: 51 mg (85.1%)). Crystals suitable for XRD were obtained by slow evaporation of a filtered DCM solution of the compound. $^{+}$ESI-MS (m/z): 332.95 [M+H]$^{+}$.

Cu(2-Mercaptotropone)$_2$ [Cu(**L1**)$_2$]

A methanolic solution containing 34 mg (0.2 mmol) of $CuCl_2{\cdot}2H_2O$ was added via cannula to a stirred solution of **L1** (63 mg 0.46 mmol) in a degassed 100 mL shlenk flask. This mixture was

allowed to stir for 1 hour before being transferred via canula into a stirred solution of in MeOH. This was allowed to stir overnight at 22°C. After stirring ceased, a dark precipitate was observed and the supernatant decanted. The solid was then washed with copious amount of MeOH before drying by purging N_2. It was then dissolved in DCM and passed through a glass frit layered with celite before being taken to dryness *in vacuo* (yield: 38 mg (56.2%)). Crystals suitable for XRD were obtained by slow evaporation of a filtered DCM solution of the compound. $^{+}$ESI-MS (m/z): 337.95. $[M+H]^{+}$

2.4 Experimental details for Chapter V

2.4.1 DOSY NMR

Spectra were recorded on a Varian NMRS 500 MHz spectrometer equipped with a 5 mm $^{1}H/^{19}F/^{13}C/^{31}P$ quad resonance probe and a z gradient coil (up to 30 G/cm) using an 8 mg sample of $[\mathbf{Ni\text{-}I}]^{0}$ in D_2O and 4 mg of $[\mathbf{Ni\text{-}I}]^{0}$ in CD_2Cl_2. The probe temperature was kept at 25°C, and the samples were equilibrated for at least 15 min prior to the experiment. ^{1}H diffusion experiments were carried out with static samples using the convection-compensated bipolar pulse pair stimulated echo pulse sequence (Dbppste_cc).[129] The 90°pulse was 9.90 μs. The incremented gradient strength (g) was varied from 1 to 30 G/cm over an array size of 16. The bipolar pulse gradient duration (δ) was 2 ms, and the diffusion period (Δ) was 50 ms in D_2O and (δ) 1.1 ms and (Δ) 27.5 ms in CD_2Cl_2, respectively. The number of transients per increment was 128 with a relaxation delay of 5 s. DOSY spectra were generated with the program MestReNova 6.0.2.[130]

2.4.2 Syntheses

$[\mathbf{Ni\text{-}I}]^{4}{}_{0}$

The N_2SO ligand (1.00 mmol) was synthesized *in-situ* from NaAcI (sodium iodoacetate, 0.21 g, 1.00 mmol) with yellow oil-like N_2SH (0.17g, 1.00 mmol)[124] in a MeOH (20 mL) solution,

followed by adding the MeOH solution of NaOMe (54 mg, 1.0 mmol). The solution was stirred overnight. The green solution of $Ni(BF_4)_2 \cdot 6H_2O$ (0.34 g, 1.0 mmol) in MeOH was transferred to the resulted colorless solution. After stirring for several hours (8 h), the resulted blue solution was dried under vacuum. The crude product was purified by dissolving in MeCN and filter through a basic Al_2O_3 column. The blue band was washed down by a mixed solvent DCM (10% MeOH). The greenish blue solid was obtained from all solvent removal and diethyl ether wash. The yield was 40%. X-ray quality crystals were obtained from vapour transfer of diethyl ether into a solution of MeCN. High resolution $^+$ESI-MS: m/z 416.96 (Calc. for $[M+H]^+$, 416.96), the mass of a monomeric unit.

[Ni-solv]$^4{}_{4+}$

The green solid of **[Ni-I]**$^4{}_0$ (0.16 g, 0.1mmol) was dissolved in 30 mL MeCN. A solution of $AgBF_4$ (0.02 g, 0.1 mmol) in 5 mL MeCN was titrated to the greenish blue solution. The AgI precipitates formed immediately. The resulted cloudy solution was filtered through a celite column after 3 hours. Blue solid was produced from solvent removal and diethyl ether wash. High resolution $^+$ESI-MS: m/z 289.0507 (Calc. for $[M+H]^+$, 289.0515), the tetramer was split into monomers under ESI condition, and no $[Ni\text{-}I]^0$ peak observed. Elem. Anal. Calc. for $C_{40}H_{76}N_8B_4F_{16}Ni_4S_4O_8$: C, 31.87; H, 5.08; N, 7.43. Found: C, 31.00; H, 5.87; N, 7.85%.

3. ZINC THIOTROPOLONE COMBINATIONS AS INHIBITORS OF THE SARS-COV-2 MAIN PROTEASE[1]

3.1 Introduction

Viral epidemics, such as the one caused by the 2019 novel coronavirus (SARS-CoV-2), present enormous public health challenges.[100, 131] With each outbreak, the biomedical research community intensifies efforts to find druggable targets or vulnerabilities in the virus' replication machinery.[112, 101, 132, 104, 133] A principal focus of these efforts is the main protease of SARS-CoV-2, ($SC2M^{pro}$) represented in **Figure 3.1**. Homodimerization activates this Cys-His protease which carries out polyprotein processing, a key component of the viral replication cycle. Using the knowledge gleaned from structures of $SC2M^{pro}$ complexed with potential therapeutics,[134, 135, 136, 103] as well as previous work carried out with the closely related main protease of SARS-CoV-1 ($SC1M^{pro}$),[137, 104, 138] a number of promising inhibitors have been identified. Small organic molecules, featuring motifs similar to the substrate of the cellular target, make up the majority of these candidates with large libraries being screened against the viral target, *in vitro*, *in vivo*, and *in silico*.

Metals have been proposed as "alternative warheads" capable of forming dative bonds with basic residues such as those in the Cys145-His41 catalytic dyad, **Figure 3.1**. This dative bonding could block the dyad or alter protein structure, meaning a metal ion could function in place of the electrophilic moieties often found in organic small molecule therapeutics. Computational studies by Garzia-Lopez, Gray, *et al.*[139, 140] indicate that available ligation sites on cobalt and copper complexes permit their binding to $SC2M^{pro}$, potentially disrupting viral protein processing. Copper complexes have been shown to inhibit replication of human influenza viruses [86] and copper gluconate displayed some efficacy against $SC2M^{pro}$ *in vitro*.[141] Cohen, *et al.* recently reported

[1]Reprinted with permission from "Zinc thiotropolone combinations as inhibitors of the SARS-CoV-2 main protease" by DeLaney, Christopher Ryan and Sheng, Yan and Pectol, D. Chase and Vantansever, Erol and Zhang, Hanyuan and Bhuvanesh, Nattamai and Salas, Isaiah and Fierke, Carol and Liu, Wenshe and Darensbourg, Marcetta Y., 2021. Dalton Transactions, Copyright 2021 by Royal Society of Chemistry.

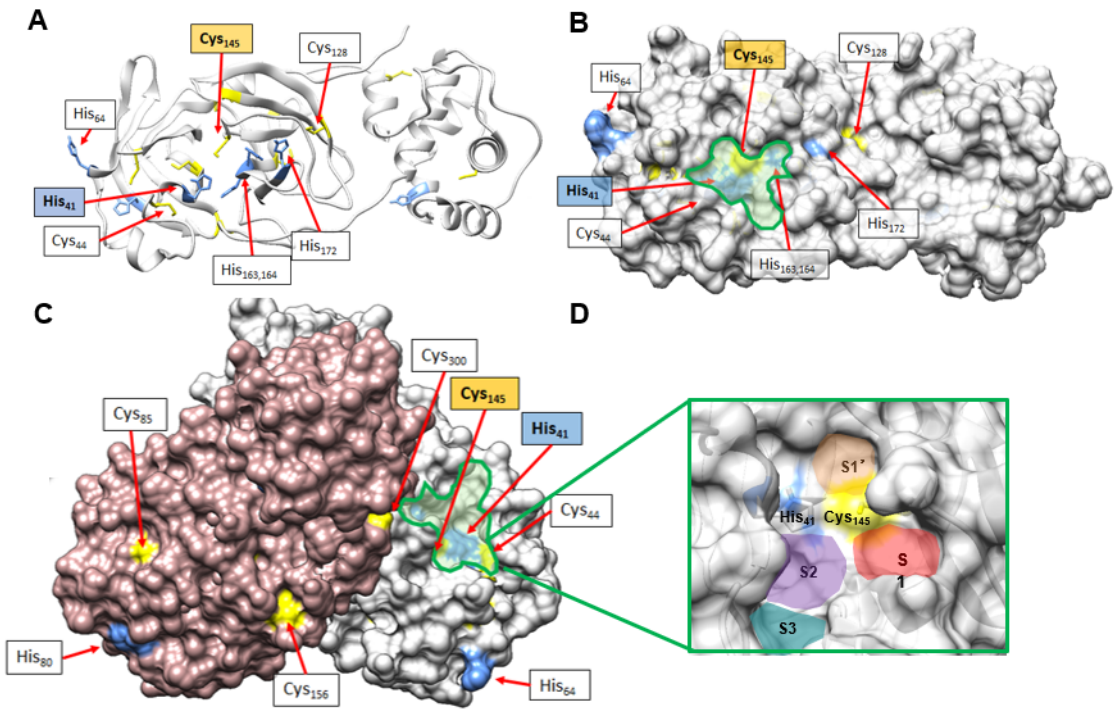

Figure 3.1: Identification of possible metal binding residues on the surface of the monomer (A and B) and dimer (C) of SC2M^{pro} (PDB:6W63) with a close up of the active site (D). The surface available cysteine (yellow) and histidine (blue) residues are labeled using their three letter abbreviations and sequence position. The catalytic dyad of His41 and Cys145 are emphasized with colored labels. (A) The ribbon representation of SC2M^{pro}, (B) The calculated molecular surface of the monomer, and (C) the combined surfaces of the catalytically active dimer. The substrate binding pocket is highlighted in green in panels B and C. Substrate binding pockets and the dyad are color coded in D for clarity. All graphical representations were generated using UCSF Chimera ref. 127.

an organometallic fragment with abiological ligands $[(bipy')Re(CO)_3]^+$ can inhibit SC2M^{pro} *in vitro*, also finding by computations placement of the open site on Re^I nearby the Cys145 within the enzyme active site.[142] The latter result was supported by comparative mass spectrometric studies of the protein bound with a selective covalent inhibitor of Cys145 vs. that with the rhenium complex.

Zinc, a micronutrient long understood to have antiviral properties,[143, 144, 110, 145] has been found to inhibit SC1M^{pro} in the form of "free" Zn^{II} hydrate as well as in coordination complexes.[115, 117] The well known lability of zinc in complexes with hard donors is diminished

on attachment of sulfur based ligands.[146, 45] Coordination complexes of zinc and ionophoric ligands are known to inhibit a number of RNA viruses, including SARS-CoV-1, both *in vitro* and *in vivo*.[89, 110, 111, 108] A key chemical feature of ionophores that facilitates *in vivo* efficacy is the lipophilicity they impart to metal ions, thus promoting passive diffusion of the metal complex into the cytosol in a concentration-dependent manner.[70] Given that low intracellular Zn^{II} levels are associated with poor patient outcomes for numerous viral infections, including SARS-CoV-2,[147, 121] the promise that ionophores might both facilitate the import of Zn^{II} and also stabilize its interaction with $SC2M^{pro}$ offers an appealing prospect. Indeed, the attachment of appropriate ligands to zinc shown to improve K_i by up to 20-fold against $SC1M^{pro}$.[115, 117] This approach has garnered attention, with a number of publications and clinical trials purporting the benefits.[148, 149, 120, 150, 151] Nevertheless the lability of zinc complexes necessitates careful ligand design to create the greatest greatest effect.

Herein we explore thiolated-tropolones for Zn-based inhibition of $SC2M^{pro}$, aiming to capitalize on the affinity of sulfur for Zn^{II},[45] while preserving sufficient substitutional lability that could permit interactions with the catalytic dyad or other structurally significant basic residues. Cohen *et al.* compiled a useful library of potential ligands for the inhibition of bacterial zinc metalloproteases such as anthrax lethal factor, matrix metalloproteinases, etc. in which tropolones such as hinokitiol (HK) featured prominently.[10] The ligands inactivate these zinc-dependent enzymes via chelation and removal of the catalytic metal center. In our system however, we use thiotropolones to enhance Zn-based inhibition of $SC2M^{pro}$ via delievery of zinc to the catalytic dyad. Previous studies have demonstrated that modifications to the primary coordination sphere have marked impacts on the biological activity of Zn^{II} ionophore complexes,[46, 94, 152] as does varying ligand backbone substituents.[93, 153] Tropolones and their S-modified derivatives are examined herein, as they have seen success in other applications but remain under explored for viral inhibition.[46, 154, 53] Recognizing that the major benefit of ionophores should be displayed in cell membrane permeation, this initial *in vitro* study explores tropolone/Zn^{II} combinations as inhibitors of $SC2M^{pro}$. Inhibitor efficacy was determined via an established FRET-

based protease assay.[133, 155] Computational docking (Autodock4 modified for metal-containing compounds)[140, 142] is employed for further insight. These studies demonstrate the potential of such zinc-based inhibitors of $SC2M^{pro}$ and the importance of specific ratios of ligand to metal that optimize the effect.

3.2 Results

3.2.1 Syntheses and Characterization

Three thio-tropolone ligands **L1**, **L2**, and **L3**, were prepared and contrasted to the known 2-oxy analogues (E = O). Nozoe and coworkers reported the thiolated derivative of tropolone (Trop), 2-mercaptotropone (**L1**) in 1953;[42] analogous syntheses of thiolated derivatives of hinokitiol (HK) (**L2**, **L3**) followed shortly thereafter.[43] We utilized a recent approach by Elagawany, *et al*.[53] that permits generation and subsequent separation of the two possible isomers of the thiolated HK ligands: 4-isopropyl-thiotropolone (**L2**) and 6-isopropyl-thiotropolone (**L3**). The protonated ligands were isolated as red-orange solids (**L1**-**L2**) or oils (**L3**) and purified by column chromatography. Reaction of 2 equiv. of **L1**-**L3** with $Zn(OAc)_2$ in methanol with heating results, in all cases, in a color change from intense red-orange to yellow, with formation of a yellow precipitate corresponding to the bis-ligated complexes, **Figure 3.2 A**, in ca. 50-80% yields of crude product. Further details can be found in Chapter II while the characterizations (Mass Spectra, ^{1}H NMR spectra, UV-vis spectra, Elemental Analysis of Bulk Samples, and XRD crystal structures) are given in the Appendix.

3.2.2 Molecular Structures

Slow evaporation of saturated CH_2Cl_2 solutions of Zn(**L1**)$_2$ and Zn(**L2**)$_2$ resulted in yellow needles suitable for XRD. The structures of these complexes are given in **Figure 3.2 B** as well as **Figures D.5** and **D.6**. Complex Zn(**L1**)$_2$ crystallized in the C12/c1 space group while Zn(**L2**)$_2$ is in P12$_1$/n1. Both have 4-coordinate zinc with $\tau_4{}'$ values of 0.695 and 0.697 respectively, indicating a flattened tetrahedral geometry ($\tau_4{}'$ = 1 for perfect T_d).[156] The nearest π-centroid distance of 3.30 Å in Zn(**L1**)$_2$ indicates the presence of π-π stacking interactions in the solid phase.[39]

A

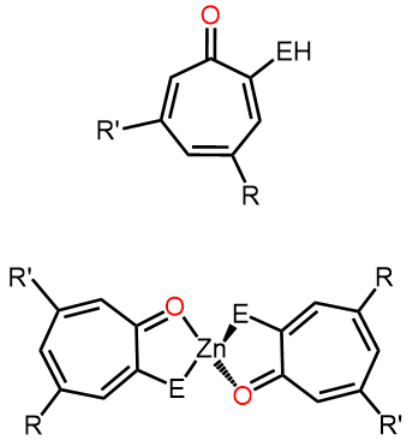

Ligand	Complex	Mode	E	R	R′
Trop	$Zn(Trop)_2$	O_4	O	H	H
HK	$Zn(HK)_2$	O_4	O	iPr	H
L1	$Zn(\mathbf{L1})_2$	S_2O_2	S	H	H
L2	$Zn(\mathbf{L2})_2$	S_2O_2	S	iPr	H
L3	$Zn(\mathbf{L3})_2$	S_2O_2	S	H	iPr

B

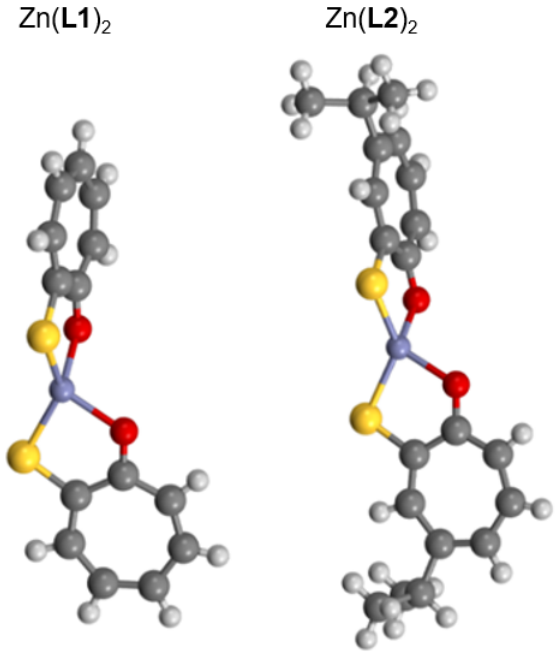

Figure 3.2: The general structure of the tropolone-based ligands used in this study and the expected structure of the bis-ligated Zn^{2+} complexes. Table summarizes the substituents at E, R, and R′ for each complex. (B) The XRD-determined molecular structures of $Zn(\mathbf{L1})_2$ (left) and $Zn(\mathbf{L2})_2$(right).

These interactions are absent in the $Zn(\mathbf{L2})_2$ structure, presumably because of the presence of the bulky i-Pr moiety on the ligand backbone. The monomeric nature of these S_2O_2 complexes in the solid state contrasts with the analogous O_4 bis-HK zinc complex[64] and the S_2O_2 bis-pyrithione zinc,[157] both of which crystallized as dimers with O- or S-bridges leading to penta-coordinate zinc; the O_4 bis-Trop complex crystallized in an extended chain, coordination polymer.[64] As expected, $Zn(\mathbf{L1})_2$ and $Zn(\mathbf{L2})_2$ have very similar metric parameters with $Zn\text{-}O_{avg}$ and $Zn\text{-}S_{avg}$ bond lengths of 1.98 Å and 2.27 Å, respectively, and an average O-Zn-S angle of 87.2°. The $Zn(\mathbf{L3})_2$ complex has not yet yielded to crystallization.

3.2.3 Solution Phase Properties

Although sparingly soluble in water, the $Zn(\mathbf{L})_2$ complexes readily dissolve in a number of organic solvents, including DMSO, CH_3CN, CH_2Cl_2 (DCM), THF, $CHCl_3$, Et_2O, and 1-octanol.

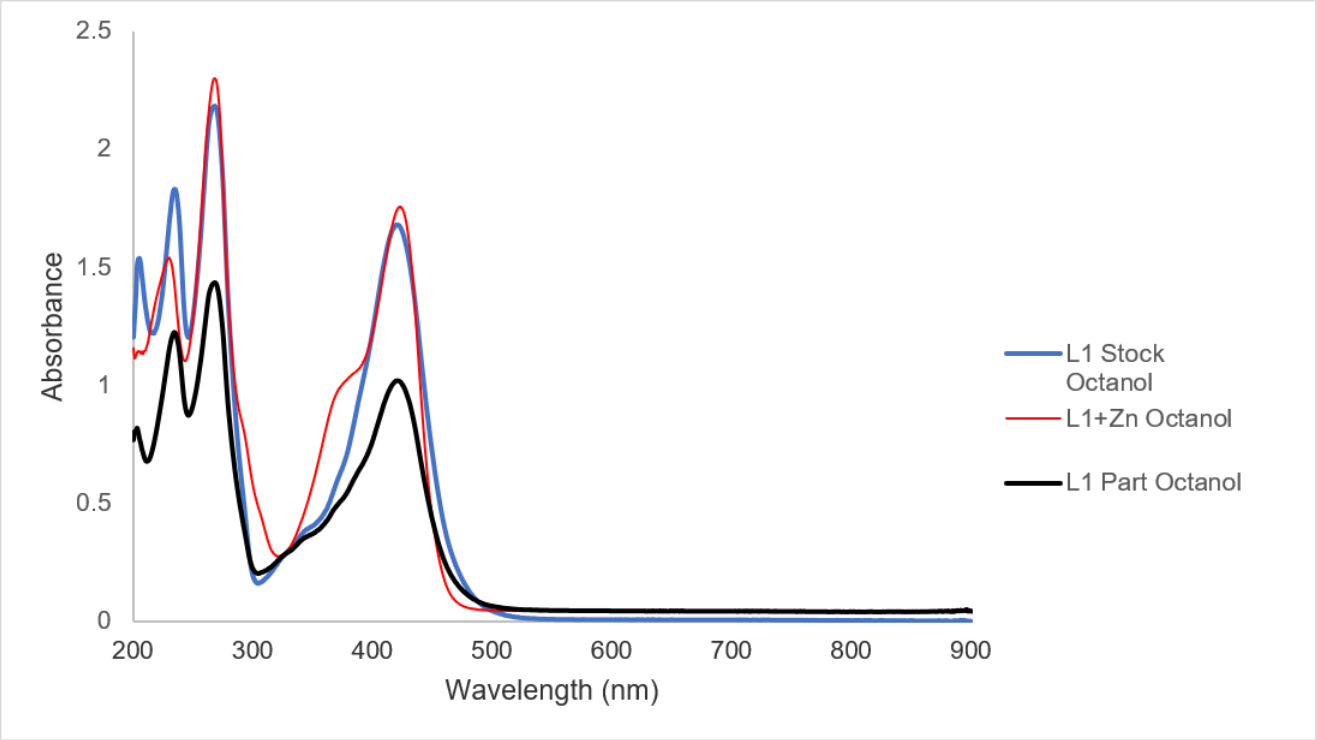

Figure 3.3: Overlay of UV-Vis spectra of 1-octanol layer before (blue) and after (red with $Zn(OAc)_2$, black without $Zn(OAc)_2$) partitioning between 1-octanol and phosphate buffered saline.

Lipophilicity was investigated by performing partitioning experiments between 1-octanol and Phosphate Buffered Saline (PBS) at pH = 7.4 using UV-Vis spectroscopy.[126] Starting with **L1** dissolved in 1-octanol, the partitioning of **L1** between PBS and 1-octanol was investigated in the presence and absence of $Zn(OAc)_2$ in the aqueous layer. In the absence of Zn^{2+}, partitioning results in a $LogD_{7.4}$ for **L1** of 0.36, **Figures C.7** and **C.8**, a slight preference for 1-octanol. However, in the presence of 0.5 equiv. of $Zn(OAc)_2$ in the aqueous layer, the lipophilicity of the resulting species increases substantially, and the resulting spectrum shifts from that of free **L1** to that of the isolated $Zn(\mathbf{L1})_2$ complex, **Figures C.8** and **C.9**. An overlay of the three spectra can be seen in **Figure 3.3**. These results, along with $LogD_{7.4}$ values for the intact $Zn(\mathbf{L1})_2$ (1.77) and $Zn(\mathbf{L2})_2$ (3.73), are summarized in **Table F.1**. They point to the ability of **L** to bind Zn^{II} and subsequently promote diffusion into non-polar environments. The results are consistent with the ability of tropolones to promote cell membrane penetration as has been reported in a number of similar systems.[89, 70]

3.2.4 Ligand Displacement Reactivity

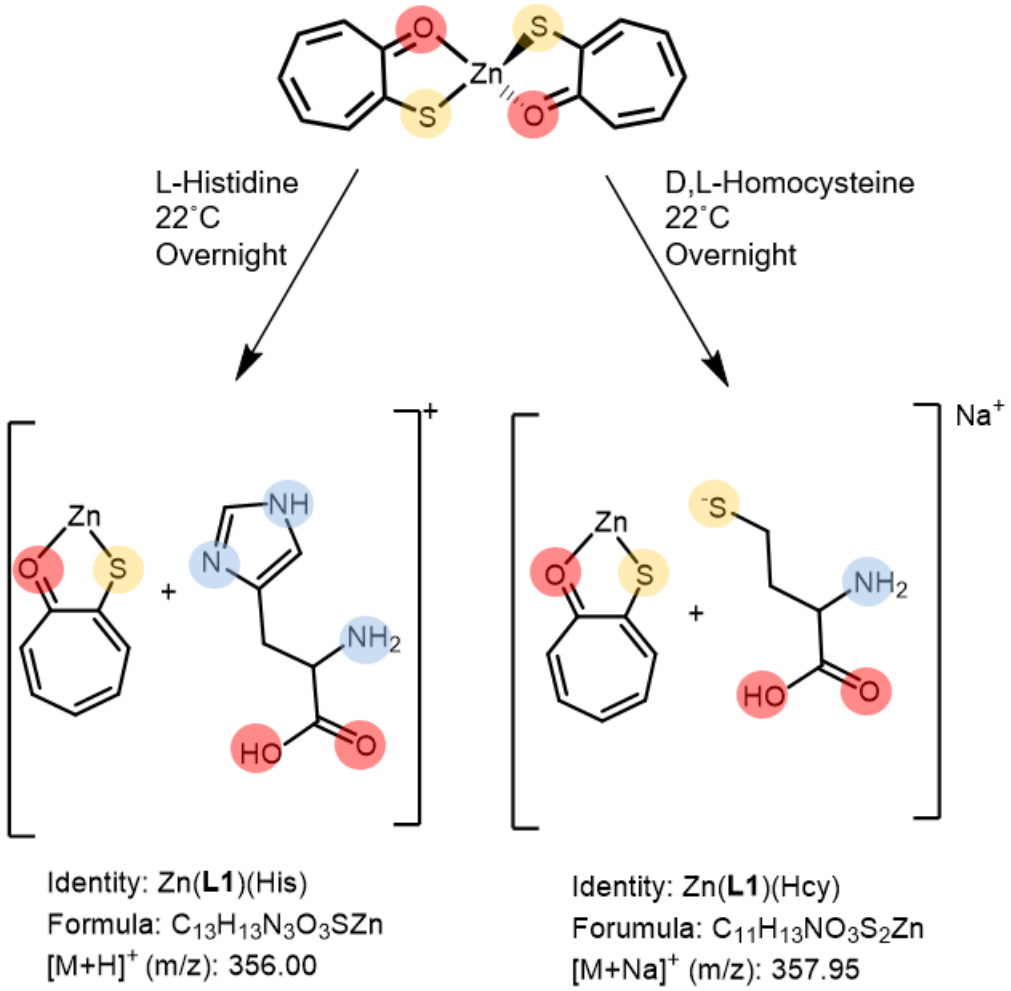

Figure 3.4: Products observed for reaction of Zn(**L1**)$_2$ with L-Histidine (left) and Homocysteine (right) with corresponding formula and (m/z) given.

As shown in earlier work on SC1M^{pro}, the binding of appropriate ligands to Zn can change its mode of inhibition from non-competitive to competitive, as well as improve the resulting K_i values.[115, 117] According to the hypothesis we are examining, two coordination sites should be liberated in order for Zn to interact with the catalytic dyad. The lability of the ligands was probed by examination of scrambling in mixtures of Zn(**L1**)$_2$ and Zn(**L2**)$_2$ in DCM. The mass spectrum of

samples taken from the 1:1 mixture following 2 h of stirring found signals indicating a statistical distribution of the two parent complexes along with the appearance of a signal at (m/z) 380.99 **Figure B.12** and **B.13**, corresponding to $C_{17}H_{17}O_2S_2Zn$, the expected composition of the mixed ligand Zn(**L1**)(**L2**) complex.

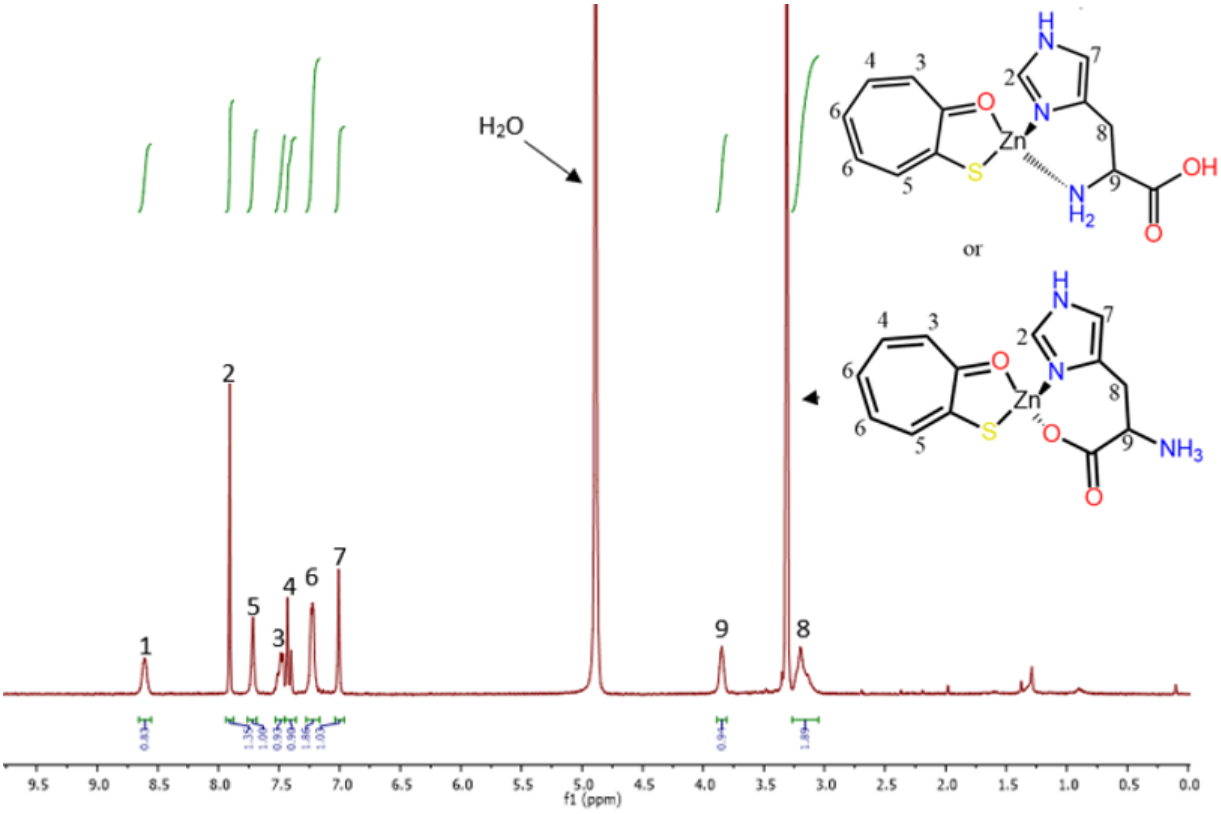

Figure 3.5: ^{1}H NMR of the reaction of Zn(**L1**)$_2$ with L-Histidine in MeOH-d$_4$ referenced to TMS via residual MeOH with a potential structures of the adduct given.

The ligand scrambling result was corroborated by reactions with exogenous biological ligands. Reaction of Zn(**L1**)$_2$ in MeOH with 4 equiv. of L-Histidine (His) at 50°C for ca. 1 h resulted in a color change from yellow to orange and yielded a single displacement product **Figure 3.4** (left). This was characterized by ^{1}H-NMR **Figure 3.5**, and $^+$ESI-MS, **Figure B.10**, the [Zn(**L1**)(His)]$^+$ adduct. A similar reaction and product resulting from a single **L1** replacement with homocysteine (Hcy) resulted in [Zn(**L1**(Hcy)]Na$^+$ (**Figure 3.4** (right) and **Figure B.9**) via $^+$ESI-MS. The same

is true for a molecular NS mimic **Figure B.11**. Taken together, these results indicate that in the presence of either His or Cys, one bidentate thiotropolone **L** can be displaced, thus opening up two coordination sites at which basic residues might bind.

3.2.5 SC2M^{pro} Inhibition Studies

To characterize the IC_{50} values of each compound, SC2M^{pro} was expressed and purified according to a published protocol.[133, 155] Building upon the established fluorescent peptide assay system (details in Chapter II), the IC_{50} values for inhibition of SC2M^{pro} were measured for the ligands alone, $Zn(NO_3)_2$ alone, $Zn(NO_3)_2$ in the presence of 0.5 μM of ligand, and the intact $Zn(\mathbf{L})_2$ complexes **Figure 3.6**. These values were compared to a number of other ligands from a library reported by Cohen *et al.*[10, 2], which were screened to determine those that offered increased inhibition of SC2M^{pro} relative to $Zn(NO_3)_2$ alone. The **L** ligands alone have high IC_{50} values (8 $\breve{}$ 34 μM), **Figure 3.6 A**, demonstrating that 0.5 μM ligand by itself provides little inhibition of enzyme activity. However, $Zn(NO_3)_2$ alone inhibits SC2M^{pro} at low concentrations ($IC_{50} = 101 \pm 9$ nM) **Figure 3.6 C** (black). This is improved upon addition of 0.5 μM **L1 Figure 3.6 B** (orange) which enhances inhibition by Zn^{2+} ($IC_{50} = 59 \pm 6$ nM) while 0.5 μM **L2 Figure 3.6 B** (green) has little effect on zinc-based inhibition ($IC_{50} = 97 \pm 5$ nM). Under the same conditions, addition of 0.5 μM of Trop (blue, $IC_{50} = 119 \pm 6$ nM) and HK (black, $IC_{50} = 190 \pm 10$ nM), did not result in an enhancement in efficacy. Additionally, the $Zn(\mathbf{L1})_2$ complex **Figure 3.6 C** (orange) shows improvement in inhibition potency ($IC_{50} = 79 \pm 6$ nM) compared to $Zn(NO_3)_2$. Enhancements in inhibition, particularly for Zn-**L1** combinations, results in greater efficacy compared to the individual components. These complexes provide another example of metal-based inhibitors of SC2M^{pro} comparing favorably with the rhenium tricarbonyl inhibitors recently reported by Cohen, *et al.*[142] The IC_{50} values for the latter are in the low μM range while the values for the Zn complexes investigated here fall in the 50-100 nM range.

Seeking to determine the optimal Zn/**L** ratio, $[Zn(NO_3)_2]$ was held constant at 100 nM while the concentrations of **L1** or **L2** were varied as shown in **Figure 3.7 A** and **B**. These data are normalized to percent activity in the presence of 100 nM $Zn(NO_3)_2$; therefore values below 100% indicate an

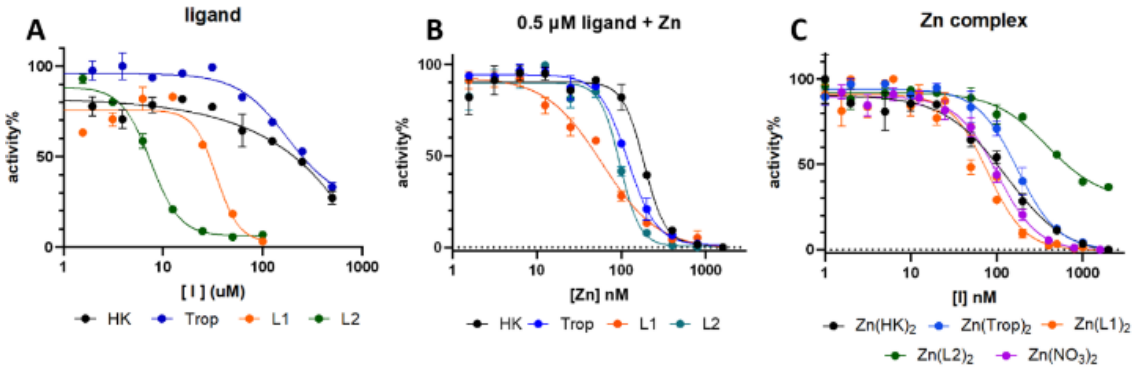

Inhibitors	IC_{50} (µM)	Inhibitors	IC_{50} (nM)	Inhibitors	IC_{50} (nM)
HK	/	0.5 µM HK + Zn	190 ± 10	$Zn(HK)_2$	130 ± 30
Trop	/	0.5 µM Trop + Zn	119 ± 6	$Zn(Trop)_2$	180 ± 20
L1	34 ± 6	0.5 µM L1 + Zn	59 ± 6	$Zn(L1)_2$	79 ± 6
L2	8 ± 1	0.5 µM L2 + Zn	97 ± 5	$Zn(L2)_2$	400 ± 100
				$Zn(NO_3)_2$	101 ± 9

Figure 3.6: The inhibition curves of (A) ligands alone; (B) constant 0.5 μM ligand and increasing [$Zn(NO_3)_2$]; and (C) the intact Zn-complexes toward $SC2M^{pro}$. A four-parameter IC_{50} equation (**Equation S1**) was fit to the data to determine IC_{50} values which are presented in the associated table.

enhancement of inhibition relative to $Zn(NO_3)_2$ alone. At concentrations of less than 10 μM added **L1** or **L2**, inhibition is enhanced (activity < 100%), with the effect being maximized at 1 μM for **L1** and 0.5 μM **L1** (blue shaded). This enhancement in inhibition was not observed for other ligands tested, such as the zinc ionophores chloroquine and hydroxychloroquine,[158, 159, 2] which didn't display enhancement until the ca. 30-50 μM range under the same conditions. However, at [**L**] greater than 10 μM, this improvement was diminished and catalytic activity increased (red shaded). These results suggest competition between Enzyme E and free **L** for binding to $Zn(\mathbf{L})^+$, **Figure 3.7 C**, indicating that a sufficient concentration of free **L** can outcompete the enzyme for the open coordination sites on Zn^{II} to form E and $Zn(\mathbf{L1})_2$. This behavior has been observed in studies of metals acting as inhibitors of Zn-dependent proteases.[154, 10] Inhibition at large excesses of **L** (green shaded) may be due to a combination of binding $Zn(\mathbf{L})_2$ and **L** as the [**L**] in this regime is close to the IC_{50} values observed for the free ligand **Figure 3.6 A**. This is consistent with studies

of Zn-complexes acting as inhibitors of the SC1M^{pro} as well as recent computational investigations on SC2M^{pro}.[160] The interpretations of these data are summarized in the equilibria of **Figure 3.7 C**.

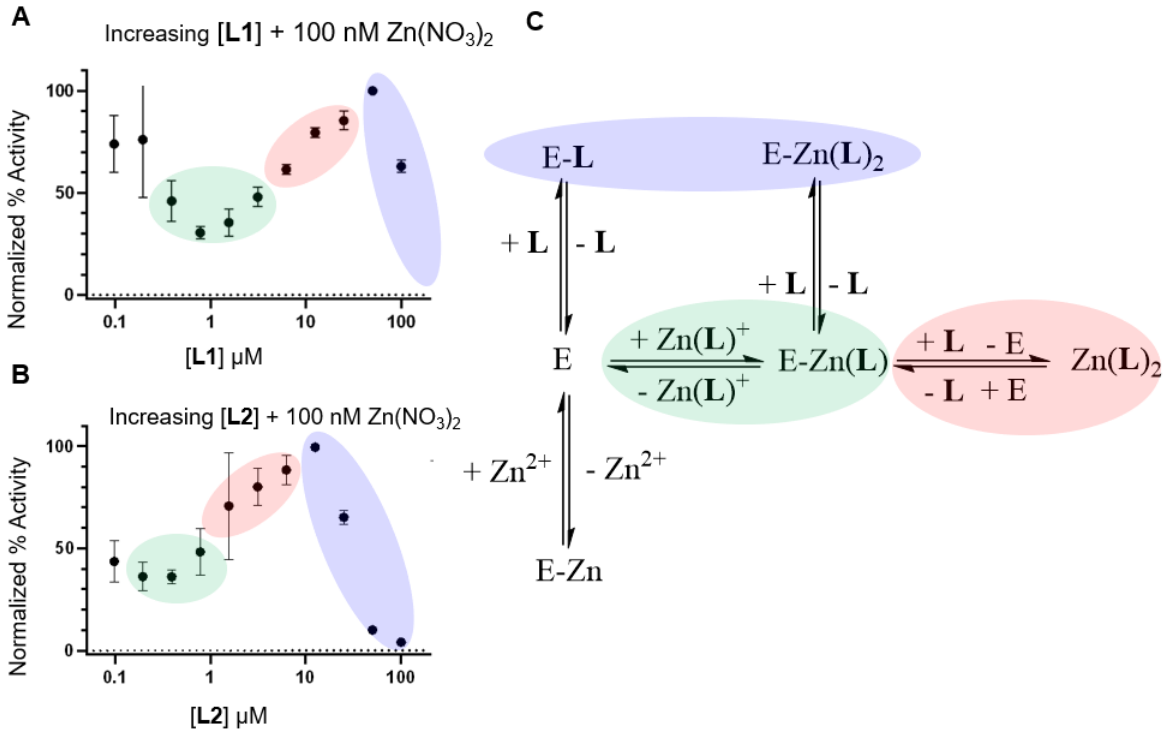

Figure 3.7: % Activity normalized to 100 nM [$Zn(NO_3)_2$]. (A) [$Zn(NO_3)_2$] is held constant at 100 nM while [**L1**] is varied. (B) [$Zn(NO_3)_2$] is held constant at 100 nM while [**L2**] is varied. (C) Proposed mechanism of inhibition by $Zn(\mathbf{L})^+$ with off pathway $Zn(\mathbf{L})_2$. Color coded regions of (A) and (B) correspond to the associated sections in (C).

3.2.6 Computations

Computational protein docking programs such as AutoDock have guided development of small molecules as inhibitors of proteases including the SC2M^{pro}. An advanced version, AutoDock4, has probed copper complexes as potential inhibitors of the novel coronavirus.[140] Unfortunately this *in silico* stratagem struggles to unambiguously inform on bond-forming processes for metal-containing inhibitors. While tentative results can be obtained, Autodock cannot provide energies

relating to metal-ligand coordinate covalent bonds. An improvement made by Cohen, *et al*., added size and charge, generating an "active" metallo fragment for favorable electrostatic interactions with the catalytically active Cys145. This inhibition prediction for the organometallic Re^{I} system was experimentally supported, although a crystal structure of the protein-organorhenium complex is currently not available.[142] As a way of validating the methodology employed herein and the resulting conclusions, the structure of Zn-1,2-toluenedithiolate [Zn(TDT)] bound to $SC1M^{pro}$ was compared to the computational docking result. The "active" metallo fragment Zn(TDT), computations found it to be positioned between the catalytic dyad, similar to the crystal structure as overlaid in **Figure 3.8**.

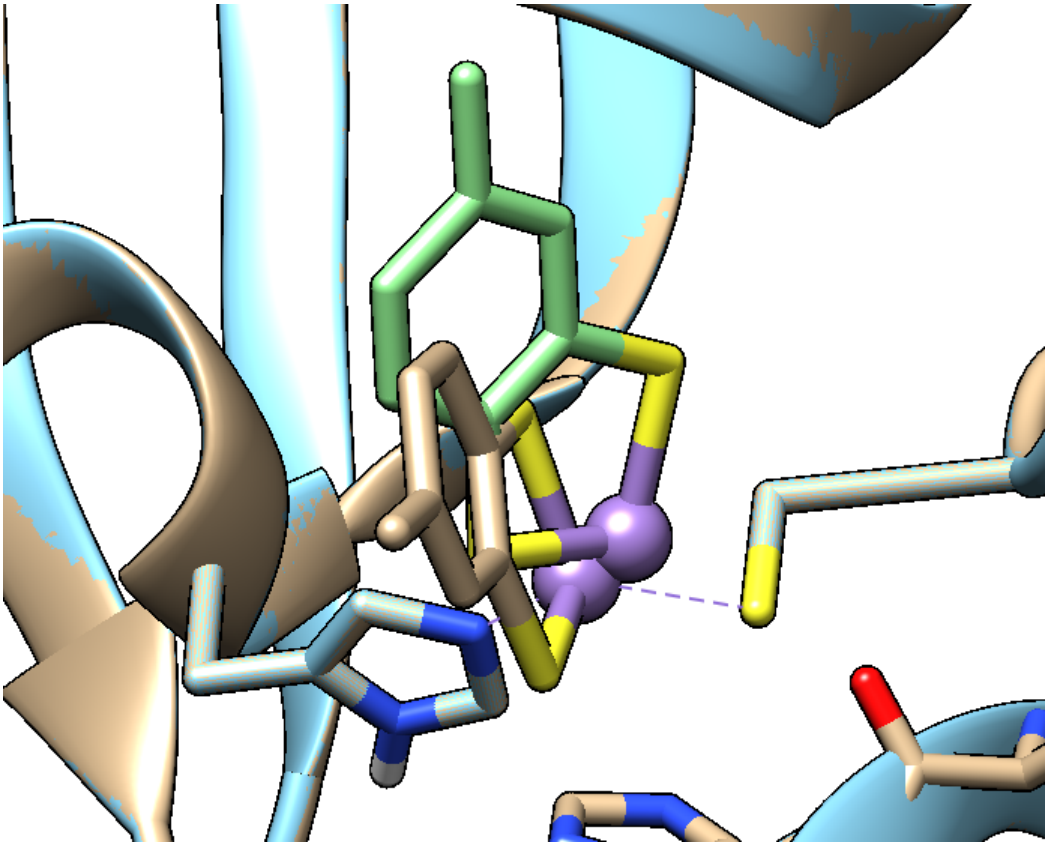

Figure 3.8: Binding poses generated from AutoDock4 calculations with Zn(TDT) [green] overlaid with the Zn fragment from the crystal structure [tan] (PDB: 2Z94). The catalytic dyad of His41 and Cys145 have been labelled for clarity.

For our computations, the free thiotropolone ligands were compared to both the bis- and mono-ligated Zn^{2+} complexes ($Zn(\mathbf{L1})^{+}$) according to the protocol described in the **SI**.† For each case, a potential inhibitor was offered to the entire surface of the protein, without bias toward the presumed active site, i.e., blind docking, see **Figure 3.1**. Analysis of the top 10 binding scores for each fragment found ca. 6 poses clustered at the active site Cys145-His41 dyad. Such clustering not observed for other surface accessible bases. Simulations were then performed with repeated active site dockings. For these preferred poses, the charge of the protein at that site was calculated using its active state, i.e., deprotonated Cys145.

The lowest relative energy of binding of each of the free thiotropolones, **L1**, **L2** and **L3**, was found for occupancy of the hydrophobic S2 pocket at the Cys145-His41 active site; however orientation towards Cys44 or Cys145 was not optimal for a covalent attachment via a disulfide-based inhibition. This is consistent with the relative inactivity of the ligands towards inhibition (IC_{50} values in μM range, **Figure 3.6 A**).

However, upon coordination of Zn, a shift in the binding mode finds that the thiotropolone of $Zn(\mathbf{L1})^{+}$ settles into the S1 binding pocket, with the Zn positioned 2.176 Å from Cys145, 2.454 Å from the amide-O of His164, and 4.224 Å from the His41 N-donor **Figure 3.9** (green). Due to the tight fit of the $Zn(\mathbf{L1})^{+}$ in the S1 pocket, addition of steric bulk in the form of isopropyl groups on the ligand backbone prevents $Zn(\mathbf{L2})^{+}$ (red) and $Zn(\mathbf{L3})^{+}$ (purple) from occupying the analogous position. Instead, the isopropyl group of $Zn(\mathbf{L2})^{+}$ is better placed in the hydrophobic S2 binding pocket shifting the Zn closer to the catalytic dyad (2.299 Å from Cys145, and 4.096 Å from His41). Addition of the iPr to the 6 instead of the 4 position results in $Zn(\mathbf{L3})^{+}$ binding to a basic residue outside of the dyad and on the edge of the pocket, Glu166 (see the purple pose with Zn-Glu distance of 1.636 Å). Although Glu166 is not involved in the specific nucleophilic attack on substrate, the binding of the metal to residues that are not essential to the protease mechanistic cycle might have broader deleterious effects on the protein. Such was suggested by Gray, Garza-Lopez, *et al.*[140, 139] with other non-dyad residues such as Cys44.[161] We conclude that the presence of Zn^{II} bound to the thiotropolones, **L**, increases affinity, i.e., produces a more negative

value for the binding energy, for the SC2M^{pro} active site compared to **L** alone.

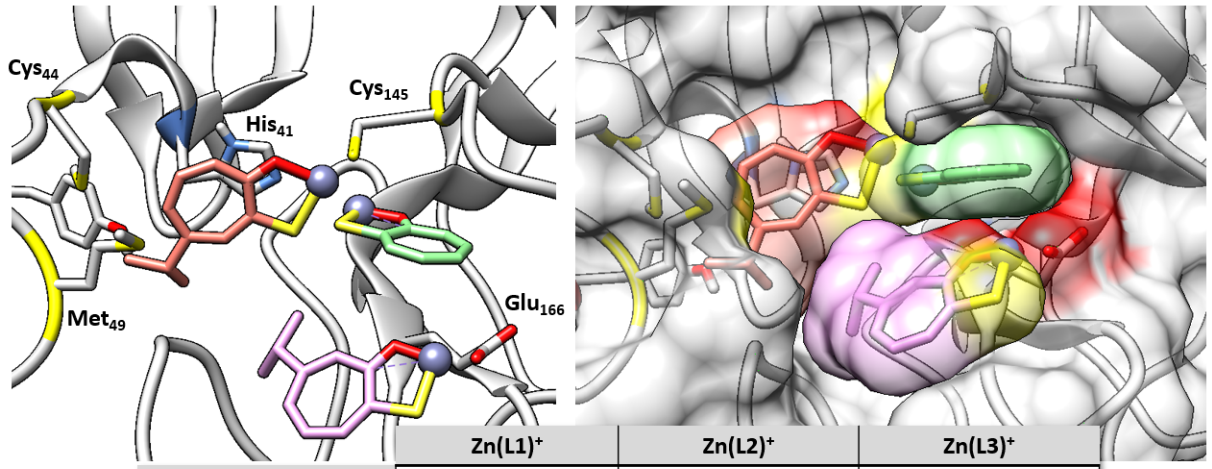

	Zn(L1)$^+$	Zn(L2)$^+$	Zn(L3)$^+$
Estimated free energy of binding (kcal/mol)	-5.49	-5.57	-5.74
Distance to metal binding residue	2.176 Å (S-Cys$_{145}$) 2.454 Å (O$_{am}$-His$_{164}$)	2.299 Å (S-Cys$_{145}$) 4.096 Å (N-His$_{41}$)	1.636 Å (O-Glu$_{166}$)

Figure 3.9: Binding poses generated from AutoDock4 calculations on SC2M^{pro} (PDB: 6W63) using the metallo fragments Zn(**L1**)$^+$ [green], Zn(**L2**)$^+$ [red], Zn(**L3**)$^+$ [purple]. [Left panel]: The final docked poses of the three Zn(**L**)$^+$ fragments with relevant metal binding residues labeled using their three letter designator and sequence position. [Right panel]: Same image but with the addition of the calculated molecular surface. All images generated using UCSF Chimera ref. 127.

It is notable that the mono-ligated Zn(**L**)$^+$ complexes are found by computations to bind in an alternate part of the protease binding pocket than was experimentally observed in the crystal structure of the Zn(TDT)-inhibited SC1M^{pro}.[117] Although the two proteases from the two coronaviral strains have nearly identical sequences surrounding the active site, data suggest that the dynamic binding pocket of SC2M^{pro} is both smaller and more flexible than SC1M^{pro}.[135] This feature could lead to alternative optimal orientations for inhibitors of the two viruses, and the subtle differences noted in our study rendered cautionary for general conclusions.

As 5-coordinate zinc complexes are common, the intact, bis-ligated complexes, Zn(**L1**)$_2$, Zn(**L2**)$_2$, and Zn(**L3**)$_2$, might reasonably bind through zinc, and amplified by the organic ligand appendages. While the direct electrostatic interaction of zinc ion in this form to the catalytic His/Cys dyad was

not evident in the computations, the ligands controlled favorable interactions into the S1 and S2 binding pockets. Based on studies of coordinatively saturated metal complexes as inhibitors for adenylyl cyclase by Chen *et al*.,[162] van der Waals interactions between the protein and the intact metal complex could be similar to those of organic small molecule inhibitors and dictate the efficacy of the presumed therapeutic.

3.3 Conclusions

The role of metals as carriers and adjuncts of small organic molecules, for potential therapeutics is just beginning to attract attention in the realm of SARS-CoV-2. The above results are unique in that they derive from various approaches: establishing fundamental properties that are useful to delineating stability; determining potential for co-binding of metal/ligand/active site residues; interpretation of enzyme inhibition assays; and, guidance from computational docking studies. The salient conclusions from this study of bis-thiotropolone-zinc complexes for inhibition of $SC2M^{pro}$ are as follows:

- With the caveat that comparisons between IC_{50} determinations across studies can be fraught with ambiguities due to differences in assay conditions, it appears that those derived in our determination of the Zn/**L** systems here (in the range of 60 -100 nM) are superior to the (currently) only known metal complex inhibitor of $SC2M^{pro}$, i.e., Cohen's rhenium carbonyl system in the range of 7–30 μM).[142]

- Partition between aqueous buffer medium and 1-octanol indicates lipophilicity is engendered on binding of Zn^{2+} by **L1** and **L2**. This portends that such ligation will enhance cell membrane permeability, studies that are currently underway.

- The affinity of thiotropolone for Zn^{2+} is responsible for a single S-O ligand displacement, particularly towards imidazole-containing species. This indicates potential for dative bond formation between $Zn(\mathbf{L})^{+}$ and basic residues.

- Regardless of administration as separated components or as intact complexes, the sterically

simpler thiotropolone, **L1**, increases by ca. 20-40% the Zn-based inhibition of SC2M^{pro} *in vitro*, while this enhancement is not observed for the 2-O parent tropolones.

- Computational docking points to the preferential association of Zn(**L**)$^{+}$ within the substrate binding pocket relative to **L** alone. Whether there is coordinate covalent bonding between Zn and the dyad awaits experimental verification.

In addition, the Zn-ionophore complex bis-pyrithione-Zn is a known inhibitor of SARS-CoV-1 RNA Dependent RNA Polymerase (RdRP).[108] Due to the high degree of sequence homology (82%) between SARS-CoV-1 RdRP and SARS-CoV-2 RdRP,[101] combinations of Zn^{2+} and **L** could inhibit this secondary viral target as well. It is also noteworthy that Zn(**L1**)$_2$ is known to a) display hypoglycemic activity in diabetic mice; b) in such cases the thiotropolone outperforms the 2-O and 2-S derivatives, sustaining a high level of Zn in the organism for a period of days via both intravenous and oral administration.[46] In these studies, the optimal donor combination appears to be SO, as was found here.

In summary, we have demonstrated that S-substituted thiotropolones work in harmony to modestly increase the efficacy of $Zn(NO_3)_2$ as an inihibitor of SC2M^{pro} *in vitro*, an improvement that is not observed when zinc is administered alongside the analogous 2-oxy tropolones. This result is attributed to the enhanced binding to zinc that the thiolate/thione provides. While an enzyme/zinc/ligand ternary complex is indicated only by inference, our study points to an avenue for expansive design of potential therapeutics by adapting the well-known governing features of coordinate covalent complexes, as has been highlighted in a recent review by Cohen *et al*.[163] These include specific geometries, control of thermodynamics and kinetics of ligand binding/dissociation, and steric modification of linkages between ligand donor sites for a better match to the active site pockets. The advances in computational modelling over the past two decades are critical to defining the available experimental space.

4. EFFECT OF METAL IDENTITY AND COORDINATION SPHERE ON METAL-BASED INHIBITION OF THE SARS-COV-2 MAIN PROTEASE[1]

4.1 Introduction

The cluster of pneuomonia cases that appeared in Wuhan, China in late 2019,[1] later identified as SARS-CoV-2 (SC2), became the defining story of 2020 and remains a critical issue throughout the world. It spawned a massive scientific effort to identify therapeutics to stem the tide against the virus while vaccines were developed.[101, 100] The continued emergence of new variants of SC2, some of which have been shown to infect those who have been vaccinated, spurs research into medicinals targeted at the main protease of SC2, SC2M^{pro}. Early in the outbreak, a number of reviews and speculative reports pointed to the potential for zinc, as stand alone or in combination with other therapeutics, to act as an inhibitor of SC2.[100, 149, 148, 120, 151, 164, 150] Zinc was first demonstrated to have antiviral effects in 1974,[143] and since then has shown efficacy across a wide range of infections.[165, 119, 145, 89, 111, 121] One of the ways that Zn is known to act is by binding to essential viral proteins, blocking function. An excellent example of this can be seen in the closely related SARS-CoV-1 (SC1) where Zn coordination complexes were found via protein crystallography to form adducts with the His-Cys dyad of the viral main protease (SC1M^{pro}).[115, 117] Our initial investigations built on this knowledge, aiming to evaluate Zn as an inhibitor of the main protease of SARS-CoV-2 (SC2M^{pro}).[2] It was found that combinations of Zn^{2+} and lipophilic thiotropolone derivatives (**L**) (IC_{50} ca. 60-80 nM) were more effective than $Zn(NO_3)_2$ (IC_{50} ca. 100 nM) or the ligands alone (IC_{50} ca. 10-35 μM) for the inhibition of SC2M^{pro} *in vitro*. Computations placed the Zn(**L**)$^+$ metallofragments at the active site, indicating that binding to the catalytic His41-Cys145 dyad of SC2M^{pro} is feasible just as seen in SC1M^{pro}.

In addition to zinc, there have been a number of other metals and metal complexes that are

[1]Reprinted with permission from "Dinitrosyl iron complexes (DNICs) as inhibitors of the SARS-CoV-2 main protease" by D. Chase Pectol,[a] Christopher R. DeLaney,[a] Jiyun Zhu,[b] Drake M. Mellott,[b] Ardala Katzfuss,[b] Zane W. Taylor,[b] Thomas D. Meek,[b] and Marcetta Y. Darensbourg[*a] , 2021. Chemical Communications, Copyright 2021 by Copyright Royal Society of Chemistry.

proposed to have potential as inhibitors of SC2M^{pro}[100] including gold,[132] copper,[140] and cobalt.[139] Gold phosphines are known to bind to free thiols on proteins, as seen in a protein-MS study by Zoppi and coworkers.[166] This is significant as SC2M^{pro} relies on its catalytic Cys145 for activity. It also contains other active site cysteinyl residues, found in the investigations into Cys44 by Verma *et al*.,[161] that have been identified as targets for potential therapeutics. Auranofin, a gold-containing anti-rheumatic drug shown in **Figure 4.1 A**, was tested against Vero E6 cells infected with SC2, and it was found to have an effective inhibitory concentration (EC_{50}) of 1.4 μM. In addition, gold nanoparticles functionalized with glycans have been shown to block the binding of the viral spike protein to the receptors on the surfaces of cells, a crucial step in the infection process for viruses such as Ebola and SC2, with IC_{50}'s as low as picomolar.[167]

Copper is often used in antimicrobial surfaces and copper salts, such as copper gluconate depicted in **Figure 4.1 B**, are reported to have modest efficacy in the reduction of infection rate in Vero E6 cells by SARS-CoV-2.[141] In this study, Rodriguez *et al*. determined that preincubation of the cells with 25, 50, and 100 μM copper gluconate reduced infection rates when exposed to SC2 by 71, 77, and 78% respectively relative to control cells . However, this is far above what is considered normal in whole blood (15 μM or 1000 μg/mL) and greatly exceeds what would be expected in tissue (1-12 μg/mL) with the complete elimination of infection not observed even at 200 μM added copper gluconate. Whether the promise displayed by copper coordination complexes against other viruses, such as the $Cu(HK)_2$ complex that has displayed activity against human influenza virus,[98] can translate to SC2 remains to be seen.

Cobalt complexes have also been investigated as inhibitors of Human Immunodeficiency Virus (HIV) protease, the enzyme responsible for polyprotein processing for the deadly infection. This activity is analogous to the reaction carried out by SC2M^{pro}, i.e. it serves the identical function of cleaving the HIV polyprotein as part of the viral replication cycle. A series of inorganic polyhedral metallacarboranes **Figure 4.1 C**, linker-substituted dual-cage cobalt bis(dicarbollides), were tested to determine the effect of linker identity on inhibition of HIV protease. Depending on the length and identity of the linker between the two cobalt metallofragments, IC_{50} values as low as ca. 3 nM

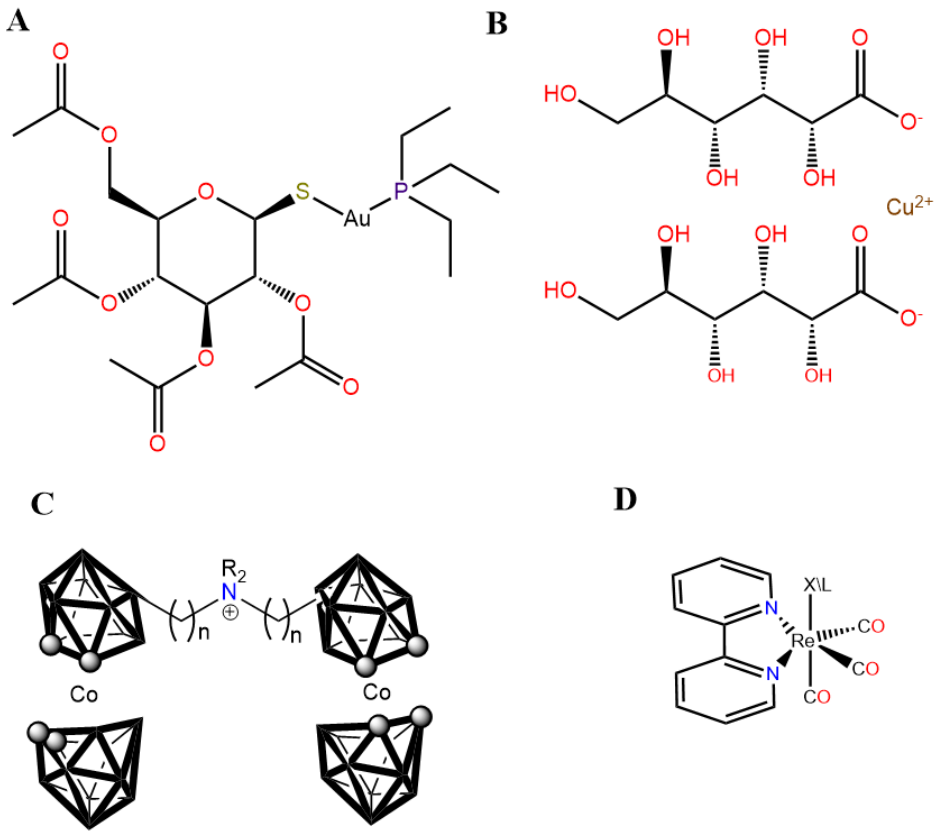

Figure 4.1: Selection of metal complexes found to inhibit viral. (A) Auranofin was found to be effective against SC2 in Vero E6 cells. (B) Copper Gluconate was found to reduce the rate of infection of Vero E6 cells. (C) Cobalt bis(dicarbollide) derivatives with various linker lengths (n) and R group identities were found to inhibit HIV protease, and (D) Rhenium tricarbonyl bipyridine derivatives with X = Cl or L = H_2O were found to inhibit $SC2M^{pro}$ *in vitro*.

were achieved.[168] Kinetic analyses indicate that this activity results from the complexes' ability to compete with the native substrate for active site binding.

One of the most intriguing studies of a metal-based SC2 inhibitor is found in a recent report by Cohen *et al.* in which derivatives of the organometallic Rhenium tricarbonyl bipyridyl $[Re^{I}(CO)_3(bipy)]$ moiety **Figure 4.1 D** are explored as inhibitors of $SC2M^{pro}$. In these studies, it was found that substitution of the apical Cl^- with H_2O improved inhibitor efficacy from ca. 20 μM to 7 μM for select derivatives. This makes sense in the light of the fact that the most likely mode of inhibition is through binding of Cys145 to an open apical site, found in both protein-MS studies and computational modeling of the metallofragment, $[Re^{I}(CO)_3(bipy)]$, in association with $SC2M^{pro}$.

These MS studies are particularly insightful, as they demonstrate that if Cys145 is blocked by attachment of a covalent inhibitor prior to exposure to $[Re^{I}(CO)_3(bipy)]$, the metallofragment does not bind to the protein. However, when the two are incubated together in the absence of the covalent inhibitor, the mass spectrum shifts by 427 mass units relative to Apo SC2M^{pro}. The resulting parent peak has an (m/z) matching that of SC2M^{pro} plus the $[Re^{I}(CO)_3(bipy)]$ unit. Taken together, these results indicate that metallofragments such as $[Re^{I}(CO)_3(bipy)]$ may be used to selectively inhibit SC2M^{pro}.

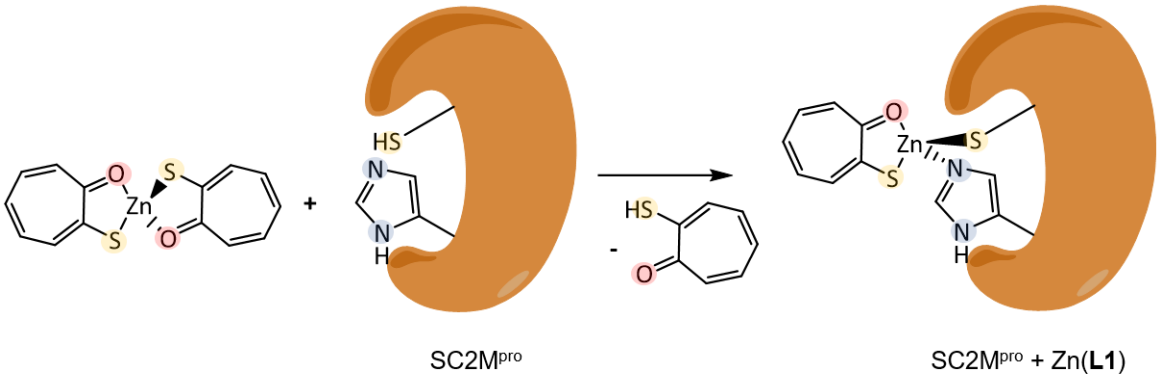

Figure 4.2: Proposed mechanism of SC2M^{pro} inhibition observed for Zn(**L**)$_2$ complexes. Ligand displacement of one thiotropolone opens the two coordination sites necessary to bind the catalytic Cys145-His41 catalytic dyad.

With transition metals other than zinc having success as inhibitors of SC2, we sought to expand on the system we explored in our previous work, generating a number of first-row metal-thiotropolone complexes which were then compared to the known Zn-thiotropolone SC2M^{pro} inhibitors.[2] Herein, we report the syntheses and characterization of first row transition metals in complex with thiotropolone (**L1**) along with their efficacy as inhibitors of SC2M^{pro} *in vitro*. The effect of the first coordination sphere on Zn-based inhibitor potency is also explored, with O4, S2O2, and S4 coordination modes compared to relate ligand-Zn affinity to the inhibitory activity of the Zn(**L**)$_2$ complex. Given that ligand lability is one of the governing factors in the efficacy

of therapeutic metal complexes,[163] we expect there will be a sweet spot for inhibition. Ligands possessing affinities higher or lower than this value will lead to less effective inhibitory combinations. In addition, Native Mass Spectrometry (Native MS) is used to investigate the identity of the metallofragments that may be interacting with SC2M^{pro}. A cartoon of the proposed binding of a Zn(**L**)$^{+}$ metallofragment to the catalytic dyad of SC2M^{pro} is given in **Figure 4.2**.

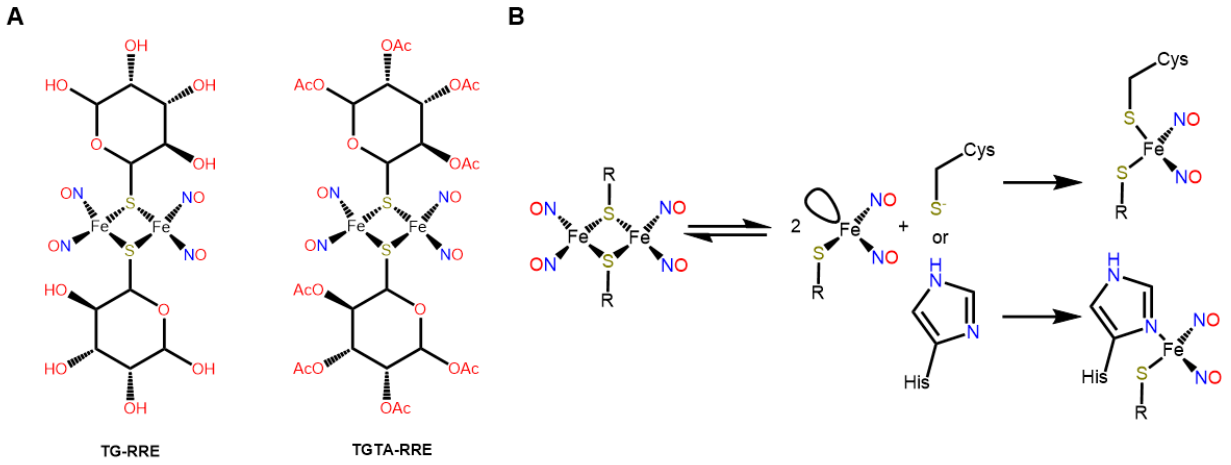

Figure 4.3: (A) ChemDraw structures of [(μ-S-TG)Fe(NO)$_2$]$_2$ (left) and [(μ-S-TGTA)Fe(NO)$_2$]$_2$ (right). (B) Scheme displaying the of reactivity of RRE-DNICs with biological bases Cysteine and Histidine. This reactivity motivates the study of these complexes as inhibitors of SC2M^{pro}. Figure adapted from Pectol *et al*. ref. 175.

As seen in Cohen *et al*.'s Re^{I}(CO)$_3$(bipy) inhibitor system, metal complexes containing diatomic ligands can serve as platforms for the development of therapeutics. A related class of medicinally viable metal complexes that contain diatomic ligands are Dinitrosyl Iron Complexes (DNICs).[169, 170, 171, 172] Under the correct conditions, these complexes may also possess the stability necessary to associate with protein active sites and inhibit function. To this point, Cesareo *et al*. actually obtained a crystal structure of a DNIC with glutathione ligands in complex with human glutathione transferase P1-1.[173] As part of our investigations into the efficacy of various metal complexes against SC2M^{pro}, we examined the effect of two dimeric Roussin's

red ester (RRE) DNIC's [(μ-SR)Fe(NO)$_2$]$_2$, bearing μ-SR ligands derived from two thiolated glucose moieties, 1-thio-β-d-glucose tetraacetate (TGTA) and 1-thio-β-d-glucose ligands (TG), [(μ-S-TG)Fe(NO)$_2$]$_2$ (TG) against the enzyme *in vitro*.[122] These two compounds, [(μ-S-TGTA)Fe(NO)$_2$]$_2$ and [(μ-S-TG)Fe(NO)$_2$]$_2$ depicted in **Figure 4.3 A** , have been shown in previous studies to be a working form of NO in a cellular environment.[174] They also react with cellular bases,[175] such as the Cys and His of the SC2M^{pro} catalytic dyad, depicted in **Figure 4.3 B**. For these reasons, their ability to act as inhibitors of SC2M^{pro} was investigated alongside the other M(**L**)$_x$ complexes.

4.2 Results

4.2.1 Syntheses and Characterization

The syntheses of the M(L)$_x$ were adapted from our previous report,[40] and proceed in 20-80% yields. In each case, a methanolic solution of one equivalent of the metal chloride salt and two ($NiCl_2$, $CuCl_2$) or three ($FeCl_3$, $CoCl_2$) equivalents of the ligand were stirred overnight, resulting in precipitation. The supernatant was then removed via cannula and the solid washed with copious amounts of methanol. X-ray diffraction (XRD) quality crystals were grown via slow evaporation of filtered dichloromethane (DCM) or d-chlorofrorm ($CDCl_3$) solutions of the metal complexes.

Dithiotropolone (**L4**) was first synthesized by Forbes and Holm in 1968 and used to make metal complexes of Zn and Ni.[41, 44] A more recent synthesis reported by Murakami *et al*. was utilized in my work.[46] Tropolone is reacted with an excess of Lawesson's reagent to generate **L4**. The crude product is extracted from an acidic water solution using DCM, dried, then reacted with $Zn(OAc)_2$ in methanol. The desired product, Zn(**L4**)$_2$, was isolated via column chromatography.[46] Further details of the synthesis and characterizations of these complexes (Mass Spectra, ^{1}H NMR spectra where applicable, Elemental Analysis of bulk samples, UV-vis spectra, and XRD crystal structures) are given in the Chapter II and the Appendices.

4.2.2 Molecular Structures

Slow evaporation of saturated solutions of the M(**L1**)$_x$ complexes yields crystals suitable for X-ray diffraction (XRD), giving the molecular structures seen in **Figure 4.4**. Both Ni(**L1**)$_2$ (B)

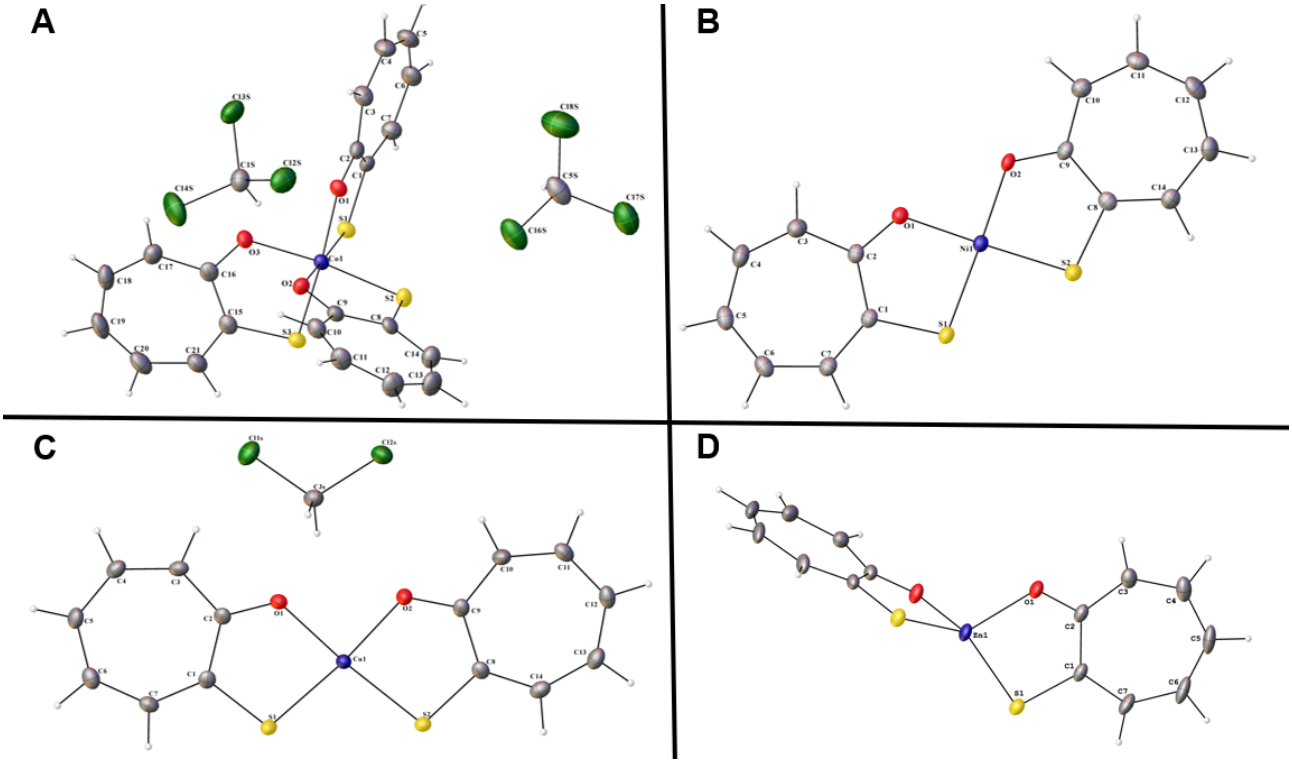

Figure 4.4: Molecular structures of (A) Co(**L1**)$_3$ (co-crystallized with two $CDCl_3$ solvent molecules), (B) Ni(**L1**)$_2$, (C) Cu(**L1**)$_2$ (co-crystallized with one DCM solvent molecule), and (D) Zn(**L1**)$_2$ from ref. 2 as determined by X-ray Diffraction. Full details are available in Appendix D.

and Cu(**L1**)$_2$ (C) crystallize in near ideal square planar configurations with $\tau_4{}'$ values of 0.028 and 0.083 respectively. This contrasts with the roughly tetrahedral geometry of Zn(**L1**)$_2$ ($\tau_4{}' = 0.695$) described in our previous report.[2] Ni(**L1**)$_2$ has Ni-S_{avg} bond lengths of and Ni-O_{avg} bond lengths of 2.131 Å and 1.873 Å respectively. This aligns well with previously reported SO mixed donor complexes of Ni, such as the bis-pyrithione complex reported by Chen *et al.*[176] The Cu(**L1**)$_2$ complex meanwhile has Cu-S_{avg} of Cu-O_{avg} lengths of 2.245 Å and 1.956 Å as expected for such SO complexes.[177] Interestingly, both of these complexes place the S donors on the same side of the complex **Figure 4.5**, **Figure D.2** and **D.3** i.e a symmetry of pseudo C_{2v} instead of D_{2h}. The Co(**L1**)$_3$ complex is octahedral **Figure D.1**, with Co-S_{avg} and Co-O_{avg} bond lengths of 2.191 Å and 1.941 Å respectively. While the Fe(**L1**)$_3$ complex has yielded crystals, they have proven too small for diffraction.

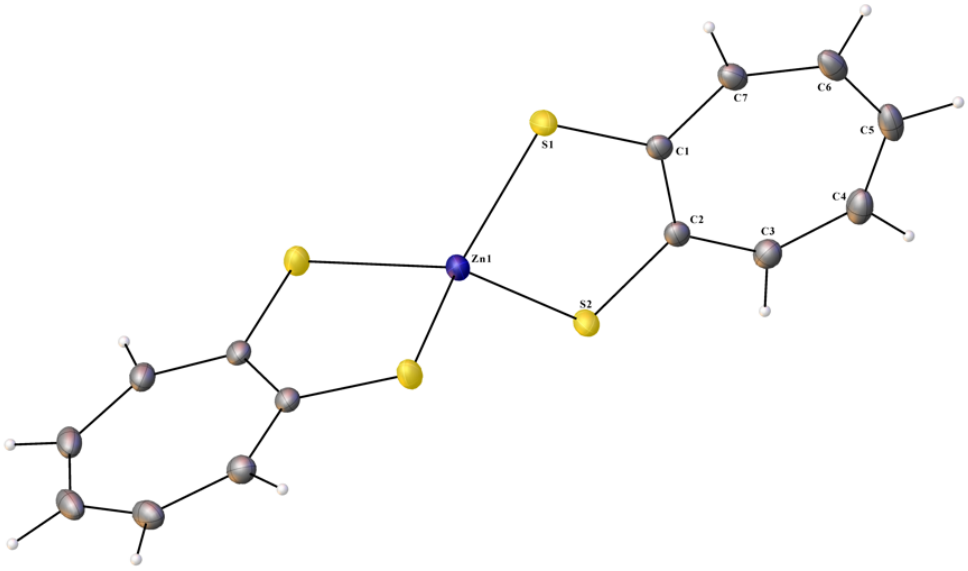

Figure 4.5: Molecular structures of Zn(**L4**)$_2$ as determined by XRD. Full details are available in Appendix D.

Likewise, slow evaporation of a saturated DCM solution of Zn(**L4**)$_2$ yields large, deep red crystals suitable for XRD. The molecular structure, displayed in **Figure 4.5**, has intraligand S_1-Zn-S_{2avg} bond angles of 90.64° and interligand S-Zn-S'_{avg} angles of 119.62° yield a roughly tetrahedral geometry ($\tau_4' = 0.856$), closer to an ideal tetrahedron than Zn(**L1**)$_2$. The complex has a Zn-S_{avg} bond length of 2.305 Å, slightly longer than the ca. 2.27 Å Zn-S_{avg} bond lengths of the SO Zn(**L1**)$_2$ and Zn(**L2**)$_2$ complexes. Just as is the case with the crystal packing of Zn(**L1**)$_2$, there appear to be π-π interactions present between the tropolone rings of Zn(**L4**)$_2$ in the solid state, with π-centroid distances of 3.60 Å.[39] The crystal packing and centroids can be visualized in **Figure D.8**.

4.2.3 SC2M^{pro} Inhibition

It is worth noting that the conditions of the assays described here are different than those in our previous report,[2] particularly with the inclusion of Bovine Serum Albumin (BSA) as a detergent at 0.5 mg/mL, much higher than the concentration of SC2M^{pro}. BSA is a known zinc

chelate,[178] and this is a likely explanation for the difference in observed inhibition of these Zn complexes between the two studies, as well as the increased importance of SO ligation in creating an effective inhibitor. While the difference in IC_{50} values between the zinc salt ($Zn(NO_3)_2$) and our best inhibitor complex Zn(**L1**)$_2$ was roughly 20% (101 nM vs 79 nM) in the first study, here we see a difference of nearly 5-fold between the K_i of $ZnCl_2$ (K_i = 1.95 μM) and Zn(**L1**)$_2$ (K_i = 430 nM) which again performed the best.

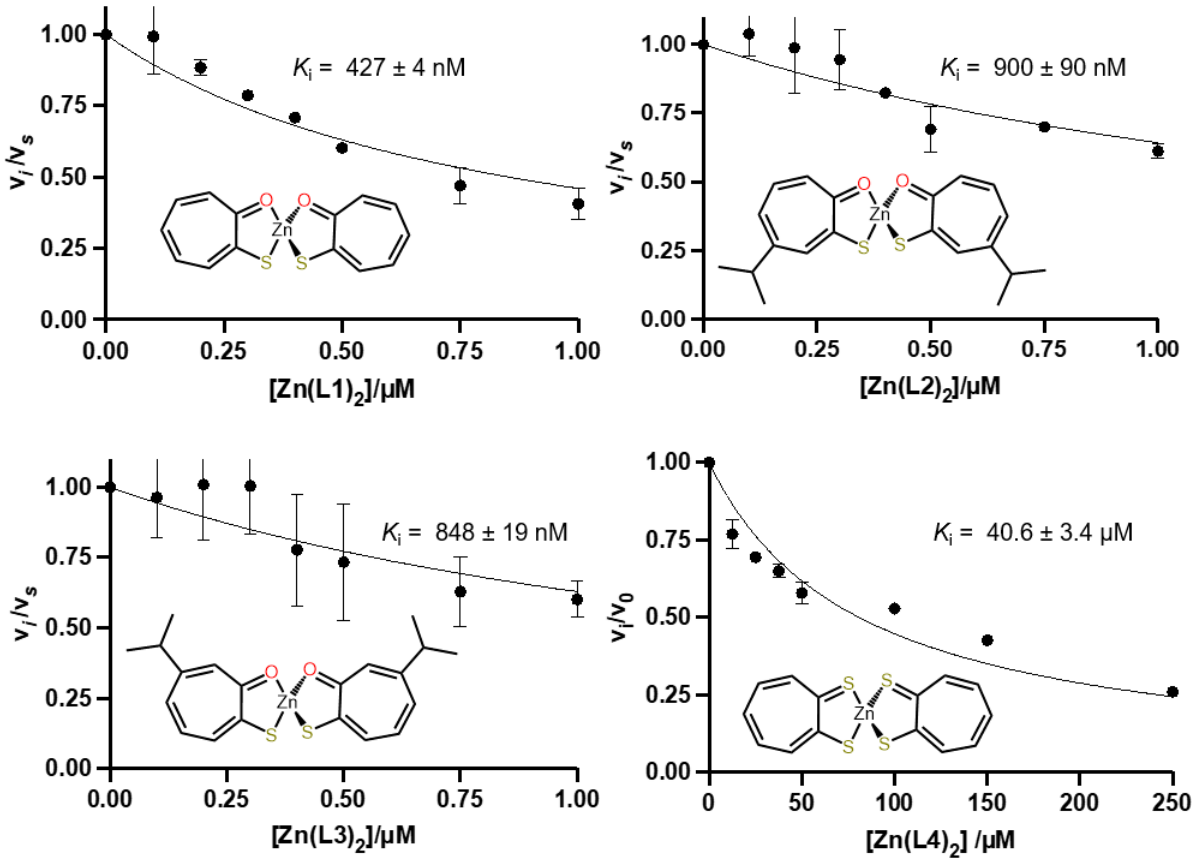

Figure 4.6: Concentration vs. velocity plots used to calculate K_i for Zn(**L1**)$_2$, Zn(**L2**)$_2$, Zn(**L3**)$_2$, and Zn(**L4**)$_2$. Molecular structures represented as ChemDraws for clarity.

Previous studies by Murakami *et al.* demonstrated that changing the donor-atom identity of tropolones can have a profound effect on the biological activity of the resulting Zn complexes.[46] In studies of the anti-diabetic activity of Zn-tropolone complexes, the S2O2 coordination mode

offered by **L1** provided the greatest boost to Zn activity while both the O4 and the S4 were an order of magnitude less effective *in vitro*. This difference was magnified in *in vivo* studies on mouse models. Here, we observe that the O4 coordination mode provided by $Zn(trop)_2$ ($K_i = 2.04 \pm 0.22$ μM) and $Zn(HK)_2$ ($K_i = 1.95 \pm 0.17$ μM) were nearly identical to that of $ZnCl_2$ alone ($K_i = 1.92 \pm 0.30$ μM) **Figure E.3**. When the S2O2 **L1**-**L3** bis-complexes were examined, it was found that $Zn(\mathbf{L1})_2$ provided the most robust enhancement in inhibition ($K_i = 427 \pm 4$ nM) while $Zn(\mathbf{L2})_2$ ($K_i = 900 \pm 90$ nM) and $Zn(\mathbf{L3})_2$ ($K_i = 848 \pm 19$ nM) both offered less enhancement when compared to the sterically simpler **L1** **Figure 4.6**. Finally, the S4 $Zn(\mathbf{L4})_2$ displayed the poorest efficacy of the tested Zn-complexes ($K_i = 40.6 \pm 3.4$ μM). Comparing these values to the known SC1 inhibitor $Zn(PT)_2$ ($K_i = 815 \pm 10$ nM) **Figure E.3**, $Zn(\mathbf{L1})_2$ with its S2O2 coordination mode and ideal lipophilicity ($LogD_{7.4} = 1.77$)[**?**] appears to be the most promising. These results align well with studies by Murakami *et al*. described above, and point to the importance in selecting the appropriate ligands when designing a metal-based inhibitor.[163]

Based on the computations performed by Gray *et al*.,[140, 139] as well as studies on $Cu^{II}(gluconate)_2$, we anticipated that Cu or Co salts or their complexes with **L** would display efficacy against $SC2M^{pro}$ *in vitro*. However, neither the chloride salts $CuCl_2$ ($IC_{50} = 173 \pm 19$ μM) and $CoCl_2$ ($IC_{50} = 407 \pm 47$ μM) **Figure E.1**, nor their complexes with **L1** $Cu(\mathbf{L1})_2$ ($IC_{50} = 65.8 \pm 7.9$ μM) and $Co(\mathbf{L1})_3$ ($IC_{50} = 52.6 \pm 4.2$ μM) showed efficacy *in vitro* **Figure 4.7**. It should be noted that in the computational studies by Kozak, Gray, and coworkers used coordinatively *unsaturated* complexes, thus leaving sites for dative bonding available.[140, 139] This is not the case here as the bidentate **L** ligands occupy these sites in our complexes. The same is true for the chloride salts **Figure E.1** and **L1** complexes **Figure 4.7** of Fe^{3+} and Ni^{2+} possessing K_i values of $30.0 \pm 2.2\mu$M and 72.4 ± 9.4 μM. The results of the assays are summarized in **Table F.2**- **F.5**. None of these metals provide the same level of inhibitory activity as $ZnCl_2$ alone (**Figure E.1**), being 1-2 orders of magnitude poorer. In addition, the K_i values for the $M(\mathbf{L1})_n$ complexes are not significantly better than **L1** alone **Figure E.2**. Taken together, we can conclude that from inhibition tests, none of the first-row transition metals when complexed to thiotropolone offer an improvement relative

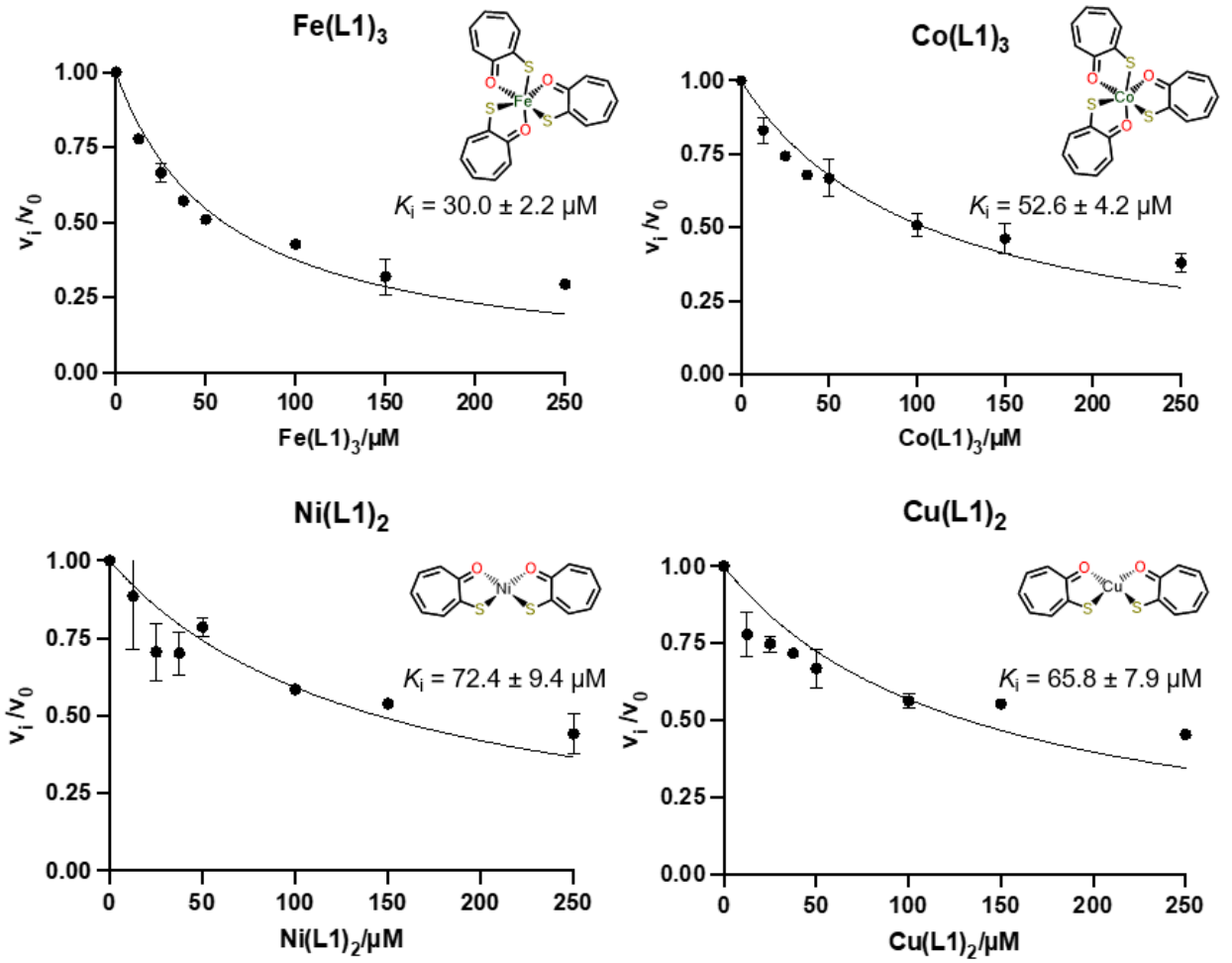

Figure 4.7: Concentration vs. velocity plots used to calculate K_i for Fe(**L1**)$_3$, Co(**L1**)$_3$, Ni(**L1**)$_2$, and Cu(**L1**)$_2$. Molecular structures represented as ChemDraws for clarity.

to Zn, at least in these *in vitro* assay conditions.

Since each of the DNICs were found *in silico* to position the DNIU favorably for coordinative inhibition of Cys145 via computional modelling using Autodock4,[122] TG-RRE and TGTA-RRE were tested *in vitro* to see if the possibility of inhibition is experimentally confirmed. The K_i's were experimentally determined for the free ligands TG and TGTA, $Fe^{III}Cl_3$, $NaNO_2^-$ (the NO control used for this experiment), and the dimeric TG-RRE and TGTA-RRE. The aforementioned FRET protease assay determined that TGTA-RRE and TG-RRE inhibited $SC2M^{pro}$ with an K_i of 32.9 and 28.2 μM respectively (**Figure 4.8**). These values are about an order of magnitude less than $FeCl_3$,

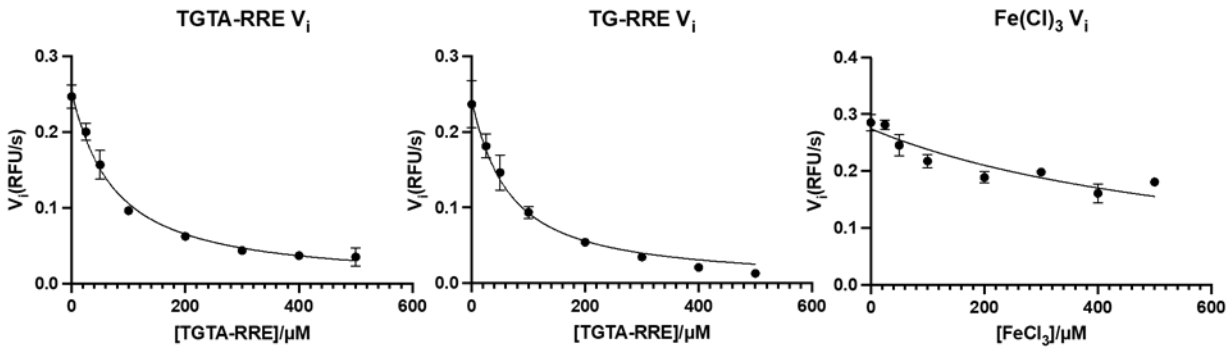

Figure 4.8: Concentration vs. velocity plots used to calculate K_i for TGTA-RRE [Left], TG-RRE [Middle], and $FeCl_3$ [Right].

(322.5 μM), a control for solvated Fe^{III}, a DNIC decomposition product in aqueous media. The free ligands and nitrite did not inhibit the enzyme even at mM concentrations. This indicates that the inhibition comes from the dinitrosyl iron unit, and not the thiolate, iron, or NO since the K_i's of the decomposition products are at least an order of magnitude higher than the DNIC's tested. The inactivity of the ligand is consistent with the computational data which suggests that the free ligands are poorer inhibitors than the monomeric or dimeric forms of the DNIC.

4.2.4 Native Mass Spectrometry

Native Mass Spectrometry (Native MS) is a technique derived from the well known electrospray ionization mass spectrometry (ESI-MS). It has been utilized to observe non-covalent interactions,[179] often between two proteins or between a ligand and a protein. As such, it serves as a means to observe potential Zn(**L**)-$SC2M^{pro}$ adducts which have previously eluded detection by standard ESI. The major peak associated with Apo $SC2M^{pro}$ is that of the active dimeric species at 67593 daltons (Da) **Figure 4.9**. This mass is represented as the blue cirlces, and is the major species in the green spectra, collected in the absence of Zn(**L1**)$_2$. However when $SC2M^{pro}$ is reacted with the Zn(**L**)$_2$ complexes prior to ionization, the highest abundance peak shifts from that of the monomer. Mass shifts of + 63 Da, assigned to Zn^{II} binding, are shown as orange triangles. Mass shifts of +200 Da, assigned to $[Zn(\mathbf{L1})]^+$, are represented as red squares. The highest relative abundance is the +200 Da species, pointing to the formation of a Zn(**L**)-$SC2M^{pro}$ adduct.

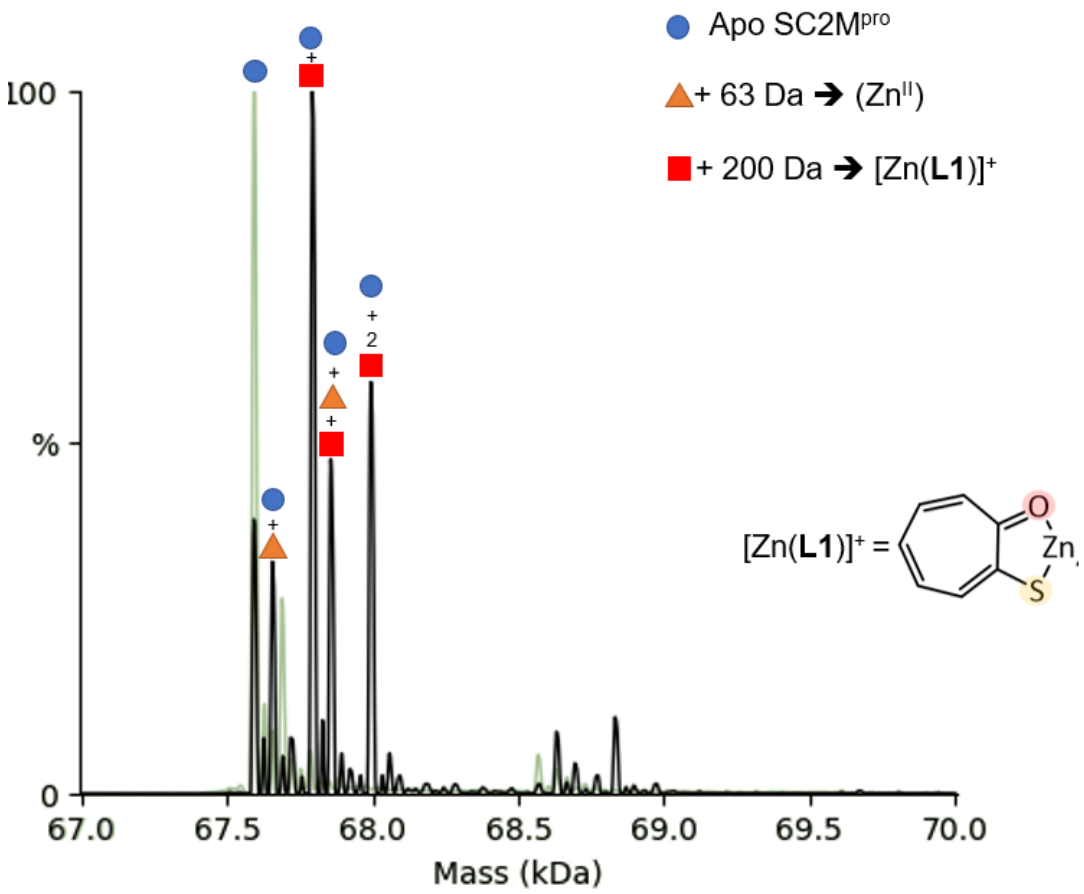

Figure 4.9: Deconvoluted spectrum of SC2M^{pro} and its reaction products with Zn(**L1**)$_2$. The green spectra was collected in the absence of Zn(**L1**)$_2$ aka Apo-SC2M^{pro} while the black spectra is that of the reaction products of SC2M^{pro} and Zn(**L1**)$_2$.The blue circles represent the mass of the SC2M^{pro} dimer with potential Zn^{II} (orange triangles) and [Zn(**L1**)]$^+$ (red squares) adducts indicated.

A potential structure of this adduct can be visualized as a cartoon in **Figure 4.9**. These results indicate that ligand loss from Zn(**L**)$_2$ is generating a species that can associate with SC2M^{pro}, potentially at the catalytic dyad as has been observed crystallographically for other Zn-complexes that inhibit the closely related SC1M^{pro}.[117] Similar behavior, with mass shifts of +242 Da and +243 Da for are observed for the reaction of Zn(**L2**)$_2$ (Figure B.17) and Zn(**L3**)$_2$ (Figure B.18) with SC2M$_{pro}$ respectively.These results also indicate that there are likely 2 Zn-binding sites available on SC2M^{pro}.

Interestingly, although it is a relatively potent inhibitor, Zn(PT)$_2$ does not appear to form a

discernible Zn(PT)-containing adduct with SC2M^{pro} (**Figure B.16**). Likewise, although the DNICs displayed moderate efficacy against SC2M^{pro} *in vitro*, the native MS indicated they did not appear to be forming easily assigned adducts with the protease, nor do they appear to be nitrosylating SC2M^{pro} (**Figure B.19** and **B.20**). The mechanism by which these compounds may be acting against the protease awaits further investigation.

4.3 Conclusion

While previous reports have indicated other first row transition metal complexes containing Co or Cu could be effective at inhibiting SC2M^{pro},[140, 141, 139] this effect was not observed for the compounds tested above. Taken together, it appears as though Zn^{2+} is unique among the metals tested for inhibition of SC2M^{pro} *in vitro*. It should be noted however, that Cu gluconate has displayed moderate efficacy against SC2M^{pro} in Vero E6 cells infected with SC2. $Cu(HK)_2$ has proven effective against human influenza virus as described in Chapter I. Therefore, the activity of these complexes *in vivo* is still of interest despite their poor performance against SC2M^{pro} *in vitro* as they may impact other viral pathways not related to polyprotein processing.

When examining the effect of coordination mode on inhibitory efficacy, going from O4 to S2O2 led to a marked increase **Figure 4.6**. Neither $Zn(trop)_2$ nor $Zn(HK)_2$ offered an enhancement relative to $ZnCl_2$ alone while Zn(**L4**)$_2$ was actually less effective than $ZnCl_2$. However, for the S2O2 derivatives, an up to 5-fold increase in inhibition is observed for the Zn(**L**)$_2$ complexes, with Zn(**L1**)$_2$ performing the best while Zn(**L2**)$_2$ and Zn(**L3**)$_2$ offer similar performance to $Zn(PT)_2$, a well-known medicinal Zn^{II} compound with a dianionic S2O2 coordination mode.[109] With three major viral proteins, RNA dependent RNA polymerase (RdRp),[108] the papain-like protease (PL^{pro}),[112] and M^{pro} all showing susceptibility to Zn coordination complexes, Zn is well positioned to contribute to the ongoing battle against SC2. This broad range of potential targets coupled with the lipophilicity observed in the previous report on Zn(**L1**)$_2$,[2] lead to a reasonable hypothesis that the activity of these complexes, particularly Zn(**L1**)$_2$, stand to be magnified *in vivo*.

5. SOLUTION-PHASE PROPERTIES OF A SOLID-PHASE TETRAMERIC NICKEL COMPLEX[1]

5.1 Introduction

Protein	**Function**	**Primary Coordination Sphere**
Acetyl-CoA Synthase	Acetyl-CoA production	Ni_d: 2 amides, 2 μ-Cys-S Ni_p: NiN_2S_2, 1 μ-Cys-S
Ni-Carbon Monoxide Dehydrogenase	CO Oxidation	2 μ-sulfides, terminal Cys-S, μ-OH
Ni-Fe Hydrogenase	H^+ reduction & H_2 oxidation	2 Cys-S, 2 μ-Cys-S
Methyl-Coenzyme M Reductase	Methane production	Tetrapyrollic corphinoid (N_4)
Aireductione Dioxygenase	Dioxygenation	3 His-N, 1 Glu-O_2, 2 H_2O
Glyoxalase 1	Aldehyde detoxification	2 His-N, 2 Glu-O_2
Ni-Superoxide Dismutase	Superoxide detoxification	
Urease	Urea hydrolysis	Ni_1: 2 H_2O 2 His-N, Ni_2: 2 H_2O 2 His-N, 1 Asp-O_2
Lactate Racemase	Lactate racemization	1 His-N, NAD SCS pincer
Ni-depedent Repressor	Nickel homeostasis	3 His-N, 1 Cys-S

Table 5.1: Table highlighting Nickel-containing proteins, their functions, and the primary coordination sphere surrounding Nickel.

While zinc is extremely common in the proteome, nickel is utilized much more sparingly in natural systems. As discussed briefly in the introduction, there are nine known nickel metalloenzymes, which are displayed alongside a tenth nickel-containing regulatory protein, Nickel-responsive repressor (NikR) in **Table 5.1**. NikR is included in the table due to importance in regulating cellular Ni efflux.[180, 181, 182, 183]. The functions of these nine varies wildly, from sugar isomerism in Lactate racemase to the C-C bond formation found in Acetyl-CoA synthase.

[1]Reprinted with permission from "Self-Assembled Nickel-4 Supramolecular Squares and Assays for HER Electrocatalysis Derived Therefrom" by Xuemei Yang, Christopher R. DeLaney, Kyle T. Burns, Lindy C. Elrod, Wenting Mo, Haley Naumann, Nattamai Bhuvanesh, Michael B. Hall, and Marcetta Y. Darensbourg, 2021. Inorganic Chemistry,60, 10, 7051–7061, Copyright 2021 by American Chemical Society.

The identity, function, and primary coordination spheres of each of these nickel-containing proteins is displayed in **Table 5.1**.[18, 17] The Ni-binding sites of a selection of proteins that contain thiolates can be found in **Figure 5.1**. Our lab and many others have long sought to mimic these active/metal-binding sites using metallothiolates as building blocks to assemble bimetallic or multimetallic molecules.[184, 185, 186, 14]

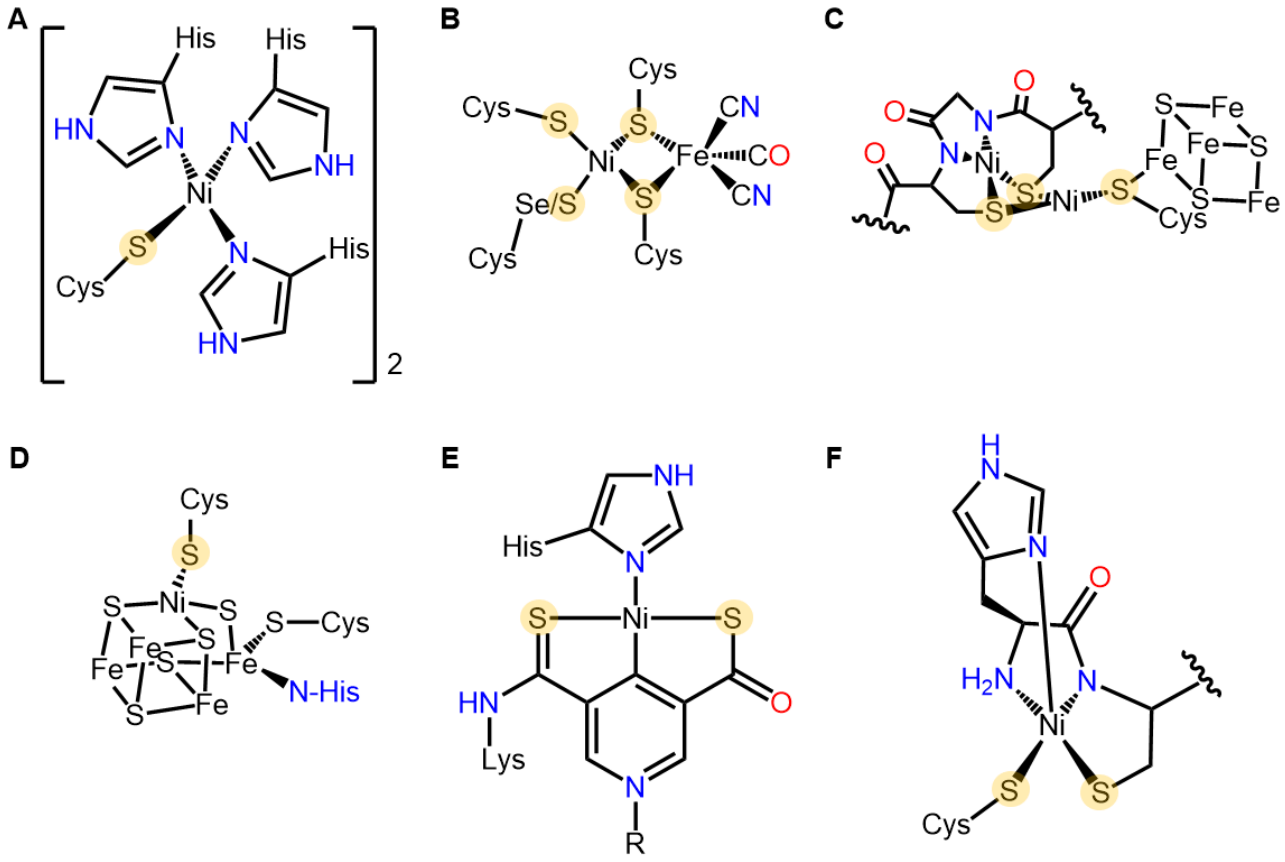

Figure 5.1: ChemDraw representations of Ni-containing proteins (**A**) Ni-responsive Repressor (**B**) Ni-Fe Hydrogenase, (**C**) Acetyl-CoA Synthase, (**D**) Ni-Carbon Monoxide Dehydrogenase (**E**) Lactate Racemase, and (**F**) Ni-Superoxide Dismutase that possess thiolates in the primary coordination sphere.

Small molecule models of metal-binding sites have been invaluable in building understanding of the roles of metals within biology.[187, 188] These well-characterized and readily modifiable synthetic analogues of metal binding sites lend themselves to study by a gamut of physical meth-

ods that are often difficult to carry out on the natural system. A synthetic approach to generate biomimetic Ni coordination complexes of varying primary coordination sphere involves the splitting of dimeric $[NiN_2S]_2^{2+}$, with exogenous nucleophiles.[124] Jenkins *et al.* first reported this methodology to mimic the N_3S metal binding pocket found in NikR.[180, 182] By varying the nature of the imidazole derivative used to split the $[NiN_2S]_2^{2+}$, a number of $[NiN_2SN']^+$ species were synthesized and characterized, as represented in **Figure 5.2**. In a follow-up report, the variety of nucleophiles used to split this dimer was expanded to include pyridine, carbenes, and aryl-thiolates (AR-S).[189]

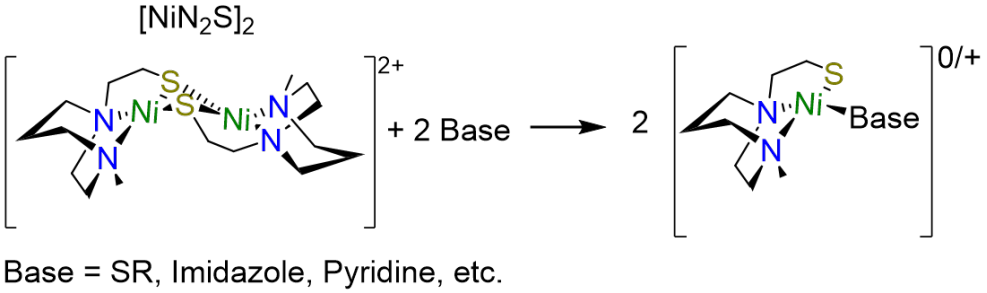

Figure 5.2: ChemDraw representation of $[NiN_2S]_2^{2+}$ dimer splitting reaction first reported in ref. 124.

Building on this work, Yang and coworkers used Ar-S and aryl-selenides (Ar-Se) nucleophiles to synthesized minimal models of the bimetallic [NiFe]- and [NiFeSe]-hydrogenase enzymes.[190] These complexes were found to undergo oxygenation reactions with O_2 reacting at the Ar-S or Ar-Se chalcogen to form adducts that bear a striking resemblance to the oxygenated states of [NiFe]- and [NiFeSe]-hydrogenase enzymes.[191, 192, 193] The reversibility of these oxygenation reactions in such mimics aligned well with what had been observed in the native enzymes,[194] with the sulfur-containing [NiFe] models being more difficult to "reactivate" than the selenium-containing [NiFeSe] models.[195]

The studies described above by Yang *et al.* are not the first time our lab has taken an interest in S-modification of metal complexes. The M.Y. Darensbourg lab has long had an interest in the

oxygen uptake reactivity of monomeric metallothiolates. An early report by Farmer *et al.* in 1992 detailed isotopic labelling studies on the O_2 uptake products of NiN_2S_2 complexes. It was shown that multiple oxidation levels of the NiN_2S_2 and complexes ($NiN_2S(SO_2)$ and $NiN_2(SO_2)_2$) were present when reacted with O_2 for 24 hours.[196] An Accounts article published in 1998 by Grapperhaus and Darensbourg discussed potential mechanisms of these oxygenation reactions and their impact on the electronic properties of the resulting metal complexes.[197] Oxygenation isn't the only means of altering thiol donor ability however. As noted in Chapter I, other types of modification have been shown to modulate the properties of thiolate-containing metal complexes.[13, 5, 14] Acetylation of the N_2S_2 tetra-dentate ligand generates the $N_2S'_2O_2$ hexadentate ligand. This ligand was found to undergo metal exchange when the zinc complex of $[ZnN_2S'_2O_2]$ is reacted with Nickel salts as seen in a 2009 study by Almaraz *et al.*[198] Further studies on these complexes showed that the ease of displacement of first-row transition metals (Fe-Zn) from this hexadentate chelating ligand followed exactly with what is predicted by the Irving-Williams series, i.e. the stability of the M^{II} complexes are ($Fe^{II}<Co^{II}<Ni^{II}<Cu^{II}>Zn^{II}$).[199]

While more commonly used for organic species, there are examples of DOSY being applied to metal complexes. For example, Chan et al. used DOSY to investigate the nuclearity of a number of Ru and Fe containing macrocycles in 2011 with computationally determined volumes aligning well with those determined experimentally.[200] Bonakdarzadeh *et al.* used DOSY to investigate a number of Pt-containing and Pd-containing supramolecular assemblies to determine the structural effects of electron-donating and electron-withdrawing groups on the backbone.[201] Fiedler *et al.* applied DOSY to gyroscope-like organometallic moieties that are known to form different isomers upon C-C bond metathesis in an attempt to distinguish between them in solution.[129] Although each of these studies have shown the applicability of these techniques, none to our knowledge have directly addressed the structural information that can be gleaned by each technique across a series of related compounds. Using these small molecule biomimetics with readily modifiable primary coordination spheres, we aimed to address this and show that each of these techniques offer unique structural information.

Given the interesting properties elicited upon acetylation of the N_2S_2 ligand, an analogous synthesis targetting the acetylated N_2S ligand was devised. The work herein highlights my contributions to the determination of the oligomeric state of S-acetylated NiN_2S complexes $[NiN_2S'O]_n^{0/n+}$, which were found to be precatalyts for hydrogen production.[3] While the complex exists in the solid-state as a tetramer, in solution it was found to be a monomer. Using various forms of spectroscopy, most notably ^{1}H Diffusion Ordered Spectroscopy (DOSY) NMR, the properties of the Ni-complex in the solid-state and solution-phase were investigated.

5.2 Results

5.2.1 Synthesis

Reaction of $NiN_2S{\cdot}EPh$ with sodium iodoacetate **Figure 5.3** (a) led to acetylation of both E and S, expulsion of the acetylated EPh^- ligand, and expansion of tridentate N_2S ligand to tetradentate $N_2S'O$, as the acetylated S within the N_2S tridentate ligand converts into a nickel-bound thioether, S′. The exclusive formation of the iodo-derivative of the carboxylate-bridged molecular square was monitored by color changes from dark purple (E = S) or dark brown (E = Se) to the sea green/blue color representing $[\mathbf{Ni\text{-}I}]^0$, characterized in the solid state to be a neutral tetramer $[\mathbf{Ni\text{-}I}]_4^0$. The $[\mathbf{Ni\text{-}I}]_4^0$ is air stable and soluble in water and polar organic solvents. The same product was obtained via direct addition of iodoacetate to the $[NiN_2S]_2^{2+}$ dimer, route (b), as well as the reaction of the dimer with preformed, acetylated EPh^-, route (c). Route (d) represents the conversion of the N_2SH ligand to the unbound $N_2S'O$ ligand by acetylation prior to introducing nickel. That is, nickel templating of the N_2S^ligand is not required prior to S-acetylation; the free $N_2S'O$ tetradentate ligand readily wraps up the nickel ion, engaging the four possible binding donors.

5.2.2 Solution Characterization

Although crystalline products of acetylated $[NiN_2S]_2^{2+}$ were isolated and structurally characterized as tetramers, there is convincing evidence that smaller aggregates, likely solvated monomeric forms, prevail in solution **Figure 5.4** (a). **Figures 5.4** (c) and (d) display the UV-vis spectra of complexes $[\mathbf{Ni\text{-}I}]^0$ and $[\mathbf{Ni\text{-}Solv}]^+$. In DCM, $[\mathbf{Ni\text{-}I}]^0$ has absorptions at 360 and 428 nm, consistent

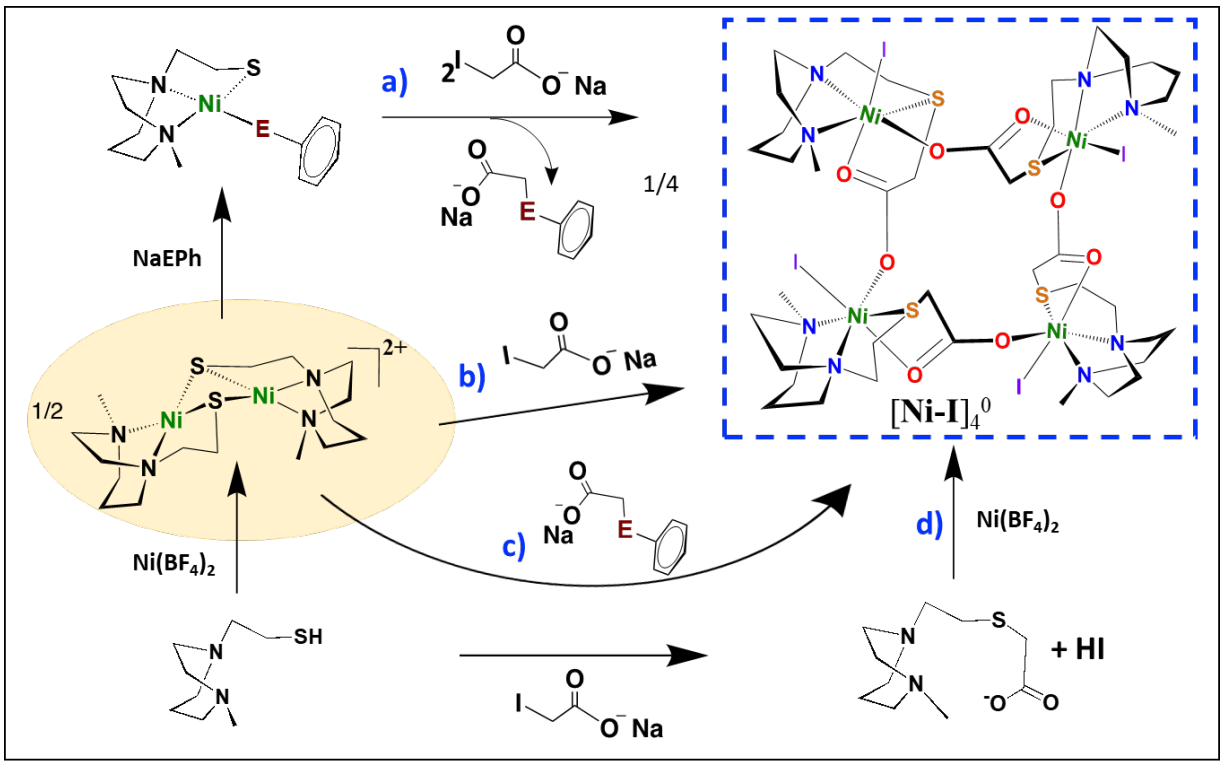

Figure 5.3: Synthetic routes to [**Ni-I**]$_4^0$, a) by sulfur acetylation of [NiN$_2$S·EPh], E = S (dark purple) or Se (dark brown) with yields of 61- 65%; b) from dimer (maroon) splitting with sodium iodoacetate giving a yield of 87%; c) from dimer splitting with NaE′Ph (55% and 40% yields for E′ = S and Se); and d) by direct synthesis from pre-formed N$_2$S′O ligand and the nickel salt with yield of 40%. Mixtures of MeCN and MeOH were used as solvent.

with the visual observation of a greenish-blue color. In MeOH or H_2O solution, [**Ni-I**]^0 is distinctly blue, in agreement with λ_{max} values of 378 and 600 nm. Note that the bis-acetylated NiN$_2$S$_2$ complex, the octahedral NiN$_2$S′$_2$O$_2$ whose structure is shown in **Figure 5.4** (b) is cobalt-blue in the solid state and also in aqueous solution.[199] The solid-state UV-Vis spectra of NiN$_2$S′$_2$O$_2$ and [**Ni-I**]$_4^0$ complex are given in **Figure C.14** and are qualitatively similar as expected for the similar first coordination spheres around the Ni^{II}. The solid-state ATR-IR of these two species (**Figure C.13**) both show ν(C=O) stretches at 1587 cm^{-1}. The ν(C=O) IR values for NiN$_2$S′$_2$O$_2$ are blue shifted relative to the solid-phase, and vary over ca. 30 cm^{-1} in MeOH, DCM and MeCN (**Figure C.12**). Similarly, the solution phase IR of [**Ni-I**]$_4^0$ is blue-shifted 15-50 cm^{-1} depending on solvent.

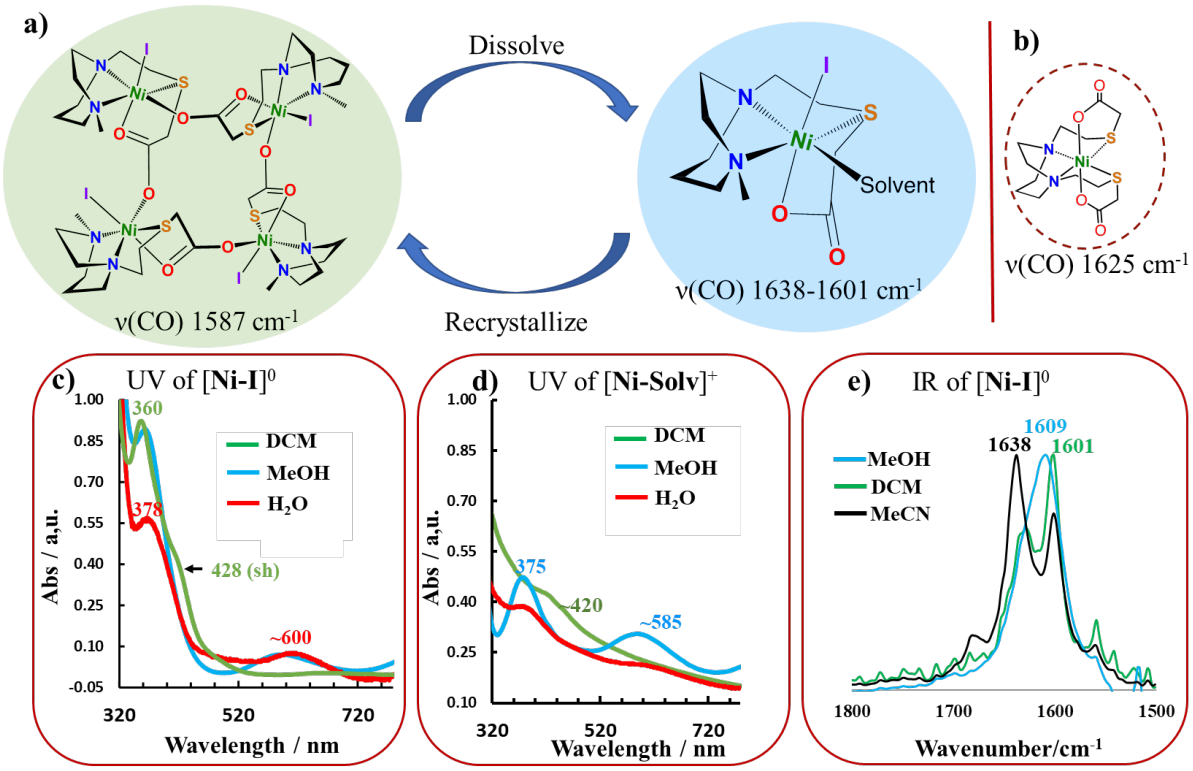

Figure 5.4: (a) The two forms of the nickel complex: tetramer in solid state and presumed monomer in solution; (b) $NiN_2S'_2O_2$ complex with ν(C=O) value recorded in DCM from ref. 197. The UV-Vis spectra of complexes (c) [**Ni-I**]^0 and (d) [**Ni-Solv**]$^+$ in various solvents; (e) displays of the IR spectra in the ν(C=O), 1600 cm^{-1} range of [**Ni-I**]^0 in MeOH, and in DCM and MeCN solutions.

Two ν(C=O) bands are observed for DCM (1628, 1601cm^{-1}) and MeCN (1638, 1601 cm^{-1}) while a single band is observed in MeOH (1609 cm^{-1}) **Figure 5.4** (e). The higher wavenumber value is consistent with that attributed to the unbound carboxylate oxygen in the $NiN_2S'_2O_2$ complex, **Figure 5.4** (b), and hence implies that a structure with unbound C=O within the ligated carboxylate exists in the polar solvents. It should be noted that a potential dimeric configuration might also have such a non-bridging carboxylate, analogous to the dicopper species where the ν(C=O) band in the copper dimer is positioned at 1631 cm^{-1}.[199] Similar phenomena were observed in the IR spectra of complex [**Ni-Solv**]$^+$ (**Figure C.12**).

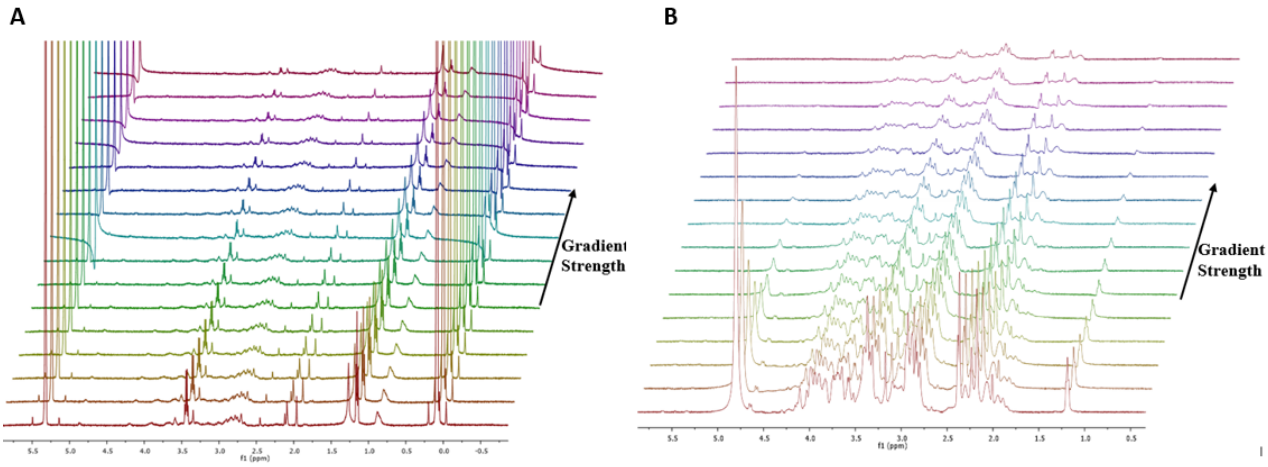

Figure 5.5: ^{1}H DOSY NMR of [**Ni-I**]^{0} in (A) CD_2Cl_2 and (B) D_2O under increasing gradient strength.

5.2.3 NMR Studies

To gain information regarding the state of aggregation of [**Ni-I**]^{0} in solution, ^{1}H DOSY NMR experiments were undertaken, ultimately yielding an estimate of the hydrodynamic radius (r_H) of [**Ni-I**]^{0} in solution in the two solvents D_2O and CD_2Cl_2 compared for this study. The DOSY NMR technique can be used to interrogate the rate of diffusion of solution-phase species, obtaining diffusional coeffcients (D) in the process. These D-values are related to the effective size of a molecule in solution and can be used to determine its molecular weight and r_H. Phenomena such as hydrogen bonding, ion-pairing, and encapsulation are all measurable using DOSY.[202] DOSY is a non-destructive, solution-phase technique that provides structural information without necessitating the growth of crystals. Although most applications of DOSY are focused on supramolecular assemblies, its use in structural determinations of molecular complexes is a growing area of research, and it provides an excellent avenue for exploring structures of inorganic complexes in solution.

The ^{1}H DOSY spectra for [**Ni-I**]^{0}], seen in **Figure 5.5**, indicate similar diffusion rates in both solvents with a slightly slower rate in D_2O (**B**) relative to CD_2Cl_2 (**A**). These plots yield experimentally derived, hydrodynamic radii from ^{1}H DOSY NMR of ca. 4.2 Å (D_2O) and 3.4 Å (CD_2Cl_2)

are both significantly smaller than the solid state tetrameric $[\mathbf{Ni\text{-}I}]_4^0$ radius of ca. 6.1 Å, with values closer to the estimate of 3.9 Å from a monomer derived from solid state/crystal structure estimate as compared in **Figure 5.6**. We conclude that the compound is in a monomeric state in both solvents. We further posit that the larger value in D_2O indicates stronger interactions with the solvent and potentially higher coordination number relative to that observed in CD_2Cl_2. This could account for the increase in the observed hydrodynamic radius. The results of these studies are summarized in **Table F.7**.

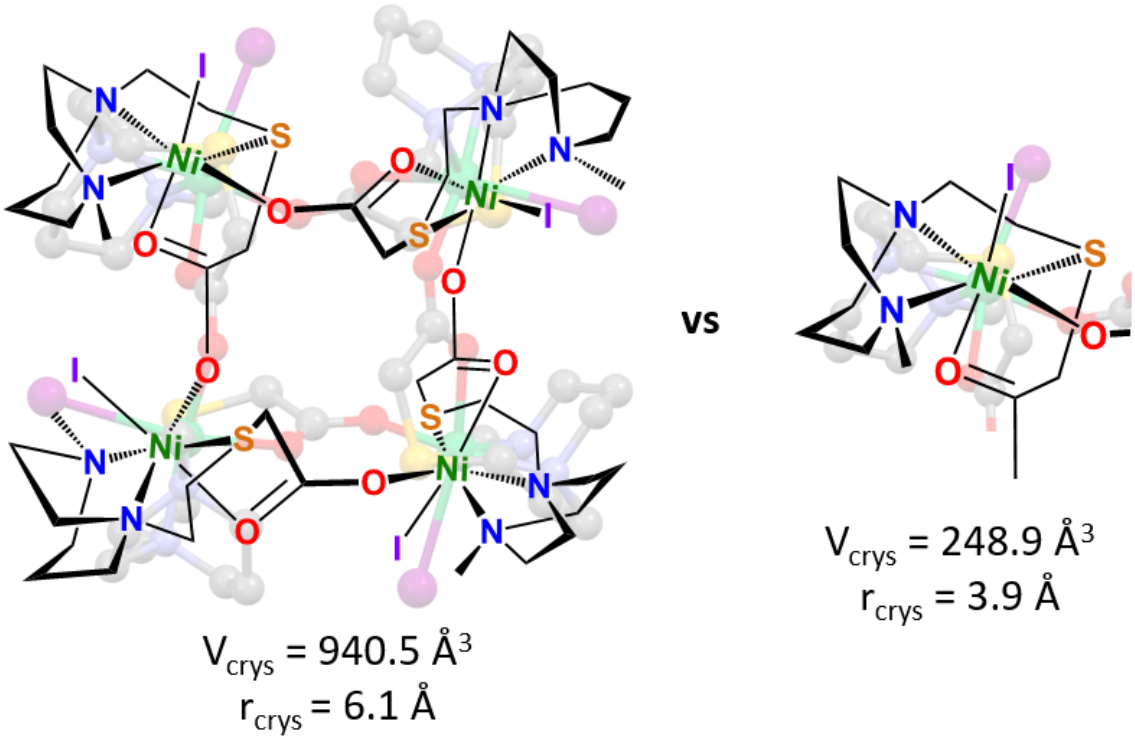

Figure 5.6: Crystallographic volume (r_{crys}) of $[\mathbf{Ni\text{-}I}]^0$ as a tetramer and monomer derived from OLEX.

The interpretation of solution properties described above is supported by the fact that the compound is diamagnetic in CD_2Cl_2, consistent with an assignment of d^8 Ni^{II} in a square planar geometry, and further consistent with the DFT results. In contrast the D_2O sample shows ^{1}H-NMR

signals in the paramagnetic region, indicating that water is most likely occupying the open sites, generating a penta/hexa-coordination sphere and a high spin Ni^{II}. This would also account for the difference in color between the CD_2Cl_2 solution (green) and the D_2O solution (blue). Notably, the Evans Method derived magnetism for [**Ni-I**]^0 and [**Ni-Solv**]$^+$ in D_2O was determined to be 2.41 μBM and 2.5 μBM, respectively, **Figures A.10**-**Figures A.11**. The applicability of this technique to paramagnetic species depends on whether the paramagnetic relaxation pathway is much slower than relaxation via diffusion. Although ^{1}H DOSY NMR is not commonly applied to paramagnetic compounds for this reason, there are examples of such experiments yielding insights into oligomeric state of metal complexes, such as work performed on Fe complexes by Crockett *et al.* in 2019.[203]

5.3 Conclusion

The salient conclusions from these studies are as follows:

- Exposure of a S-bridged $[NiN_2S]_2^{2+}$ synthon to sources of iodoacetate generate S-acetylation and thermodynamically-driven, self-assembled clusters.

- The clusters crystallize as molecular squares, in which each of the four nickels are in octahedral coordination and the original N_2S donors retain meridional positions: the S connected into the N_2S, is modified by the acetylation agent into an S-bound thioether. Two carboxylate oxygens, one internal and one bridging from an adjacent nickel add to the coordination sphere, while either iodide or acetonitrile/water completes the hexa-coordination. There was no indication that such tetrameric structures were retained in solution.

- Solution characterization indicates solvent dependence for IR and electronic spectral properties, as well as the observed hydrodynamic radius of the complex from the ^{1}H DOSY NMR measurements. DOSY in particular points to a monomeric formulation in solution, as the observed (r_H) values in CD_2Cl_2 (3.4 Å) and D_2O (4.2 Å) align more closely with the estimated radius of a monomeric unit in the crystal structure (ca. 3.9 Å), rather than the tetramer (radius ca. 6.1 Å). Para- or diamagnetism of [**Ni-I**]^0 varies with solvent.

These studies point to the importance of selecting the right technique when comparing solution-phase properties and solid phase structures, and demonstrate the utility of ^{1}H DOSY NMR for investigating inorganic complexes. The ability to identify the oligomeric state of such complexes of solution is also of import due to their ability to act as precatalysts for HER.

6. SUMMARY AND PERSPECTIVE

6.1 Summary

The work presented in this dissertation highlights the utility of thiolates in the construction of metal complexes of varying applications. Chapter I provides a general background on thiolate chemistry before focusing largely on the medicinal applications of tropolones, specifically as it relates to viral inhibition and SARS-CoV-2. Chapter II gives the experimental details of the work conducted during my studies. Chapters III demonstrates how using thiolates to tune the primary coordination sphere provided by tropolones, generating SO ligands, can be used to generate effective Zn-based inhibitors of the SARS-CoV-2 main protease SC2M^{pro}. Chapter IV expands on this idea, investigating the effects of changing the coordinated metal as well as further modifying the primary coordination sphere by adding an additional thiolate, giving an S2 ligand, on the inhibition of SC2M^{pro}. Finally, Chapter V examines how S-acetylation in Ni-S complexes can impact the solid-state structures and solution-phase properties of the resulting complexes.

6.1.1 Zinc thiotropolone combinations as inhibitors of the SARS-CoV-2 main protease

Chapter III focuses on our initial investigations into the inhibition of SC2M^{pro} using Zn-based inhibitors. It was found that substituting one of the oxygen donors of tropolones with a thiolate, generating SO ligands, resulted in a more potent inhibitory combination for the simplest thiotropolone **L1**. When compared to $Zn(NO_3)_2$ alone or the parent coordination complexes $Zn(trop)_2$, and $Zn(HK)_2$, Zn-**L1** combinations proved the most effective *in vitro* inhibitors of SC2M^{pro}. This was observed regardless of whether Zn^{II} and **L1** were administered as a complex [Zn(**L1**)$_2$] or as separate components i.e. $Zn(NO_3)_2$ + **L1**. This inhibition is dependent on the ratio of $Zn(NO_3)_2$ to **L1**, with excess **L1** resulting in a return of SC2M^{pro} activity. The proposed mode of inhibition is via displacement of one **L1** from [Zn(**L1**)$_2$], resulting in a [Zn(**L1**)$^+$] metallofragment. This hypothesis is based on both chemical reactivity of the intact complex with biological bases and computational modelling of SC2M^{pro}'s interactions with **L1** [Zn(**L1**)$^+$], and [Zn(**L1**)$_2$].

6.1.2 Effect of Metal Identity and Coordination Sphere on Metal-based SC2M^{pro} Inhibition

Chapter IV expands on the initial studies of SC2M^{pro}, although using a different assay as described in Chapter II. Transition metal complexes (Fe-Cu) of **L1** were synthesized, characterized, then tested for inhibitory activity. Despite some reports touting the potential efficacy of cobalt and copper,[139, 140, 141] none of the other first-row transition metals, as either MCl_x salts or M**L1**)$_x$ complexes, were effective at inhibiting SC2M^{pro} *in vitro*. Whether these complexes may target a different viral protein or critical cellular pathway remains to be seen however. The effect of varying coordination sphere on Zn-based inhibition was also investigated. It was determined that just as in the previous study, **L1** was the most effective at enhancing inhibition. Neither the 2O trop and HK, nor the 2S **L4** provided the same boost in efficacy observed for **L1**. Zn(**L1**)$_2$ even outperformed the known medicinal Zn(PT)$_2$. Native MS studies indicate the formation of a Zn(**L1**)-SC2M^{pro} adduct as a potential means to explaining the observed inhibitory activity of the Zn(**L**)$_2$ complexes. Finally, studies of another class of metal-based inhibitors, Dinitrosyl Iron Complexes (DNICs), showed modest inhibition of SC2M^{pro}. Given that Native MS studies did not show a discernible adduct forming between the DNIC and SC2M^{pro}, the mechanism by which this inhibition occurs remains to be determined.

6.1.3 Solution-phase Properties of a Solid-phase Tetrameric Nickel Complex

Chapter V details our investigations into a nickel complex that was found to make "molecular squares" in the solid-phase. While the crystal structures resulting from the two [NiN_2S′O] complexes ([**Ni-I**]$_4^0$ and [**Ni-solv**]$_4^{4+}$) were found to be tetrameric, solution phase measurements pointed to a monomeric solution-phase formulation of [**Ni-I**]^0 and [**Ni-solv**]$^+$. The Evans method NMR, used for determing the magnetic moment of [**Ni-I**]^0 and [**Ni-solv**]$^+$, shows paramagnetism in D_2O for both complexes while no paramagnetic signals are observed in the analogous spectra in CD_2Cl_2 of [**Ni-I**]^0. In addition, while the crystallographic radius (r_{crys}) of the tetrameric [**Ni-I**]$_4^0$ was found to be 6.1 Å, ^{1}H DOSY NMR in CD_2Cl_2 and D_2O gave hydrodynamic radii (r_H) of 3.35 Å and 4.20 Å respectively. These values align much more closely with the r_{crys} of a monomeric

unit derived from the crystal structure, i.e. a radius of ca. 3.9 Å. Coupled with the shifts in the UV-Vis/IR when going from the solid-state to the solution-phase, we concluded that the tetramer does not persist in solution, and likely breaks up into monomers with coordinating solvents occupying the available site on Ni^{II}. When dissolved in solution these complexes were found to be a precursors for electrocatalysis, producing H_2 in the presence of acetic acid.

6.2 Perspective

The work described in Chapters III and IV expands on previous studies of metal-tropolone combinations as potential therapeutics.[46, 68, 69, 70, 71, 86, 87, 88, 89, 96, 97] While a number of Medical Hypotheses papers pointed to the potential of Zn in combination with hinokitiol,[148] chloroquine,[120, 164] and other ionophores, there have been few thorough studies on the topic.[159] Medicine is dominated by organic molecules, but that need not be the case. A recent review by Cohen *et al*. highlights the potential of metal complexes in this regard and their relative under utilization when compared to more traditional organic moieties.[163]

6.2.1 New metal-thiotropolone complexes

Copper-tropolone complexes to this point have the greatest breadth of medicinal applications. Despite their lack of efficacy in the *in vitro* studies against $SC2M^{pro}$ in Chapter IV, they remain an excellent candidate for further research. This is particularly true in the area of anti-metastatic compounds, where both $Cu(trop)_2$ and $Cu(HK)_2$ have already seen success.[87, 88] Given that coordination sphere had such a profound impact on the efficacy of our Zn-thiotropolone complexes, it would be intriguing to see how such changes would impact the biological activity of Cu^{II} complexes. Another interesting application of the thiolated tropolones described here may be their use in place of 1-thio-β-d-glucose tetraacetate (TGTA) in Auranofin, depicted in **Figure 4.1 A**. Substitution of TGTA with **L1-L4** may lead to new therapeutic compounds with increased lipophilicity. A crystal structure of a Au-PPh_3(**L1**) complex, shown in **Figure D.X** was determined during my studies, and provides a proof of concept for generating other $AuPR_3$-thiotropolone complexes. Changing the ligands surrounding gold has been shown to alter the activity of gold-based

therapeutics,[204] and offers an avenue for further exploration. Other donor atoms such as N or P would offer further variety in terms of ligand affinity and could provide another avenue for tuning metal-ligand interactions. The most important area for further investigation however would be test these compounds on infected cells. Given that Zn^{II}-ionophore complexes are known to inhibit viral replication in infected cells,[89, 108, 110, 111] *in vivo* testing is the next logical step in determining the applicability of these complexes as prophylactics or therapeutics.

6.2.2 Increased utilization of DOSY and Ion Mobility Mass Spectrometry

While the molecular structures as determined by XRD remain invaluable to inorganic chemistry, they can at times be misleading as to the nature of the species that are present in solution. The Ni^{II} complexes in Chapter V are an excellent example of this. While the complexes are tetramers with bridging carboxylates in the solid-state, their solution-phase properties as determined by DOSY NMR among other techniques indicate a monomeric formation is more likely. Applying techniques such as DOSY to solution-phase structural questions (when applicable) is a more direct means of addressing them than extending conclusions based on the solid-phase.

Ion mobility mass spectrometry (IM-MS) is another emerging technique that could have great utility in inorganic structural determinations. IM-MS couples two analytical techniques, ion mobility (IM) and mass spectrometry (MS), facilitating the analysis of ions in the gas phase. Ion mobility provides information about the shape and size of analytes while mass spectrometry allows for the determination of gas-phase mass-to-charge (m/z) ratios. By combining these two orthogonal separations, ions can be separated initially by their size in IM and identified by their respective (m/z). This technique has also been applied to small molecules that can exist as different conformers. Baker et al. showed that it was possible to separate isomeric inorganic complexes and that the determined CCS values aligned well with computationally-derived structures.[205] As ionization methods become more "gentle" increasing amounts of solution-phase information can be maintained, just as is seen in the Native MS studies in Chapter IV. Both of these techniques offer an alternative or partner to crystallography in drawing conclusions about the nature of inorganic species in solution.

REFERENCES

[1] J. F.-W. Chan, S. Yuan, K.-H. Kok, K. K.-W. To, H. Chu, J. Yang, F. Xing, J. Liu, C. C.-Y. Yip, R. W.-S. Poon, H.-W. Tsoi, S. K.-F. Lo, K.-H. Chan, V. K.-M. Poon, W.-M. Chan, J. D. Ip, J.-P. Cai, V. C.-C. Cheng, H. Chen, C. K.-M. Hui, and K.-Y. Yuen, "A familial cluster of pneumonia associated with the 2019 novel coronavirus indicating person-to-person transmission: a study of a family cluster," *The Lancet*, vol. 395, no. 10223, pp. 514–523, 2020.

[2] C. R. DeLaney, Y. Sheng, D. C. Pectol, E. Vantansever, H. Zhang, N. Bhuvanesh, I. Salas, C. Fierke, W. Liu, and M. Y. Darensbourg, "Zinc thiotropolone combinations as inhibitors of the sars-cov-2 main protease," *Dalton Transactions*, 2021.

[3] X. Yang, C. R. DeLaney, K. T. Burns, L. C. Elrod, W. Mo, H. Naumann, N. Bhuvanesh, M. B. Hall, and M. Y. Darensbourg, "Self-assembled nickel-4 supramolecular squares and assays for her electrocatalysts derived therefrom," *Inorganic Chemistry*, vol. 60, no. 10, pp. 7051–7061, 2021.

[4] H. Sigel and D. B. McCormick, "Discriminating behavior of metal ions and ligands with regard to their biological significance," *Accounts of Chemical Research*, vol. 3, no. 6, pp. 201–208, 1970.

[5] E. I. Solomon, S. I. Gorelsky, and A. Dey, "Metal–thiolate bonds in bioinorganic chemistry," *Journal of Computational Chemistry*, vol. 27, no. 12, pp. 1415–1428, 2006.

[6] F. A. Cotton and F. A. Cotton, *Advanced inorganic chemistry*. 1999.

[7] C. Andreini, L. Banci, I. Bertini, and A. Rosato, "Zinc through the three domains of life," *Journal of Proteome Research*, vol. 5, no. 11, pp. 3173–3178, 2006.

[8] S. S. Krishna, I. Majumdar, and N. V. Grishin, "Structural classification of zinc fingers: Survey and summary," *Nucleic Acids Research*, vol. 31, no. 2, pp. 532–550, 2003.

[9] M. Cassandri, A. Smirnov, F. Novelli, C. Pitolli, M. Agostini, M. Malewicz, G. Melino, and G. Raschellà, "Zinc-finger proteins in health and disease," *Cell Death Discovery*, vol. 3, no. 1, p. 17071, 2017.

[10] A. Agrawal, S. Johnson, J. Jacobsen, M. Miller, L.-H. Chen, M. Pellecchia, and S. Cohen, "Chelator fragment libraries for targeting metalloproteinases," *ChemMedChem*, vol. 5, no. 2, pp. 195–199, 2010.

[11] D. P. Martin, Z. S. Hann, and S. M. Cohen, "Metalloprotein-inhibitor binding: human carbonic anhydrase ii as a model for probing metal-ligand interactions in a metalloprotein active site," *Inorganic chemistry*, vol. 52, no. 21, pp. 12207–12215, 2013.

[12] C. V. Credille, B. L. Dick, C. N. Morrison, R. W. Stokes, R. N. Adamek, N. C. Wu, I. A. Wilson, and S. M. Cohen, "Structure–activity relationships in metal-binding pharmacophores for influenza endonuclease," *Journal of Medicinal Chemistry*, vol. 61, no. 22, pp. 10206–10217, 2018.

[13] P. J. Kiley and G. Storz, "Exploiting thiol modifications," *PLOS Biology*, vol. 2, no. 11, p. e400, 2004.

[14] Z. Tonzetich, *Biomimetic Metal Thiolates*. 2021.

[15] D. Nakane, Y. Wasada-Tsutsui, Y. Funahashi, T. Hatanaka, T. Ozawa, and H. Masuda, "A novel square-planar ni(ii) complex with an amino-carboxamido-dithiolato-type ligand as an active-site model of nisod," *Inorganic Chemistry*, vol. 53, no. 13, pp. 6512–6523, 2014.

[16] P. T. Truong, E. M. Gale, and T. C. Harrop, "Synthetic models of ni-sod employing imidazole n/s ligand constructs," *Abstracts of Papers of the American Chemical Society*, vol. 244, 2012.

[17] J. L. Boer, S. B. Mulrooney, and R. P. Hausinger, "Nickel-dependent metalloenzymes," *Archives of Biochemistry and Biophysics*, vol. 544, pp. 142–152, 2014.

[18] D. B. Zamble, "Nickel in biology," *Metallomics*, vol. 7, no. 4, pp. 588–589, 2015.

[19] J. W. Cook and J. D. Loudon, "The tropolones," *Quarterly Reviews, Chemical Society*, vol. 5, no. 2, pp. 99–130, 1951.

[20] J. H. Birkinshaw and H. Raistrick, "Studies in the biochemistry of micro-organisms: Puberulic acid c(8)h(6)o(6) and an acid c(8)h(4)o(6), new products of the metabolism of glucose by penicillium puberulum bainier and penicillium aurantio-virens biourge. with an appendix on certain dihydroxybenzenedicarboxylic acids," *The Biochemical journal*, vol. 26, no. 2, pp. 441–453, 1932.

[21] N. Tetsuo, "Über die farbstoffe im holzteile des "hinokl"-baumes. i. hinokitin und hinokitiol(vorläufige mitteilung)," *Bulletin of the Chemical Society of Japan*, vol. 11, no. 3, pp. 295–298, 1936.

[22] J. H. Birkinshaw, A. R. Chambers, and H. Raistrick, "Studies in the biochemistry of micro-organisms: Stipitatic acid, c8h6o5, a metabolic product of penicillium stipitatum thom," *Biochemical Journal*, vol. 36, no. 1-2, pp. 242–251, 1942.

[23] M. J. S. Dewar, "Structure of stipitatic acid," *Nature*, vol. 155, no. 3924, pp. 50–51, 1945.

[24] M. J. S. Dewar, "Structure of colchicine," *Nature*, vol. 155, no. 3927, pp. 141–142, 1945.

[25] R. Bentley, "A fresh look at natural tropolonoids," *Nat Prod Rep*, vol. 25, no. 1, pp. 118–38, 2008.

[26] H. Erdtman and J. Gripenberg, "Antibiotic substances from the heart wood of thuja plicata don," *Nature*, vol. 161, no. 4097, p. 719, 1948.

[27] T. Nozoe, S. Seto, Y. Kitahara, M. Kunori, and Y. Nakayama, "On the synthesis of tropolone (cycloheptatrienolone)," *Proceedings of the Japan Academy*, vol. 26, no. 7, pp. 38–42, 1950.

[28] M. J. S. Dewar, "Tropolone," *Nature*, vol. 166, no. 4227, pp. 790–791, 1950.

[29] H. Guo, D. Roman, and C. Beemelmanns, "Tropolone natural products," *Natural Product Reports*, vol. 36, no. 8, pp. 1137–1155, 2019.

[30] R. L. Redington and T. E. Redington, "Tropolone monomer: Vibrational spectrum and proton tunneling," *Journal of Molecular Spectroscopy*, vol. 78, no. 2, pp. 229–247, 1979.

[31] T. Machiguchi, T. Hasegawa, H. Saitoh, S. Yamabe, and S. Yamazaki, "Solid-state thiotropolone: An extremely rapid intramolecular proton transfer," *The Journal of Organic Chemistry*, vol. 76, no. 13, pp. 5457–5460, 2011.

[32] T. A. Hamor and J. E. Derry, "The crystal structures of tropolone and 4-isopropyltropolone: a comparison," *Acta Crystallographica Section B*, vol. 29, no. 11, pp. 2649–2650, 1973.

[33] H. Shimanouchi and Y. Sasada, "The crystal and molecular structure of tropolone," *Acta Crystallographica Section B*, vol. 29, no. 1, pp. 81–90, 1973.

[34] T. Nozoe, "Substitution products of tropolone and allied compounds," *Nature*, vol. 167, no. 4261, pp. 1055–1057, 1951.

[35] E. Hückel, "Quantentheoretische beiträge zum benzolproblem," *Zeitschrift für Physik*, vol. 70, no. 3, pp. 204–286, 1931.

[36] F. Pietra, "Seven-membered conjugated carbo- and heterocyclic compounds and their homoconjugated analogs and metal complexes. synthesis, biosynthesis, structure, and reactivity," *Chemical Reviews*, vol. 73, no. 4, pp. 293–364, 1973.

[37] Y. Dutt, R. P. Singh, and M. Katyal, "Metal complexes with tropolones," *Talanta*, vol. 16, no. 10, pp. 1369–1382, 1969.

[38] W. v. E. Doering and L. H. Knox, "Rearrangement of halotropones. chloride exchange in tribromotropolone," *Journal of the American Chemical Society*, vol. 74, no. 22, pp. 5683–5687, 1952.

[39] E. L. Muetterties and C. M. Wright, "Chelate chemistry. i. tropolone and aminotroponimine derivatives of the main-group elements," *Journal of the American Chemical Society*, vol. 86, no. 23, pp. 5132–5137, 1964.

[40] E. L. Muetterties, H. Roesky, and C. M. Wright, "Chelate chemistry. v. metal chelates based on tropolone and its derivatives," *Journal of the American Chemical Society*, vol. 88, no. 21, pp. 4856–4861, 1966.

[41] C. E. Forbes and R. H. Holm, "Dithiotropolone (2-mercaptocycloheptatrienethione) and its metal complexes," *Journal of the American Chemical Society*, vol. 90, no. 24, pp. 6884–6885, 1968.

[42] T. Nozoe, M. Sato, and K. Matsui, "Mercaptotropone and some of its allied compounds," *Proceedings of the Japan Academy*, vol. 29, pp. 22–26, 1953.

[43] T. Nozoe and K. Matsui, "On the structure of 2-mercaptotropones," *Bulletin of the Chemical Society of Japan*, vol. 34, no. 5, pp. 616–618, 1961.

[44] C. E. Forbes and R. H. Holm, "Dithiotropolonates. ii. synthesis and properties of dithiotropolone and its metal(ii) complexes," *Journal of the American Chemical Society*, vol. 92, no. 8, pp. 2297–2303, 1970.

[45] B. L. Dick, A. Patel, J. A. McCammon, and S. M. Cohen, "Effect of donor atom identity on metal-binding pharmacophore coordination," *Journal of biological inorganic chemistry : JBIC : a publication of the Society of Biological Inorganic Chemistry*, vol. 22, no. 4, pp. 605–613, 2017.

[46] H. Murakami, H. Yasui, and Y. Yoshikawa, "Pharmacological and pharmacokinetic studies of anti-diabetic tropolonato-zn(ii) complexes with zn(s(2)o(2)) coordination mode," *Chem Pharm Bull (Tokyo)*, vol. 60, no. 9, pp. 1096–104, 2012.

[47] M. C. Barret, P. H. Bhatia, G. Kociok-Köhn, and K. C. Molloy, "New copper(ii) 2-(alkylamino)troponates," *Transition Metal Chemistry*, vol. 39, no. 5, pp. 543–551, 2014.

[48] E. L. Muetterties and C. M. Wright, "Chelate chemistry. ii.1 hydrolysis of metal tropolonates," *Journal of the American Chemical Society*, vol. 87, no. 1, pp. 21–24, 1965.

[49] E. L. Muetterties and C. M. Wright, "Chelate chemistry. iii. chelates of high coordination number," *Journal of the American Chemical Society*, vol. 87, no. 21, pp. 4706–4717, 1965.

[50] E. L. Muetterties, "Chelate chemistry. iv. ten-coordinate thorium and uranium (iv)," *Journal of the American Chemical Society*, vol. 88, no. 2, pp. 305–306, 1966.

[51] M. D. Lind, B. Lee, and J. L. Hoard, "Structure and bonding in a ten-coordinate lanthanum(iii) chelate of ethylenediaminetetraacetic acid1," *Journal of the American Chemical Society*, vol. 87, no. 7, pp. 1611–1612, 1965.

[52] F. Cao, C. Orth, M. J. Donlin, P. Adegboyega, M. J. Meyers, R. P. Murelli, M. Elagawany, B. Elgendy, and J. E. Tavis, "Synthesis and evaluation of troponoids as a new class of antibiotics," *ACS Omega*, vol. 3, no. 11, pp. 15125–15133, 2018.

[53] M. Elagawany, L. Hegazy, F. Cao, M. J. Donlin, N. Rath, J. Tavis, and B. Elgendy, "Identification of 4-isopropyl-thiotropolone as a novel anti-microbial: regioselective synthesis, nmr characterization, and biological evaluation," *Rsc Advances*, vol. 8, no. 52, pp. 29967–29975, 2018.

[54] J. A. McCleverty, N. M. Atherton, N. G. Connelly, and C. J. Winscom, "Transition-metal dithiolenes. part vii. five- and six-co-ordinate lewis-base complexes of cobalt and iron bisdithiolenes," *Journal of the Chemical Society A: Inorganic, Physical, Theoretical*, no. 0, pp. 2242–2257, 1969.

[55] G. N. Schrauzer, "Coordination compounds with delocalized ground states. transition metal derivatives of dithiodiketones and ethylene-1,2-dithiolates (metal dithienes)," *Accounts of Chemical Research*, vol. 2, no. 3, pp. 72–80, 1969.

[56] T. J. Anderson, M. A. Neuman, and G. A. Melson, "Coordination chemistry of scandium. vii. crystal and molecular structure of hydrogentetrakis(tropolonato)scandium(iii), a scandium(iii) complex with approximate d2d dodecahedral stereochemistry," *Inorganic Chemistry*, vol. 13, no. 8, pp. 1884–1890, 1974.

[57] A. Avdeef, J. A. Costamagna, and J. P. Fackler, "Crystal and molecular structure of tris(tropolonato)manganese(iii), mn(o2c7h5)3, a high-spin complex having structural fea-

tures consistent with jahn-teller behavior for two distinct mno6 centers," *Inorganic Chemistry*, vol. 13, no. 8, pp. 1854–1863, 1974.

[58] T. A. Hamor and D. J. Watkin, "The crystal structure of tris(tropolonato)iron(iii)("ferric tropolone")," *Journal of the Chemical Society D: Chemical Communications*, no. 9, pp. 440–441, 1969.

[59] R. J. Irving, M. L. Post, and R. W. Baker, "Crystal and molecular structure of a tetranuclear cobalt(ii)–tropolonate complex: [co4(c7h5o2)8(h2o)2]," *Journal of the Chemical Society, Dalton Transactions*, no. 19, pp. 1898–1902, 1975.

[60] D. Doddrell, M. Bendall, P. Healy, G. Smith, C. Kennard, C. Raston, and A. White, "59co and 13c nuclear spin relaxation studies in solutions of symmetric, bidentate cobalt(iii) complexes. on the mechanism of 59co spin relaxation. crystal structure determination of tris(tropolonato)cobalt(iii)," *Australian Journal of Chemistry*, vol. 32, no. 6, pp. 1219–1230, 1979.

[61] H. Suzuki, S.-i. Matsumura, Y. Satoh, K. Sogoh, and H. Yasuda, "Random copolymerizations of norbornene with other monomers catalyzed by novel ni compounds involving n- or o-donated ligands," *Reactive and Functional Polymers*, vol. 58, no. 2, pp. 77–91, 2004.

[62] W. M. Macintyre, J. M. Robertson, and R. F. Zahrobsky, "The crystal structure of cupric tropolone: A refinement," *Proceedings of the Royal Society of London. Series A, Mathematical and Physical Sciences*, vol. 289, no. 1417, pp. 161–170, 1966.

[63] J.-E. Berg, A.-M. Pilotti, A.-C. Soderholm, and B. Karlsson, "Bis(tropolonato)copper(ii)," *Acta Crystallographica Section B*, vol. 34, no. 10, pp. 3071–3072, 1978.

[64] M. C. Barret, M. F. Mahon, K. C. Molloy, J. W. Steed, and P. Wright, "Synthesis and structural characterization of tin(ii) and zinc(ii) derivatives of cyclic alpha-hydroxyketones, including the structures of sn(maltol)(2), sn(tropolone)(2), zn(tropolone)(2), and zn(hinokitiol)(2)," *Inorg Chem*, vol. 40, no. 17, pp. 4384–8, 2001.

[65] D. A. Clemente, G. Bandoli, M. Vidali, P. A. Vigato, R. Portanova, and L. Magon, "Crystal and molecular structure of bis(tropolonato)-dioxo-(ethanol)uranium(vi)," *Journal of Crystal and Molecular Structure*, vol. 3, no. 4, pp. 221–233, 1973.

[66] K. Lyczko, M. Lyczko, K. Wozniak, M. Stachowicz, W. P. Oziminski, and K. Kubo, "Influence of ph and type of counterion on the formation of bismuth(iii) complexes with tropolonato and 5-methyltropolonato ligands: Synthesis, structure, spectroscopic characterization and calculation studies," *Inorganica Chimica Acta*, vol. 436, pp. 57–68, 2015.

[67] F. Nepveu, F. Jasanada, and L. Walz, "Structural characterization of two lipophilic tris(tropolonato) gallium(iii) and indium(iii) complexes of radiopharmaceutical interest," *Inorganica Chimica Acta*, vol. 211, no. 2, pp. 141–147, 1993.

[68] K. Nomiya, A. Yoshizawa, K. Tsukagoshi, N. C. Kasuga, S. Hirakawa, and J. Watanabe, "Synthesis and structural characterization of silver(i), aluminium(iii) and cobalt(ii) complexes with 4-isopropyltropolone (hinokitiol) showing noteworthy biological activities. action of silver(i)-oxygen bonding complexes on the antimicrobial activities," *J Inorg Biochem*, vol. 98, no. 1, pp. 46–60, 2004.

[69] K. Nomiya, A. Yoshizawa, N. C. Kasuga, H. Yokoyama, and S. Hirakawa, "Synthesis, solid-state characterization and antimicrobial activities of three different polymorphs of a copper(ii) complex with 4-isopropyltropolone (hinokitiol)," *Inorganica Chimica Acta*, vol. 357, no. 4, pp. 1168–1176, 2004.

[70] A. S. Grillo, A. M. SantaMaria, M. D. Kafina, A. G. Cioffi, N. C. Huston, M. Han, Y. A. Seo, Y. Y. Yien, C. Nardone, A. V. Menon, J. Fan, D. C. Svoboda, J. B. Anderson, J. D. Hong, B. G. Nicolau, K. Subedi, A. A. Gewirth, M. Wessling-Resnick, J. Kim, B. H. Paw, and M. D. Burke, "Restored iron transport by a small molecule promotes absorption and hemoglobinization in animals," *Science*, vol. 356, no. 6338, pp. 608–616, 2017.

[71] M. C. Barret, P. H. Bhatia, G. Kociok-Kohn, and K. C. Molloy, "New copper(ii) 2-(alkylamino)troponates," *Transition Metal Chemistry*, vol. 39, no. 5, pp. 543–551, 2014.

[72] K. Nakano, T. Chigira, T. Miyafusa, S. Nagatoishi, J. M. M. Caaveiro, and K. Tsumoto, "Discovery and characterization of natural tropolones as inhibitors of the antibacterial target capf from staphylococcus aureus," *Scientific Reports*, vol. 5, no. 1, p. 15337, 2015.

[73] A. S. Lee, H. de Lencastre, J. Garau, J. Kluytmans, S. Malhotra-Kumar, A. Peschel, and S. Harbarth, "Methicillin-resistant staphylococcus aureus," *Nature Reviews Disease Primers*, vol. 4, no. 1, p. 18033, 2018.

[74] A. D. Pannifer, T. Y. Wong, R. Schwarzenbacher, M. Renatus, C. Petosa, J. Bienkowska, D. B. Lacy, R. J. Collier, S. Park, S. H. Leppla, P. Hanna, and R. C. Liddington, "Crystal structure of the anthrax lethal factor," *Nature*, vol. 414, no. 6860, pp. 229–233, 2001.

[75] F. E. Jacobsen, J. A. Lewis, K. J. Heroux, and S. M. Cohen, "Characterization and evaluation of pyrone and tropolone chelators for use in metalloprotein inhibitors," *Inorganica Chimica Acta*, vol. 360, no. 1, pp. 264–272, 2007.

[76] W. T. Ismaya, H. J. Rozeboom, A. Weijn, J. J. Mes, F. Fusetti, H. J. Wichers, and B. W. Dijkstra, "Crystal structure of agaricus bisporus mushroom tyrosinase: Identity of the tetramer subunits and interaction with tropolone," *Biochemistry*, vol. 50, no. 24, pp. 5477–5486, 2011.

[77] J. A. Jacobsen, J. L. Fullagar, M. T. Miller, and S. M. Cohen, "Identifying chelators for metalloprotein inhibitors using a fragment-based approach," *Journal of Medicinal Chemistry*, vol. 54, no. 2, pp. 591–602, 2011.

[78] D. Rogolino, M. Carcelli, M. Sechi, and N. Neamati, "Viral enzymes containing magnesium: Metal binding as a successful strategy in drug design," *Coordination Chemistry Reviews*, vol. 256, no. 23, pp. 3063–3086, 2012.

[79] J. Didierjean, C. Isel, F. Querré, J. F. Mouscadet, A. M. Aubertin, J. Y. Valnot, S. R. Piettre, and R. Marquet, "Inhibition of human immunodeficiency virus type 1 reverse transcriptase, rnase h, and integrase activities by hydroxytropolones," *Antimicrob Agents Chemother*, vol. 49, no. 12, pp. 4884–94, 2005.

[80] P. Borowski, M. Lang, A. Haag, and A. Baier, "Tropolone and its derivatives as inhibitors of the helicase activity of hepatitis c virus nucleotide triphosphatase/helicase," *Antivir Chem Chemother*, vol. 18, no. 2, pp. 103–9, 2007.

[81] N. B. Agyemang, C. R. Kukla, T. C. Edwards, Q. Li, M. K. Langen, A. Schaal, A. D. Franson, A. G. Casals, K. A. Donald, A. J. Yu, M. J. Donlin, L. A. Morrison, J. E. Tavis, and R. P. Murelli, "Divergent synthesis of a thiolate-based aplha-hydroxytropolone library with a dynamic bioactivity profile," *RSC Adv*, vol. 9, no. 59, pp. 34227–34234, 2019.

[82] S. N. Ononye, M. D. VanHeyst, E. Z. Oblak, W. Zhou, M. Ammar, A. C. Anderson, and D. L. Wright, "Tropolones as lead-like natural products: the development of potent and selective histone deacetylase inhibitors," *ACS Med Chem Lett*, vol. 4, no. 8, pp. 757–61, 2013.

[83] S. K. Kurdistani, S. Tavazoie, and M. Grunstein, "Mapping global histone acetylation patterns to gene expression," *Cell*, vol. 117, no. 6, pp. 721–733, 2004.

[84] M. Y. Mboge, B. P. Mahon, R. McKenna, and S. C. Frost, "Carbonic anhydrases: Role in ph control and cancer," *Metabolites*, vol. 8, no. 1, p. 19, 2018.

[85] J. C. Mallory, G. Crudden, A. Oliva, C. Saunders, A. Stromberg, and R. J. Craven, "A novel group of genes regulates susceptibility to antineoplastic drugs in highly tumorigenic breast cancer cells," *Molecular Pharmacology*, vol. 68, no. 6, p. 1747, 2005.

[86] D. Miyamoto, Y. Kusagaya, N. Endo, A. Sometani, S. Takeo, T. Suzuki, Y. Arima, K. Nakajima, and Y. Suzuki, "Thujaplicin-copper chelates inhibit replication of human influenza viruses," *Antiviral Res*, vol. 39, no. 2, pp. 89–100, 1998.

[87] L. M. Balsa, M. C. Ruiz, L. Santa Maria de la Parra, E. J. Baran, and I. E. León, "Anticancer and antimetastatic activity of copper(ii)-tropolone complex against human breast cancer cells, breast multicellular spheroids and mammospheres," *Journal of Inorganic Biochemistry*, vol. 204, p. 110975, 2020.

[88] X. Chen, X. Zhang, J. Chen, Q. Yang, L. Yang, D. Xu, P. Zhang, X. Wang, and J. Liu, "Hinokitiol copper complex inhibits proteasomal deubiquitination and induces paraptosis-like cell death in human cancer cells," *European Journal of Pharmacology*, vol. 815, pp. 147–155, 2017.

[89] B. M. Krenn, E. Gaudernak, B. Holzer, K. Lanke, F. J. Van Kuppeveld, and J. Seipelt, "Antiviral activity of the zinc ionophores pyrithione and hinokitiol against picornavirus infections," *J Virol*, vol. 83, no. 1, pp. 58–64, 2009.

[90] A. Shisheva, D. Gefel, and Y. Shechter, "Insulinlike effects of zinc ion in vitro and in vivo: Preferential effects on desensitized adipocytes and induction of normoglycemia in streptozocin-induced rats," *Diabetes*, vol. 41, no. 8, p. 982, 1992.

[91] H. Sakurai and Y. Adachi, "The pharmacology of the insulinomimetic effect of zinc complexes," *Biometals*, vol. 18, no. 4, pp. 319–23, 2005.

[92] M. Yamane, Y. Adachi, Y. Yoshikawa, and H. Sakurai, "A new anti-diabetic zn(ii)–hinokitiol (β-thujaplicin) complex with zn(o4) coordination mode," *Chemistry Letters*, vol. 34, no. 12, pp. 1694–1695, 2005.

[93] M. Yamaguchi, K. Wakasugi, R. Saito, Y. Adachi, Y. Yoshikawa, H. Sakurai, and A. Katoh, "Syntheses of vanadyl and zinc(ii) complexes of 1-hydroxy-4,5,6-substituted 2(1h)-pyrimidinones and their insulin-mimetic activities," *J Inorg Biochem*, vol. 100, no. 2, pp. 260–9, 2006.

[94] Y. Yoshikawa, M. Kondo, H. Sakurai, and Y. Kojima, "A family of insulinomimetic zinc(ii) complexes of amino ligands with zn(nn) (n=3 and 4) coordination modes," *J Inorg Biochem*, vol. 99, no. 7, pp. 1497–503, 2005.

[95] M. Nakai, F. Sekiguchi, M. Obata, C. Ohtsuki, Y. Adachi, H. Sakurai, C. Orvig, D. Rehder, and S. Yano, "Synthesis and insulin-mimetic activities of metal complexes with 3-hydroxypyridine-2-carboxylic acid," *J Inorg Biochem*, vol. 99, no. 6, pp. 1275–82, 2005.

[96] Y. Naito, Y. Yoshikawa, M. Shintani, S. Kamoshida, N. Kajiwara, and H. Yasui, "Anti-hyperglycemic effect of long-term bis(hinokitiolato)zinc complex ([zn(hkt)(2)]) ingestion on insulin resistance and pancreatic islet cells protection in type 2 diabetic kk-a(y) mice," *Biol Pharm Bull*, vol. 40, no. 3, pp. 318–326, 2017.

[97] R. Suzuki, Y. Inoue, I. Murata, H. Nomura, Y. Isshiki, M. Hashimoto, Y. Kudo, H. Kitagishi, S. Kondo, and I. Kanamoto, "Preparation, characterization, and study of the antimicrobial activity of a hinokitiol-copper(ii)/γ-cyclodextrin ternary complex," *Journal of Molecular Structure*, vol. 1194, pp. 19–27, 2019.

[98] D. Miyamoto, Y. Kusagaya, N. Endo, A. Sometani, T. Seiji, T. Suzuki, Y. Arima, K. Nakajima, and S. Yasuo, "Thujaplicin–copper chelates inhibit replication of human influenza viruses," *Antiviral Research*, vol. 39, no. 2, pp. 89–100, 1998.

[99] Y. R. Guo, Q. D. Cao, Z. S. Hong, Y. Y. Tan, S. D. Chen, H. J. Jin, K. S. Tan, D. Y. Wang, and Y. Yan, "The origin, transmission and clinical therapies on coronavirus disease 2019 (covid-19) outbreak - an update on the status," *Mil Med Res*, vol. 7, no. 1, p. 11, 2020.

[100] L. Zhang and Y. H. Liu, "Potential interventions for novel coronavirus in china: A systematic review," *Journal of Medical Virology*, vol. 92, no. 5, pp. 479–490, 2020.

[101] J. S. Morse, T. Lalonde, S. Q. Xu, and W. R. Liu, "Learning from the past: Possible urgent prevention and treatment options for severe acute respiratory infections caused by 2019-ncov," *Chembiochem*, vol. 21, no. 5, pp. 730–738, 2020.

[102] D. M. Mellott, C.-T. Tseng, A. Drelich, P. Fajtová, B. C. Chenna, D. H. Kostomiris, J. Hsu, J. Zhu, Z. W. Taylor, K. I. Kocurek, V. Tat, A. Katzfuss, L. Li, M. A. Giardini, D. Skinner, K. Hirata, M. C. Yoon, S. Beck, A. F. Carlin, A. E. Clark, L. Beretta, D. Maneval, V. Hook, F. Frueh, B. L. Hurst, H. Wang, F. M. Raushel, A. J. O'Donoghue, J. L. de Siqueira-Neto, T. D. Meek, and J. H. McKerrow, "A clinical-stage cysteine protease inhibitor blocks sars-cov-2 infection of human and monkey cells," *ACS Chemical Biology*, vol. 16, no. 4, pp. 642–650, 2021.

[103] Z. Jin, Y. Zhao, Y. Sun, B. Zhang, H. Wang, Y. Wu, Y. Zhu, C. Zhu, T. Hu, X. Du, Y. Duan, J. Yu, X. Yang, X. Yang, K. Yang, X. Liu, L. W. Guddat, G. Xiao, L. Zhang, H. Yang, and Z. Rao, "Structural basis for the inhibition of sars-cov-2 main protease by antineoplastic drug carmofur," *Nat Struct Mol Biol*, vol. 27, no. 6, pp. 529–532, 2020.

[104] A. Pandey, A. N. Nikam, A. B. Shreya, S. P. Mutalik, D. Gopalan, S. Kulkarni, B. S. Padya, G. Fernandes, S. Mutalik, and R. Prassl, "Potential therapeutic targets for combating sars-cov-2: Drug repurposing, clinical trials and recent advancements," *Life Sci*, vol. 256, p. 117883, 2020.

[105] Y. Huang, C. Yang, X.-f. Xu, W. Xu, and S.-w. Liu, "Structural and functional properties of sars-cov-2 spike protein: potential antivirus drug development for covid-19," *Acta Pharmacologica Sinica*, vol. 41, no. 9, pp. 1141–1149, 2020.

[106] M. Gheblawi, K. Wang, A. Viveiros, Q. Nguyen, J.-C. Zhong, A. J. Turner, M. K. Raizada, M. B. Grant, and G. Y. Oudit, "Angiotensin-converting enzyme 2: Sars-cov-2 receptor and regulator of the renin-angiotensin system: Celebrating the 20th anniversary of the discovery of ace2," *Circulation research*, vol. 126, no. 10, pp. 1456–1474, 2020.

[107] C. Liu, Q. Q. Zhou, Y. Z. Li, L. V. Garner, S. P. Watkins, L. J. Carter, J. Smoot, A. C. Gregg, A. D. Daniels, S. Jervey, and D. Albaiu, "Research and development on therapeutic agents and vaccines for covid-19 and related human coronavirus diseases," *Acs Central Science*, vol. 6, no. 3, pp. 315–331, 2020.

[108] A. J. te Velthuis, S. H. van den Worm, A. C. Sims, R. S. Baric, E. J. Snijder, and M. J. van Hemert, "Zn(2+) inhibits coronavirus and arterivirus rna polymerase activity in vitro and zinc ionophores block the replication of these viruses in cell culture," *PLoS Pathog*, vol. 6, no. 11, p. e1001176, 2010.

[109] J. R. Schwartz, "Zinc pyrithione: A topical antimicrobial with complex pharmaceutics," *J Drugs Dermatol*, vol. 15, no. 2, pp. 140–4, 2016.

[110] B. M. Krenn, B. Holzer, E. Gaudernak, A. Triendl, F. J. van Kuppeveld, and J. Seipelt, "Inhibition of polyprotein processing and rna replication of human rhinovirus by pyrrolidine dithiocarbamate involves metal ions," *J Virol*, vol. 79, no. 22, pp. 13892–9, 2005.

[111] K. Lanke, B. M. Krenn, W. J. Melchers, J. Seipelt, and F. J. van Kuppeveld, "Pdtc inhibits picornavirus polyprotein processing and rna replication by transporting zinc ions into cells," *J Gen Virol*, vol. 88, no. Pt 4, pp. 1206–17, 2007.

[112] H. Shan, J. Liu, J. Shen, J. Dai, G. Xu, K. Lu, C. Han, Y. Wang, X. Xu, Y. Tong, H. Xiang, Z. Ai, G. Zhuang, J. Hu, Z. Zhang, Y. Li, L. Pan, and L. Tan, "Development of potent and selective inhibitors targeting the papain-like protease of sars-cov-2," *Cell Chem Biol*, 2021.

[113] C. A. Ramos-Guzmán, J. J. Ruiz-Pernía, and I. Tuñón, "Unraveling the sars-cov-2 main protease mechanism using multiscale methods," *ACS Catalysis*, vol. 10, no. 21, pp. 12544–12554, 2020.

[114] H. Yang and J. Yang, "A review of the latest research on mpro targeting sars-cov inhibitors," *RSC Medicinal Chemistry*, vol. 12, no. 7, pp. 1026–1036, 2021.

[115] J. T. Hsu, C. J. Kuo, H. P. Hsieh, Y. C. Wang, K. K. Huang, C. P. Lin, P. F. Huang, X. Chen, and P. H. Liang, "Evaluation of metal-conjugated compounds as inhibitors of 3cl protease of sars-cov," *FEBS Lett*, vol. 574, no. 1-3, pp. 116–20, 2004.

[116] R. S. Ochs, "Understanding enzyme inhibition," *Journal of Chemical Education*, vol. 77, no. 11, p. 1453, 2000.

[117] C. C. Lee, C. J. Kuo, M. F. Hsu, P. H. Liang, J. M. Fang, J. J. Shie, and A. H. Wang, "Structural basis of mercury- and zinc-conjugated complexes as sars-cov 3c-like protease inhibitors," *FEBS Lett*, vol. 581, no. 28, pp. 5454–8, 2007.

[118] M. Lazarczyk and M. Favre, "Role of zn2+ ions in host-virus interactions," *J Virol*, vol. 82, no. 23, pp. 11486–94, 2008.

[119] P. Bonaventura, G. Benedetti, F. Albarede, and P. Miossec, "Zinc and its role in immunity and inflammation," *Autoimmun Rev*, vol. 14, no. 4, pp. 277–85, 2015.

[120] A. Kumar, Y. Kubota, M. Chernov, and H. Kasuya, "Potential role of zinc supplementation in prophylaxis and treatment of covid-19," *Medical hypotheses*, vol. 144, pp. 109848–109848, 2020.

[121] A. V. Skalny, L. Rink, O. P. Ajsuvakova, M. Aschner, V. A. Gritsenko, S. I. Alekseenko, A. A. Svistunov, D. Petrakis, D. A. Spandidos, J. Aaseth, A. Tsatsakis, and A. A. Tinkov, "Zinc and respiratory tract infections: Perspectives for covid19 (review)," *Int J Mol Med*, 2020.

[122] D. C. Pectol, C. R. DeLaney, J. Zhu, D. M. Mellott, A. Katzfuss, Z. W. Taylor, T. D. Meek, and M. Y. Darensbourg, "Dinitrosyl iron complexes (dnics) as inhibitors of the sars-cov-2 main protease," *Chemical Communications*, 2021.

[123] R. Ting, L. Lermer, and D. M. Perrin, "Triggering dnazymes with light: A photoactive c8 thioether-linked adenosine," *Journal of the American Chemical Society*, vol. 126, no. 40, pp. 12720–12721, 2004.

[124] R. M. Jenkins, M. L. Singleton, E. Almaraz, J. H. Relbenspies, and M. Y. Darensbourg, "Imidazole-containing (n3s)-ni-ii complexes relating to nickel containing biomolecules," *Inorganic Chemistry*, vol. 48, no. 15, pp. 7280–7293, 2009.

[125] O. V. Dolomanov, A. J. Blake, N. R. Champness, and M. Schroder, "Olex: new software for visualization and analysis of extended crystal structures," *Journal of Applied Crystallography*, vol. 36, no. 5, pp. 1283–1284, 2003.

[126] A. Andres, M. Roses, C. Rafols, E. Bosch, S. Espinosa, V. Segarra, and J. M. Huerta, "Setup and validation of shake-flask procedures for the determination of partition coefficients (logd) from low drug amounts," *Eur J Pharm Sci*, vol. 76, pp. 181–91, 2015.

[127] E. F. Pettersen, T. D. Goddard, C. C. Huang, G. S. Couch, D. M. Greenblatt, E. C. Meng, and T. E. Ferrin, "Ucsf chimera - a visualization system for exploratory research and analysis," *Journal of Computational Chemistry*, vol. 25, no. 13, pp. 1605–1612, 2004.

[128] M. T. Marty, A. J. Baldwin, E. G. Marklund, G. K. A. Hochberg, J. L. P. Benesch, and C. V. Robinson, "Bayesian deconvolution of mass and ion mobility spectra: From binary interactions to polydisperse ensembles," *Analytical Chemistry*, vol. 87, no. 8, pp. 4370–4376, 2015.

[129] T. Fiedler, L. Chen, N. D. Wagner, D. H. Russell, and J. A. Gladysz, "Gas and liquid phase diffusivities of isomeric metal complexes derived from multifold ring-closing metatheses: Ion mobility mass spectrometry trumps dosy nmr," *Organometallics*, vol. 35, no. 12, pp. 2071–2075, 2016.

[130] M. R. Willcott, "Mestre nova," *Journal of the American Chemical Society*, vol. 131, no. 36, pp. 13180–13180, 2009.

[131] H. H. Zeng, E. G. Matveeva, A. K. Stoddard, C. A. Fierke, and R. B. Thompson, "Long wavelength fluorescence ratiometric zinc biosensor," *J Fluoresc*, vol. 23, no. 3, pp. 375–9, 2013.

[132] T. Marzo and L. Messori, "A role for metal-based drugs in fighting covid-19 infection? the case of auranofin," *ACS Med Chem Lett*, vol. 11, no. 6, pp. 1067–1068, 2020.

[133] E. C. Vatansever, K. S. Yang, A. K. Drelich, K. C. Kratch, C.-C. Cho, K. R. Kempaiah, J. C. Hsu, D. M. Mellott, S. Xu, C.-T. K. Tseng, and W. R. Liu, "Bepridil is potent against sars-cov-2 in vitro," *Proceedings of the National Academy of Sciences*, vol. 118, no. 10, p. e2012201118, 2021.

[134] G. J. Lockbaum, A. C. Reyes, J. M. Lee, R. Tilvawala, E. A. Nalivaika, A. Ali, N. Kurt Yilmaz, P. R. Thompson, and C. A. Schiffer, "Crystal structure of sars-cov-2 main protease in complex with the non-covalent inhibitor ml188," *Viruses*, vol. 13, no. 2, p. 174, 2021.

[135] M. Bzówka, K. Mitusińska, A. Raczyńska, A. Samol, J. A. Tuszyński, and A. Góra, "Structural and evolutionary analysis indicate that the sars-cov-2 mpro is a challenging target for small-molecule inhibitor design," *International journal of molecular sciences*, vol. 21, no. 9, p. 3099, 2020.

[136] W. Dai, B. Zhang, X.-M. Jiang, H. Su, J. Li, Y. Zhao, X. Xie, Z. Jin, J. Peng, F. Liu, C. Li, Y. Li, F. Bai, H. Wang, X. Cheng, X. Cen, S. Hu, X. Yang, J. Wang, X. Liu, G. Xiao, H. Jiang, Z. Rao, L.-K. Zhang, Y. Xu, H. Yang, and H. Liu, "Structure-based design of antiviral drug candidates targeting the sars-cov-2 main protease," *Science*, vol. 368, no. 6497, pp. 1331–1335, 2020.

[137] D. M. Mellott, C. T. Tseng, A. Drelich, P. Fajtova, B. C. Chenna, D. H. Kostomiris, J. Hsu, J. Zhu, Z. W. Taylor, V. Tat, A. Katzfuss, L. Li, M. A. Giardini, D. Skinner, K. Hirata, S. Beck, A. F. Carlin, A. E. Clark, L. Beretta, D. Maneval, F. Frueh, B. L. Hurst, H. Wang, K. I. Kocurek, F. M. Raushel, A. J. O'Donoghue, J. L. de Siqueira-Neto, T. D. Meek, and J. H. McKerrow, "A cysteine protease inhibitor blocks sars-cov-2 infection of human and monkey cells," *bioRxiv*, 2020.

[138] T. Pillaiyar, M. Manickam, V. Namasivayam, Y. Hayashi, and S. H. Jung, "An overview of severe acute respiratory syndrome-coronavirus (sars-cov) 3cl protease inhibitors: Peptidomimetics and small molecule chemotherapy," *Journal of Medicinal Chemistry*, vol. 59, no. 14, pp. 6595–6628, 2016.

[139] J. J. Kozak, H. B. Gray, and R. A. Garza-Lopez, "Structural stability of the sars-cov-2 main protease: Can metal ions affect function?," *J Inorg Biochem*, vol. 211, p. 111179, 2020.

[140] R. A. Garza-Lopez, J. J. Kozak, and H. B. Gray, "Copper(ii) inhibition of the sars-cov-2 main protease," *ChemRxiv : the preprint server for chemistry*, p. 10.26434/chemrxiv.12673436.v1, 2020.

[141] K. Rodriguez, R. Josselin, E. Audoux, F. Saunier, E. Botelho-Nevers, A. Prier, Y. Dickerscheit, S. Pillet, B. Pozzetto, T. Bourlet, and P. O. Verhoeven, "Evaluation of in vitro activity of copper gluconate against sars-cov-2 using confocal microscopy-based high content screening," *bioRxiv*, p. 2020.12.13.422548, 2020.

[142] J. Karges, M. Kalaj, M. Gembicky, and S. M. Cohen, "Re(i) tricarbonyl complexes as coordinate covalent inhibitors for the sars-cov-2 main cysteine protease," *Angew Chem Int Ed*

Engl, vol. 60, no. 19, pp. 10716–10723, 2021.

[143] B. D. Korant, J. C. Kauer, and B. E. Butterworth, "Zinc ions inhibit replication of rhinoviruses," *Nature*, vol. 248, no. 449, pp. 588–90, 1974.

[144] S. A. Read, S. Obeid, C. Ahlenstiel, and G. Ahlenstiel, "The role of zinc in antiviral immunity," *Advances in Nutrition*, vol. 10, no. 4, pp. 696–710, 2019.

[145] G. A. Eby, "Zinc ion availability - the determinant of efficacy in zinc lozenge treatment of common colds," *Journal of Antimicrobial Chemotherapy*, vol. 40, no. 4, pp. 483–493, 1997.

[146] H. Irving and R. J. P. Williams, "637. the stability of transition-metal complexes," *Journal of the Chemical Society (Resumed)*, no. 0, pp. 3192–3210, 1953.

[147] D. Jothimani, E. Kailasam, S. Danielraj, B. Nallathambi, H. Ramachandran, P. Sekar, S. Manoharan, V. Ramani, G. Narasimhan, I. Kaliamoorthy, and M. Rela, "Covid-19: Poor outcomes in patients with zinc deficiency," *Int J Infect Dis*, vol. 100, pp. 343–349, 2020.

[148] B. X. Hoang and B. Han, "A possible application of hinokitiol as a natural zinc ionophore and anti-infective agent for the prevention and treatment of covid-19 and viral infections," *Medical Hypotheses*, vol. 145, p. 110333, 2020.

[149] B. X. Hoang, H. Q. Hoang, and B. Han, "Zinc iodide in combination with dimethyl sulfoxide for treatment of sars-cov-2 and other viral infections," *Medical Hypotheses*, vol. 143, p. 109866, 2020.

[150] M. O. Shittu and O. I. Afolami, "Improving the efficacy of chloroquine and hydroxychloroquine against sars-cov-2 may require zinc additives - a better synergy for future covid-19 clinical trials," *Infez Med*, vol. 28, no. 2, pp. 192–197, 2020.

[151] P. M. Carlucci, T. Ahuja, C. Petrilli, H. Rajagopalan, S. Jones, and J. Rahimian, "Zinc sulfate in combination with a zinc ionophore may improve outcomes in hospitalized covid-19 patients," *Journal of Medical Microbiology*, vol. 69, no. 10, pp. 1228–1234, 2020.

[152] Y. Adachi, J. Yoshida, Y. Kodera, and H. Sakurai, "A highly potent insulin-mimetic zinc(ii) complex with a zn(s2o2) coordination mode: Bis(1,6-dimethyl-3-hydroxy-5-methoxy-2-pentyl-1,4-dihydropyridine-4-thionato)zinc(ii)," *Chemistry Letters*, vol. 34, no. 5, pp. 656–657, 2005.

[153] T. Jakusch, K. Gajda-Schrantz, Y. Adachi, H. Sakurai, T. Kiss, and L. Horvath, "Solution equilibrium characterization of insulin-mimetic zn(ii) complexes," *J Inorg Biochem*, vol. 100, no. 9, pp. 1521–6, 2006.

[154] J. L. Fullagar, A. L. Garner, A. K. Struss, J. A. Day, D. P. Martin, J. Yu, X. Cai, K. D. Janda, and S. M. Cohen, "Antagonism of a zinc metalloprotease using a unique metal-chelating scaffold: tropolones as inhibitors of p. aeruginosa elastase," *Chem Commun (Camb)*, vol. 49, no. 31, pp. 3197–9, 2013.

[155] K. S. Yang, X. Y. R. Ma, Y. Y. Ma, Y. R. Alugubelli, D. A. Scott, E. C. Vatansever, A. K. Drelich, B. Sankaran, Z. Z. Geng, L. R. Blankenship, H. E. Ward, Y. J. Sheng, J. C. Hsu, K. C. Kratch, B. Y. Zhao, H. S. Hayatshahi, J. Liu, P. W. Li, C. A. Fierke, C. T. Tseng, S. Q. Xu, and W. R. Liu, "A quick route to multiple highly potent sars-cov-2 main protease inhibitors**," *Chemmedchem*, vol. 16, no. 6, pp. 942–948, 2021.

[156] A. Okuniewski, D. Rosiak, J. Chojnacki, and B. Becker, "Coordination polymers and molecular structures among complexes of mercury(ii) halides with selected 1-benzoylthioureas," *Polyhedron*, vol. 90, pp. 47–57, 2015.

[157] B. L. Barnett, H. C. Kretschmar, and F. A. Hartman, "Structural characterization of bis(n-oxopyridine-2-thionato)zinc(iii)," *Inorganic Chemistry*, vol. 16, no. 8, pp. 1834–1838, 1977.

[158] J. Xue, A. Moyer, B. Peng, J. Wu, B. N. Hannafon, and W. Q. Ding, "Chloroquine is a zinc ionophore," *PLoS One*, vol. 9, no. 10, p. e109180, 2014.

[159] S. Abd-Elsalam, S. Soliman, E. S. Esmail, M. Khalaf, E. F. Mostafa, M. A. Medhat, O. A. Ahmed, M. S. A. El Ghafar, M. Alboraie, and S. M. Hassany, "Do zinc supplements enhance

the clinical efficacy of hydroxychloroquine?: a randomized, multicenter trial," *Biol Trace Elem Res*, pp. 1–5, 2020.

[160] A. Pormohammad, N. K. Monych, and R. J. Turner, "Zinc and sars-cov-2: A molecular modeling study of zn interactions with rna-dependent rna-polymerase and 3c-like proteinase enzymes," *International journal of molecular medicine*, vol. 47, no. 1, pp. 326–334, 2021.

[161] N. Verma, J. A. Henderson, and J. Shen, "Proton-coupled conformational activation of sars coronavirus main proteases and opportunity for designing small-molecule broad-spectrum targeted covalent inhibitors," *Journal of the American Chemical Society*, 2020.

[162] D. Chen, G. Menche, T. D. Power, L. Sower, J. W. Peterson, and C. H. Schein, "Accounting for ligand-bound metal ions in docking small molecules on adenylyl cyclase toxins," *Proteins*, vol. 67, no. 3, pp. 593–605, 2007.

[163] J. Karges, R. Stokes, and S. Cohen, "Metal complexes for therapeutic applications," *Trends in Chemistry*, vol. 3, 2021.

[164] R. Derwand and M. Scholz, "Does zinc supplementation enhance the clinical efficacy of chloroquine/hydroxychloroquine to win today's battle against covid-19?," *Med Hypotheses*, vol. 142, p. 109815, 2020.

[165] R. Bobat, H. Coovadia, C. Stephen, K. L. Naidoo, N. McKerrow, R. E. Black, and W. J. Moss, "Safety and efficacy of zinc supplementation for children with hiv-1 infection in south africa: a randomised double-blind placebo-controlled trial," *Lancet*, vol. 366, no. 9500, pp. 1862–7, 2005.

[166] C. Zoppi, L. Messori, and A. Pratesi, "Esi ms studies highlight the selective interaction of auranofin with protein free thiols," *Dalton Trans*, vol. 49, no. 18, pp. 5906–5913, 2020.

[167] D. Budhadev, E. Poole, I. Nehlmeier, Y. Liu, J. Hooper, E. Kalverda, U. S. Akshath, N. Hondow, W. B. Turnbull, S. Pöhlmann, Y. Guo, and D. Zhou, "Glycan-gold nanoparticles as multifunctional probes for multivalent lectin–carbohydrate binding: Implications for block-

ing virus infection and nanoparticle assembly," *Journal of the American Chemical Society*, 2020.

[168] P. Řezáčová, J. Pokorná, J. Brynda, M. Kožíšek, P. Cígler, M. Lepšík, J. Fanfrlík, J. Řezáč, K. Grantz Šašková, I. Sieglová, J. Plešek, V. Šícha, B. Grüner, H. Oberwinkler, J. Sedláček', H.-G. Kräusslich, P. Hobza, V. Král, and J. Konvalinka, "Design of hiv protease inhibitors based on inorganic polyhedral metallacarboranes," *Journal of Medicinal Chemistry*, vol. 52, no. 22, pp. 7132–7141, 2009.

[169] J. Mintz, A. Vedenko, O. Rosete, K. Shah, G. Goldstein, J. M. Hare, R. Ramasamy, and H. Arora, "Current advances of nitric oxide in cancer and anticancer therapeutics," *Vaccines (Basel)*, vol. 9, no. 2, 2021.

[170] A. F. Vanin, A. V. Pekshev, A. B. Vagapov, N. A. Sharapov, V. L. Lakomkin, A. A. Abramov, A. A. Timoshin, and V. I. Kapelko, "Gaseous nitric oxide and dinitrosyl iron complexes with thiol-containing ligands as potential medicines that can relieve covid-19," *Biophysics (Oxf)*, vol. 66, no. 1, pp. 155–163, 2021.

[171] A. F. Vanin, V. A. Tronov, and R. R. Borodulin, "Nitrosonium cation as a cytotoxic component of dinitrosyl iron complexes with thiol-containing ligands (based on the experimental work on mcf7 human breast cancer cell culture)," *Cell Biochem Biophys*, vol. 79, no. 1, pp. 93–102, 2021.

[172] R. Pulukkody and M. Y. Darensbourg, "Synthetic advances inspired by the bioactive dinitrosyl iron unit," *Acc Chem Res*, vol. 48, no. 7, pp. 2049–58, 2015.

[173] E. Cesareo, L. J. Parker, J. Z. Pedersen, M. Nuccetelli, A. P. Mazzetti, A. Pastore, G. Federici, A. M. Caccuri, G. Ricci, J. J. Adams, M. W. Parker, and M. Lo Bello, "Nitrosylation of human glutathione transferase p1-1 with dinitrosyl diglutathionyl iron complex in vitro and in vivo," *J Biol Chem*, vol. 280, no. 51, pp. 42172–80, 2005.

[174] D. C. Pectol, S. Khan, R. B. Chupik, M. Elsabahy, K. L. Wooley, M. Y. Darensbourg, and S. M. Lim, "Toward the optimization of dinitrosyl iron complexes as therapeutics for smooth

muscle cells," *Mol Pharm*, vol. 16, no. 7, pp. 3178–3187, 2019.

[175] D. C. Pectol, S. Khan, M. Elsabahy, K. L. Wooley, S.-M. Lim, and M. Y. Darensbourg, "Effects of glutathione and histidine on no release from a dimeric dinitrosyl iron complex (dnic)," *Inorganic Chemistry*, vol. 59, no. 23, pp. 16998–17008, 2020.

[176] X. Chen, Y. Hu, D. Wu, L. Weng, and B. Kang, "Syntheses and electrochemistry of some transition metal complexes with 2-mercaptopyridine n-oxide and crystal structure of bis(2-mercaptopyridine n-oxide)nickel(ii)," *Polyhedron*, vol. 10, no. 23, pp. 2651–2657, 1991.

[177] A. D. Bond, N. Feeder, S. J. Teat, and W. Jones, "Bis[1-hydroxypyridine-2(1h)-thionato-s,o]copper(ii)," *Acta Crystallogr C*, vol. 57, no. Pt 10, pp. 1157–8, 2001.

[178] J. Masuoka and P. Saltman, "Zinc(ii) and copper(ii) binding to serum albumin. a comparative study of dog, bovine, and human albumin," *J Biol Chem*, vol. 269, no. 41, pp. 25557–61, 1994.

[179] A. C. Leney and A. J. R. Heck, "Native mass spectrometry: What is in the name?," *Journal of the American Society for Mass Spectrometry*, vol. 28, no. 1, pp. 5–13, 2017.

[180] E. R. Schreiter, M. D. Sintchak, Y. Y. Guo, P. T. Chivers, R. T. Sauer, and C. L. Drennan, "Crystal structure of the nickel-responsive transcription factor nikr," *Nature Structural Biology*, vol. 10, no. 10, pp. 794–799, 2003.

[181] S. L. Bloom and D. B. Zamble, "Metal-selective dna-binding response of escherichia coli nikr," *Biochemistry*, vol. 43, no. 31, pp. 10029–10038, 2004.

[182] E. R. Schreiter, S. C. Wang, D. B. Zamble, and C. L. Drennan, "Nikr-operator complex structure and the mechanism of repressor activation by metal ions," *Proc Natl Acad Sci U S A*, vol. 103, no. 37, pp. 13676–81, 2006.

[183] A. L. West, S. E. Evans, J. M. Gonzalez, L. G. Carter, H. Tsuruta, E. Pozharski, and S. L. J. Michel, "Ni(ii) coordination to mixed sites modulates dna binding of hpnikr via a long-range effect," *Proceedings of the National Academy of Sciences of the United States of America*, vol. 109, no. 15, pp. 5633–5638, 2012.

[184] J. A. Denny and M. Y. Darensbourg, "Metallodithiolates as ligands in coordination, bioinorganic, and organometallic chemistry," *Chemical Reviews*, vol. 115, no. 11, pp. 5248–5273, 2015.

[185] K. N. Green, S. P. Jeffery, J. H. Reibenspies, and M. Y. Darensbourg, "A nickel tripeptide as a metallodithiolate ligand anchor for resin-bound organometallics," *Journal of the American Chemical Society*, vol. 128, no. 19, pp. 6493–6498, 2006.

[186] M. V. Rampersad, S. P. Jeffery, J. H. Reibenspies, C. G. Ortiz, D. J. Darensbourg, and M. Y. Darensbourg, "N2s2ni metallothiolates as a class of ligands that support organometallic and bioorganometallic reactivity," *Angewandte Chemie-International Edition*, vol. 44, no. 8, pp. 1217–1220, 2005.

[187] R. Breslow, "Biomimetic chemistry and artificial enzymes: Catalysis by design," *Accounts of Chemical Research*, vol. 28, no. 3, pp. 146–153, 1995.

[188] W.-D. Woggon, "From enzyme models to model enzymes. by anthonyj. kirby and florian hollfelder," *Angewandte Chemie International Edition*, vol. 49, no. 23, pp. 3867–3867, 2010.

[189] R. M. Jenkins, M. L. Singleton, L. A. Leamer, J. H. Reibenspies, and M. Y. Darensbourg, "Orientation and stereodynamic paths of planar monodentate ligands in square planar nickel n2s complexes," *Inorganic Chemistry*, vol. 49, no. 12, pp. 5503–5514, 2010.

[190] X. Yang, L. C. Elrod, T. Le, V. S. Vega, H. Naumann, Y. Rezenom, J. H. Reibenspies, M. B. Hall, and M. Y. Darensbourg, "Controlling o2 reactivity in synthetic analogues of [nifes]- and [nifese]-hydrogenase active sites," *Journal of the American Chemical Society*, vol. 141, no. 38, pp. 15338–15347, 2019.

[191] A. Volbeda, E. Garcin, C. Piras, A. L. de Lacey, V. M. Fernandez, E. C. Hatchikian, M. Frey, and J. C. Fontecilla-Camps, "Structure of the [nife] hydrogenase active site: evidence for biologically uncommon fe ligands," *Journal of the American Chemical Society*, vol. 118, no. 51, pp. 12989–12996, 1996.

[192] H. Ogata, P. Kellers, and W. Lubitz, "The crystal structure of the [nife] hydrogenase from the photosynthetic bacterium allochromatium vinosum: Characterization of the oxidized enzyme (ni-a state)," *Journal of Molecular Biology*, vol. 402, no. 2, pp. 428–444, 2010.

[193] A. Volbeda, P. Amara, C. Darnault, J.-M. Mouesca, A. Parkin, M. M. Roessler, F. A. Armstrong, and J. C. Fontecilla-Camps, "X-ray crystallographic and computational studies of the o2-tolerant [nife]-hydrogenase 1 from escherichia coli," *Proceedings of the National Academy of Sciences of the United States of America*, vol. 109, no. 14, pp. 5305–5310, 2012.

[194] M. Horch, L. Lauterbach, M. A. Mroginski, P. Hildebrandt, O. Lenz, and I. Zebger, "Reversible active site sulfoxygenation can explain the oxygen tolerance of a nad+-reducing [nife] hydrogenase and its unusual infrared spectroscopic properties," *Journal of the American Chemical Society*, vol. 137, no. 7, pp. 2555–2564, 2015.

[195] X. Yang, L. C. Elrod, J. H. Reibenspies, M. B. Hall, and M. Y. Darensbourg, "Oxygen uptake in complexes related to [nifes]- and [nifese]-hydrogenase active sites," *Chemical Science*, vol. 10, no. 5, pp. 1368–1373, 2019.

[196] P. J. Farmer, T. Solouki, D. K. Mills, T. Soma, D. H. Russell, J. H. Reibenspies, and M. Y. Darensbourg, "Isotopic labeling investigation of the oxygenation of nickel-bound thiolates by molecular oxygen," *Journal of the American Chemical Society*, vol. 114, no. 12, pp. 4601–4605, 1992.

[197] C. A. Grapperhaus and M. Y. Darensbourg, "Oxygen capture by sulfur in nickel thiolates," *Accounts of Chemical Research*, vol. 31, no. 8, pp. 451–459, 1998.

[198] E. Almaraz, J. A. Denny, W. S. Foley, J. H. Reibenspies, N. Bhuvanesh, and M. Y. Darensbourg, "Zinc/nickel exchange and ligand cannibalism in n2s2o1,2 donor ligand sets," *Dalton Transactions*, no. 43, pp. 9496–9502, 2009.

[199] J. A. Denny, W. S. Foley, A. D. Todd, and M. Y. Darensbourg, "The ligand unwrapping/rewrapping pathway that exchanges metals in s-acetylated, hexacoordinate n2s2o2

complexes," *Chemical Science*, vol. 6, no. 12, pp. 7079–7088, 2015.

[200] Y.-T. Chan, X. Li, J. Yu, G. A. Carri, C. N. Moorefield, G. R. Newkome, and C. Wesdemiotis, "Design, synthesis, and traveling wave ion mobility mass spectrometry characterization of iron(ii)– and ruthenium(ii)–terpyridine metallomacrocycles," *Journal of the American Chemical Society*, vol. 133, no. 31, pp. 11967–11976, 2011.

[201] P. Bonakdarzadeh, F. Topić, E. Kalenius, S. Bhowmik, S. Sato, M. Groessl, R. Knochenmuss, and K. Rissanen, "Dosy nmr, x-ray structural and ion-mobility mass spectrometric studies on electron-deficient and electron-rich m6l4 coordination cages," *Inorganic Chemistry*, vol. 54, no. 12, pp. 6055–6061, 2015.

[202] P. S. Pregosin, "Applications of nmr diffusion methods with emphasis on ion pairing in inorganic chemistry: a mini-review," *Magn Reson Chem*, vol. 55, no. 5, pp. 405–413, 2017.

[203] M. P. Crockett, H. Zhang, C. M. Thomas, and J. A. Byers, "Adding diffusion ordered nmr spectroscopy (dosy) to the arsenal for characterizing paramagnetic complexes," *Chemical Communications*, vol. 55, no. 96, pp. 14426–14429, 2019.

[204] C. Nardon, N. Pettenuzzo, and D. Fregona, "Gold complexes for therapeutic purposes: an updated patent review (2010-2015)," *Curr Med Chem*, vol. 23, no. 29, pp. 3374–3403, 2016.

[205] E. S. Baker, J. E. Bushnell, S. R. Wecksler, M. D. Lim, M. J. Manard, N. F. Dupuis, P. C. Ford, and M. T. Bowers, "Probing shapes of bichromophoric metalorganic complexes using ion mobility mass spectrometry," *Journal of the American Chemical Society*, vol. 127, no. 51, pp. 18222–18228, 2005.

APPENDIX A

NMR SPECTRA

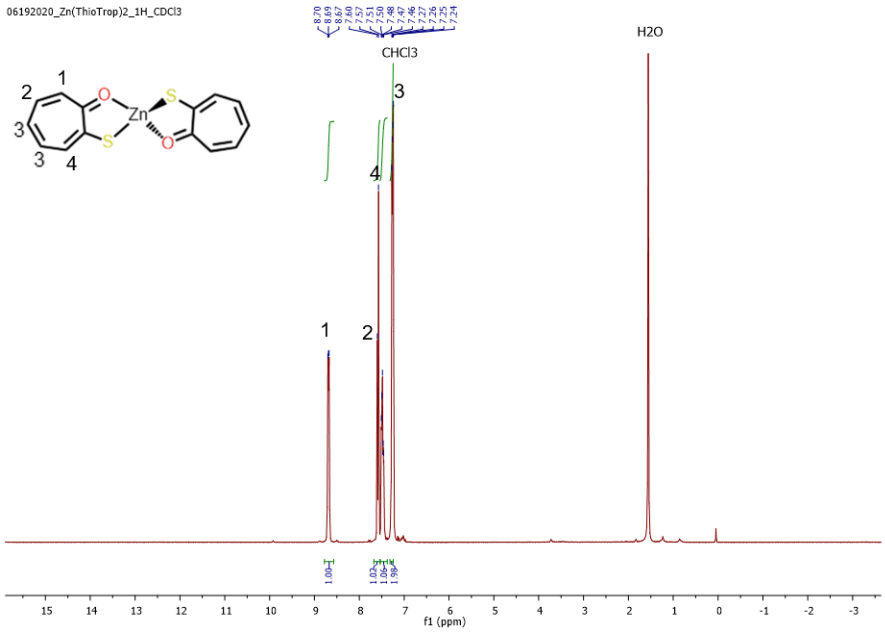

Figure A.1: ^{1}H NMR spectrum of Zn(**L1**)$_2$ in $CDCl_3$ using a 400MHz NMR spectrometer referenced to TMS via residual $CHCl_3$.

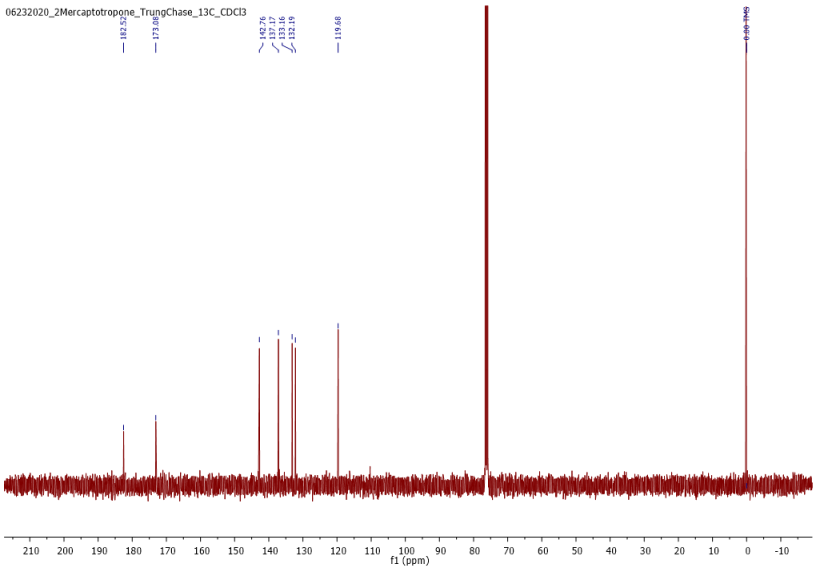

Figure A.2: ^{13}C NMR spectrum of Zn(**L1**)$_2$ in $CDCl_3$ using a 100MHz NMR spectrometer referenced to TMS.

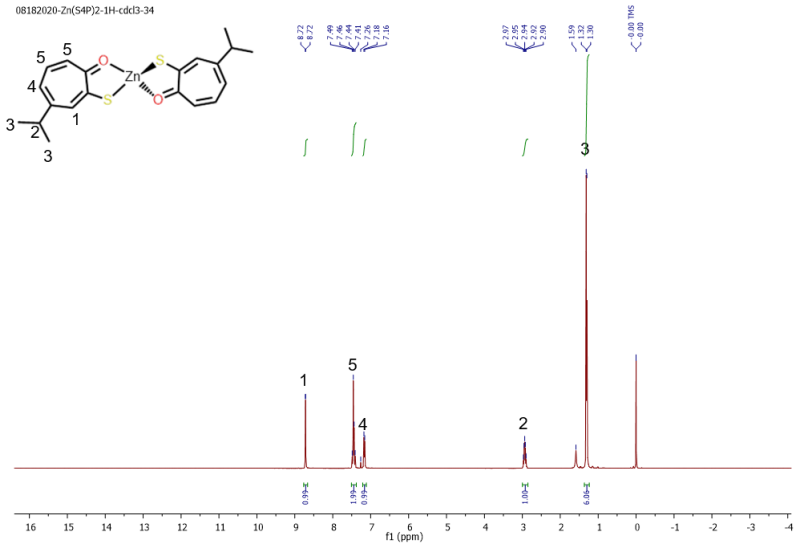

Figure A.3: ^{1}H NMR spectrum of Zn(**L2**)$_2$ in $CDCl_3$ using a 400MHz NMR spectrometer referenced to TMS.

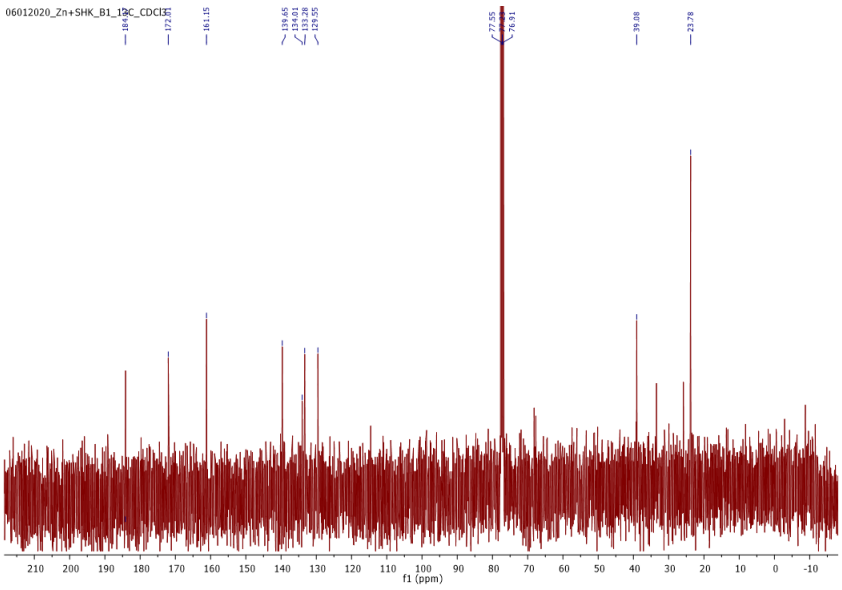

Figure A.4: ^{1}H NMR spectrum of Zn(**L2**)$_2$ in $CDCl_3$ using a 100MHz NMR spectrometer referenced to TMS.

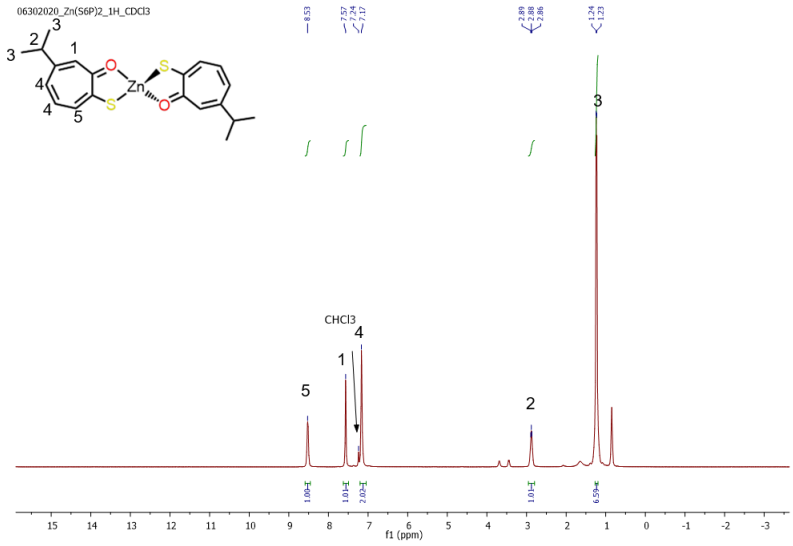

Figure A.5: ^{1}H NMR spectrum of Zn(**L3**)$_2$ in $CDCl_3$ using a 400MHz NMR spectrometer referenced to TMS via residual $CHCl_3$.

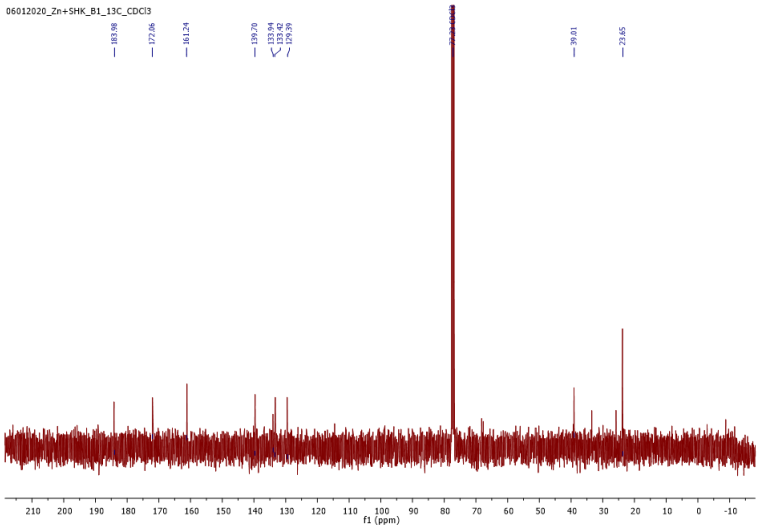

Figure A.6: ^{13}C NMR spectrum of Zn(**L3**)$_2$ in $CDCl_3$ using a 100MHz NMR spectrometer referenced to $CDCl_3$.

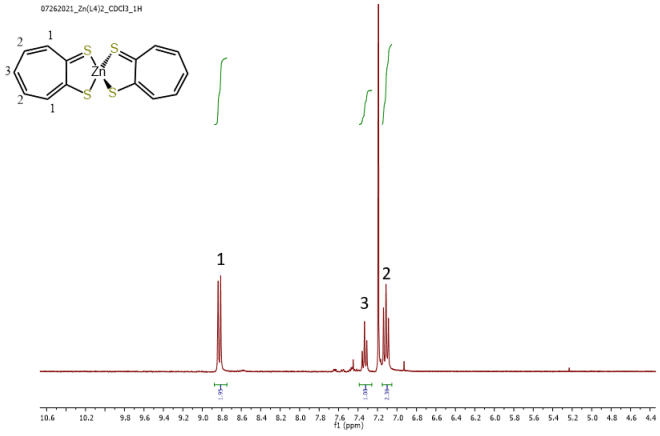

Figure A.7: ^{1}H NMR spectrum of Zn(**L4**)$_2$ in the aromatic region dissolved in $CDCl_3$ using a 400MHz NMR spectrometer referenced to $CHCl_3$.

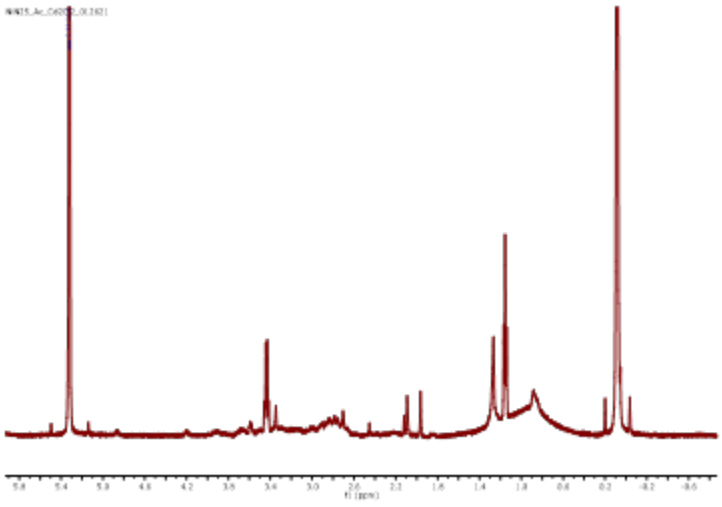

Figure A.8: ^{1}H NMR of [**Ni-I**]^{0} in CD_2Cl_2, referenced to residual DCM via TMS.

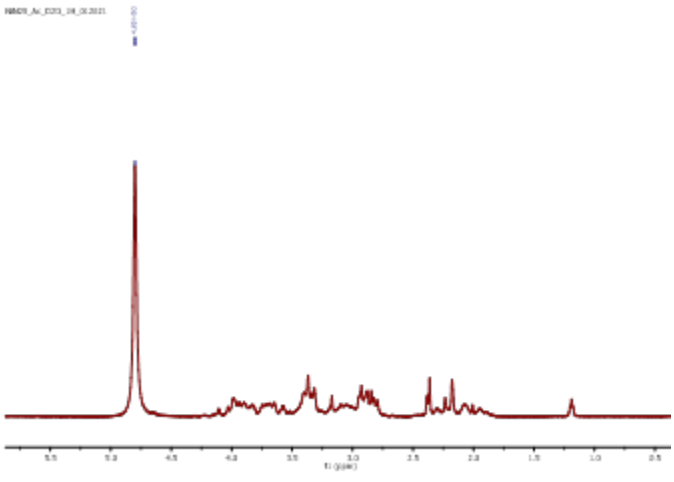

Figure A.9: ^{1}H NMR of [**Ni-I**]^{0} in D_2O, referenced to residual H_2O.

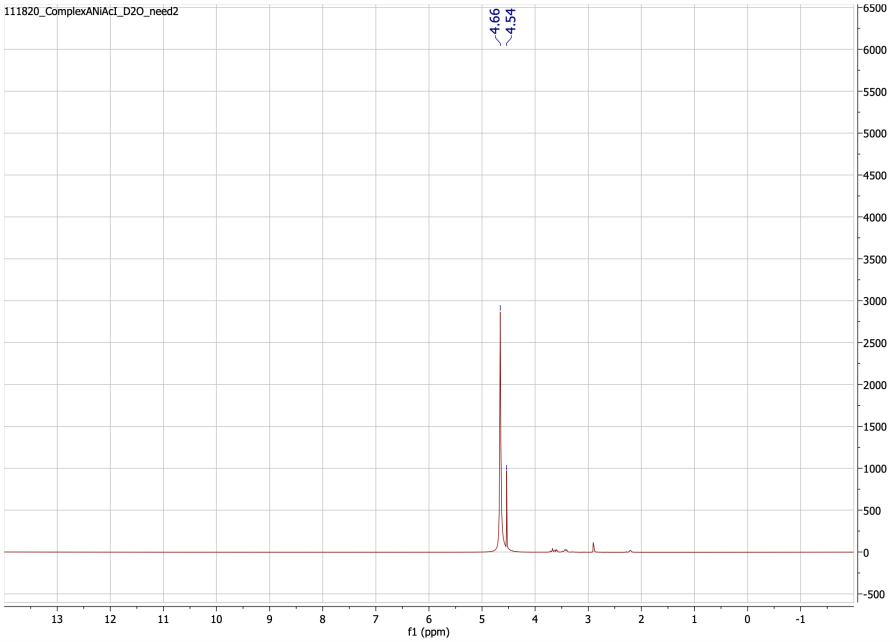

Figure A.10: ^{1}H-NMR Spectrum of [**Ni-I**]^{0} in D_2O (5% H_2O) with an inner capillary at 298 K using a 500 MHz NMR spectrometer under Ar.

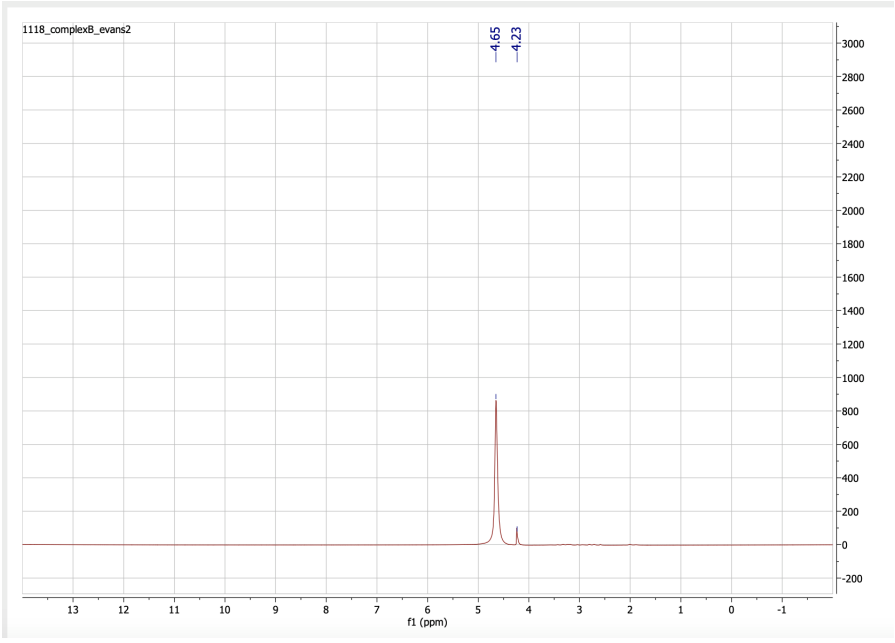

Figure A.11: ^{1}H-NMR Spectrum of [**Ni-Solv**]$^{+}$ in D_2O (5% H_2O) with an inner capillary at 298 K using a 500 MHz NMR spectrometer under Ar.

APPENDIX B

MASS SPECTRA

Mass Spectra

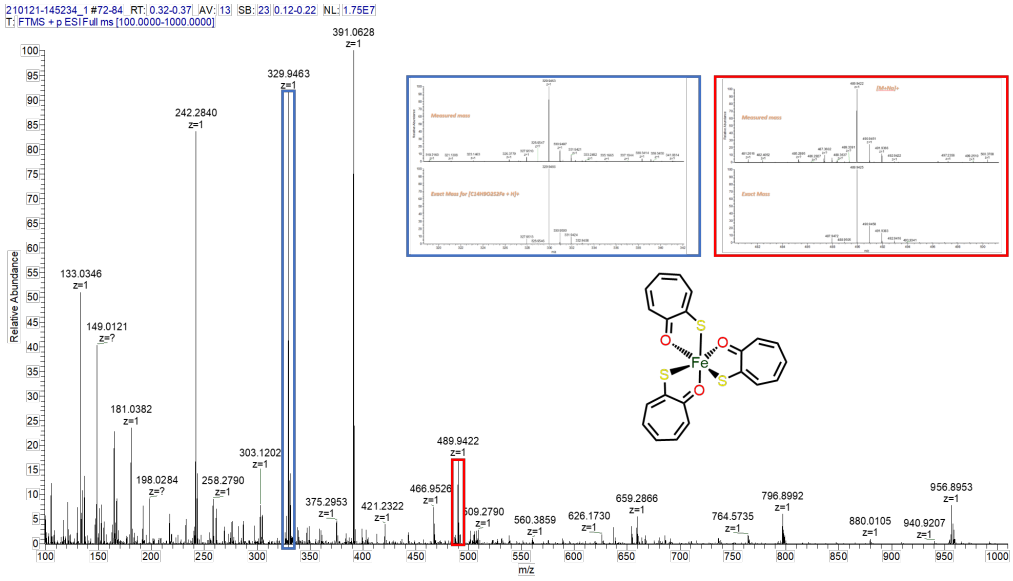

Figure B.1: High resolution $^{+}$ESI-MS of Fe(**L1**)$_3$ in DCM with isotopic bundles of interest ([M-L1]$^{+}$ 329.95) highlighted in blue and ([M+Na]$^{+}$ 489.94) highlighted in red.

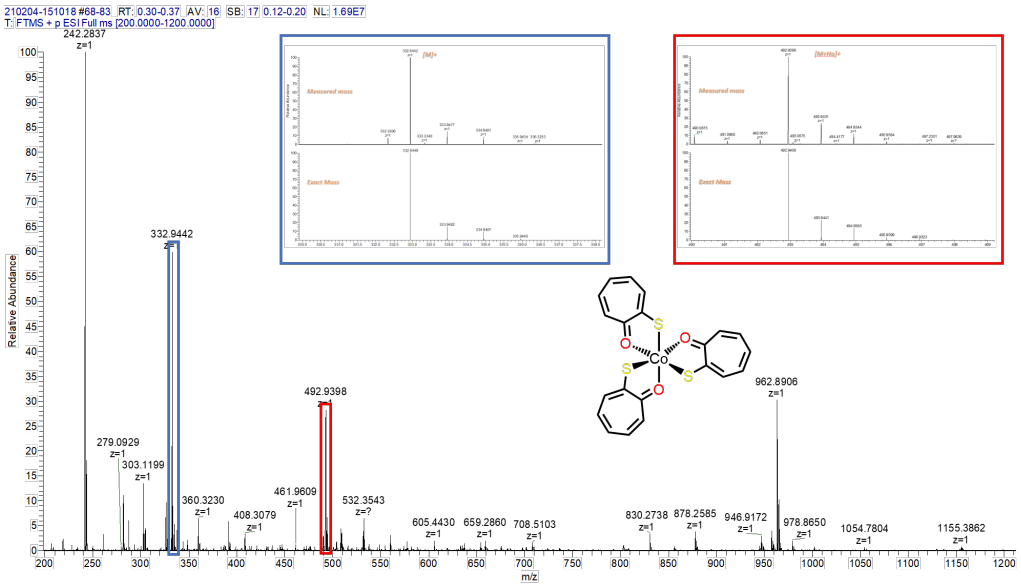

Figure B.2: High resolution $^{+}$ESI-MS of Co(**L1**)$_3$ in DCM with isotopic bundle of interest ([M-L1]$^{+}$ 332.94) highlighted in blue and ([M+Na]$^{+}$ 492.94) highlighted in red.

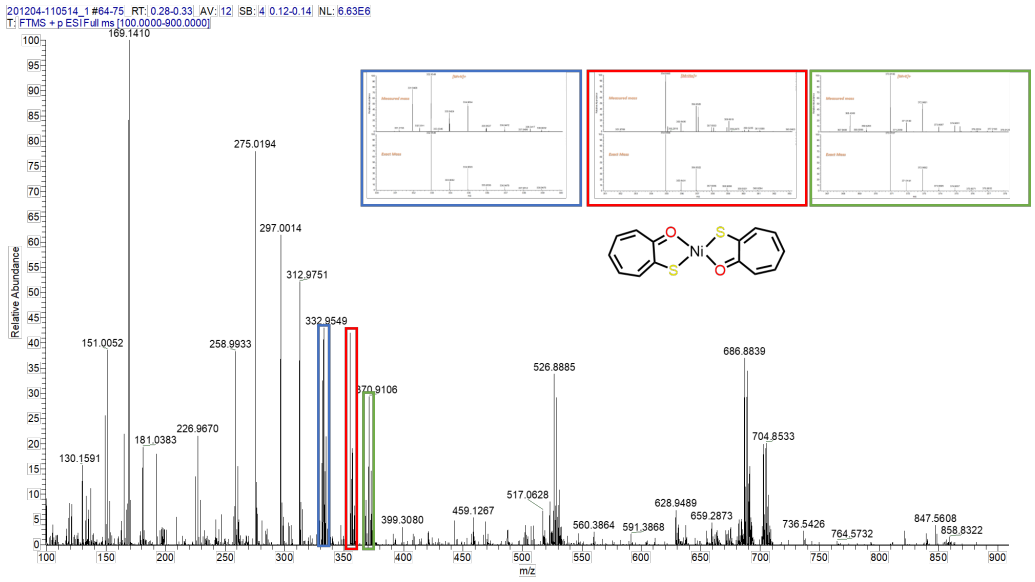

Figure B.3: High resolution $^{+}$ESI-MS of Ni(**L1**)$_2$ in DCM with isotopic bundles of interest highlighted ([M+H] $^{+}$ 332.95) (blue) ([M+Na]$^{+}$ 364.94)(red) and ([M+K]$^{+}$ 370.91) (green).

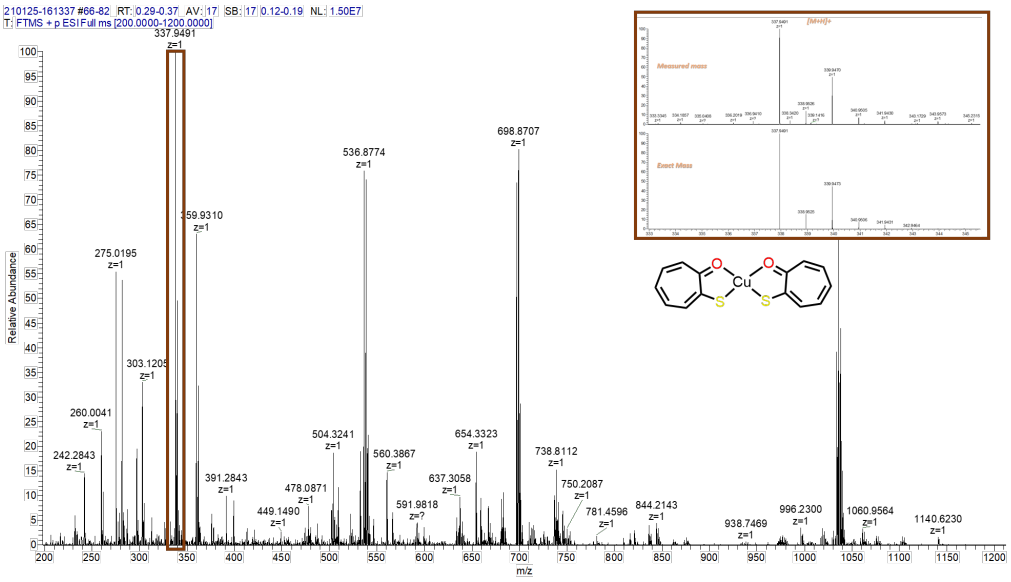

Figure B.4: High resolution $^{+}$ESI-MS of Cu(**L1**)$_2$ in DCM with isotopic bundle of interest ([M+H]$^{+}$ 337.95) highlighted in brown.

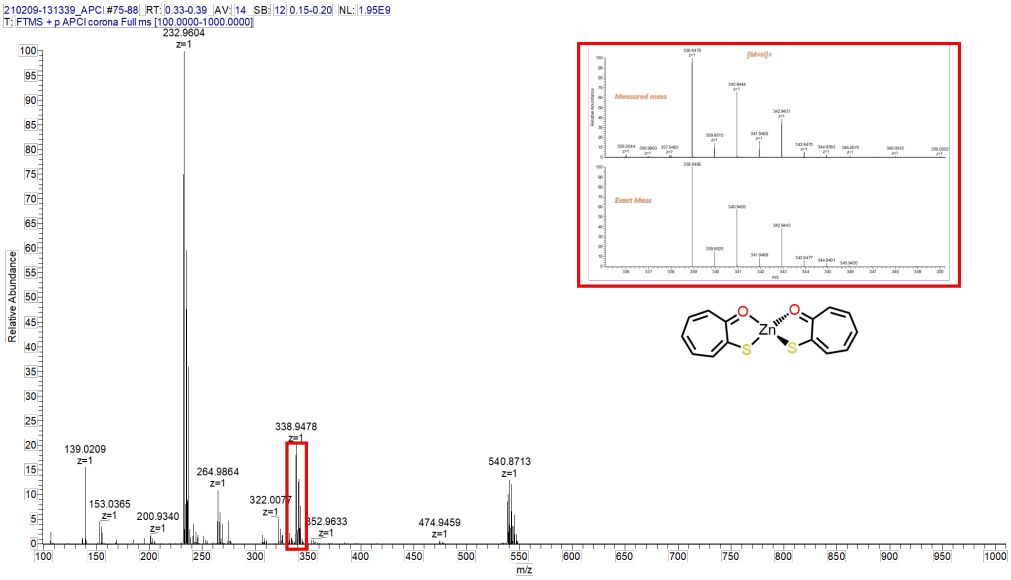

Figure B.5: High resolution $^{+}$APCI-MS of Zn(**L1**)$_2$ in DCM with isotopic bundle for the parent ion. (Calc. for [M+H]$^{+}$ 338.94).

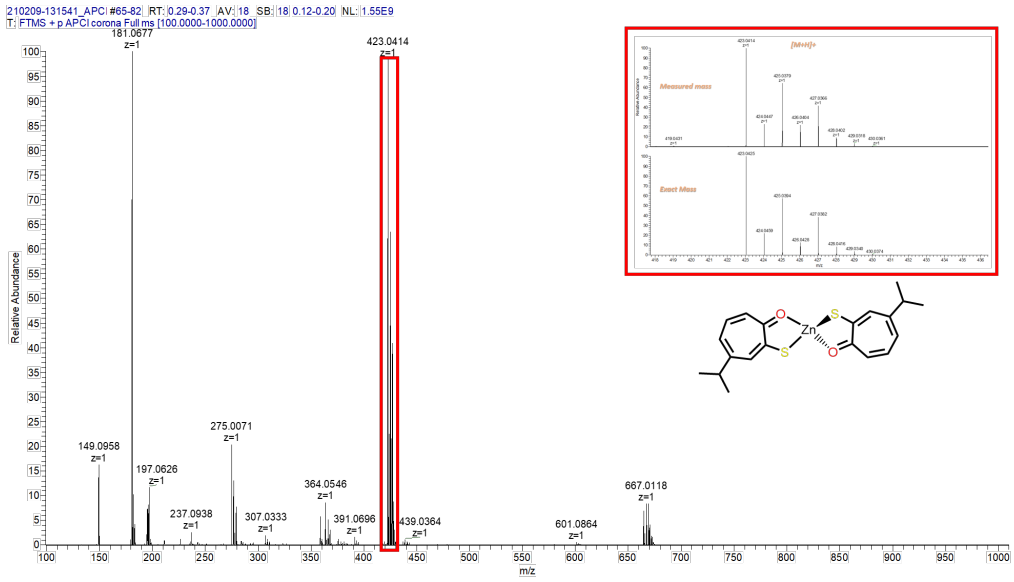

Figure B.6: High resolution $^{+}$APCI-MS of Zn(**L2**)$_2$ in DCM with isotopic bundle for the parent ion. (Calc. for $[M+H]^+$ 423.04).

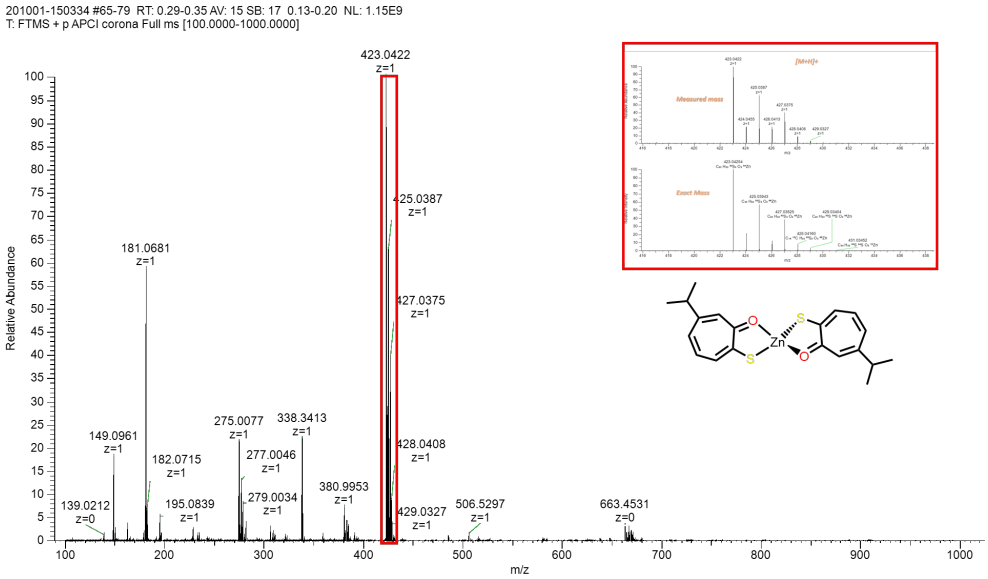

Figure B.7: High resolution $^{+}$APCI-MS of Zn(**L3**)$_2$ in DCM with isotopic bundle for the parent ion. (Calc. for $[M+H]^+$ 423.04).

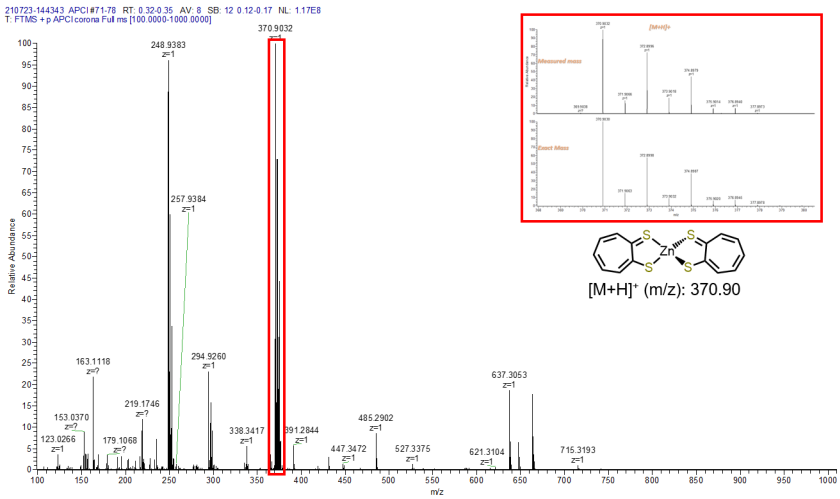

Figure B.8: High resolution $^{+}$APCI-MS of Zn(**L4**)$_2$ in DCM with isotopic bundle for the parent ion. (Calc. for [M+H]$^{+}$ 370.90).

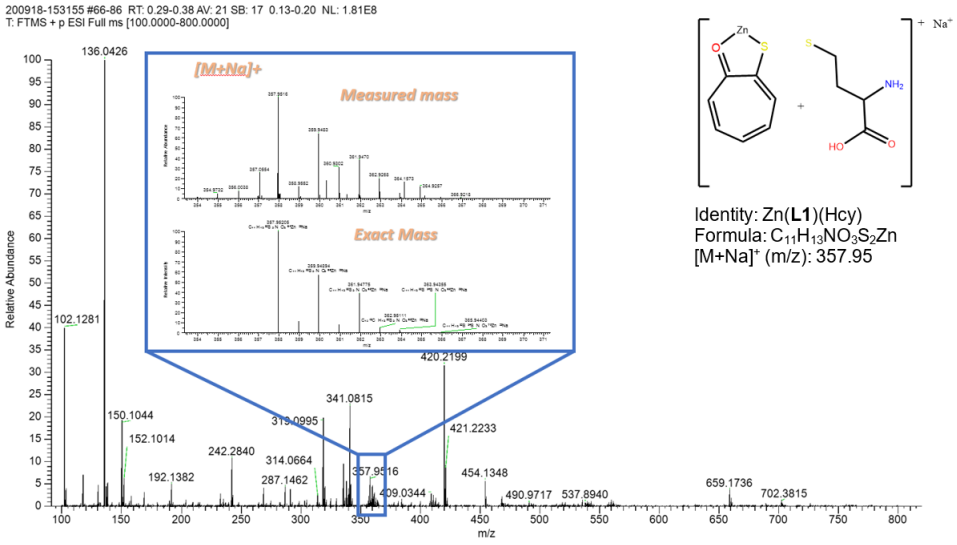

Figure B.9: High resolution $^{+}$ESI-MS of reaction of Zn(**L1**)$_2$ with D,L-Homocysteine. Isotopic bundle ([M+Na]$^{+}$ 357.95) of interest highlighted in blue.

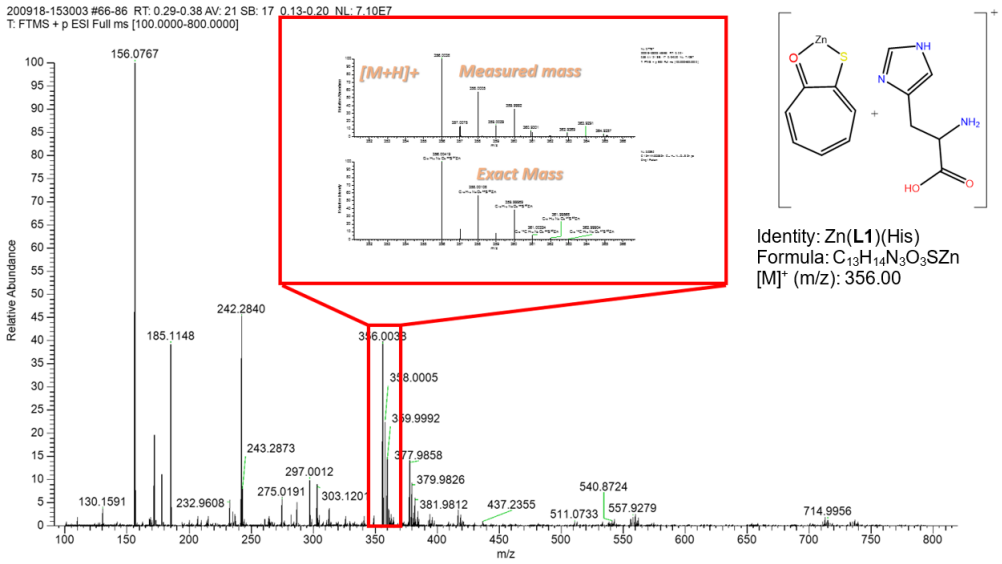

Figure B.10: High resolution $^{+}$ESI-MS of reaction of Zn(**L1**)$_2$ with L-Histidine. Isotopic bundle ([M+H]$^+$ 356.00) of interest highlighted in red.

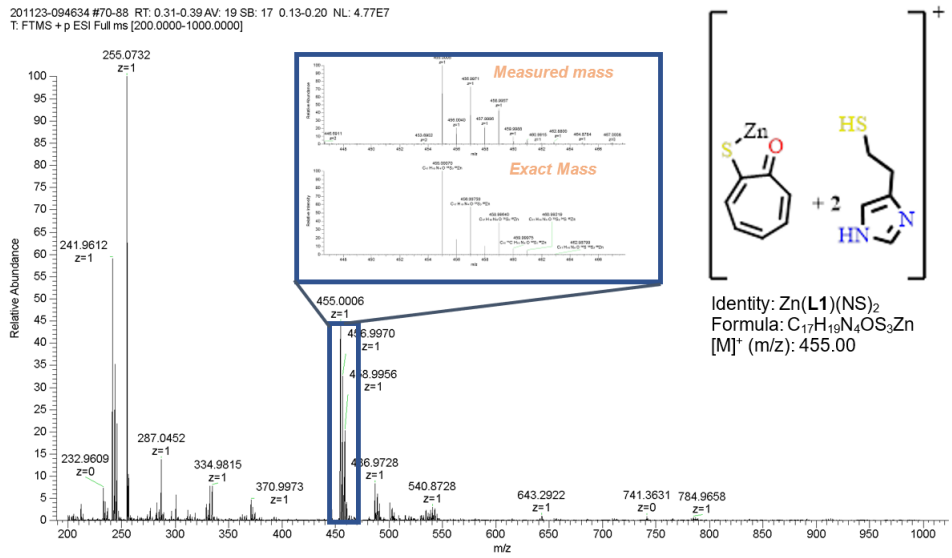

Figure B.11: High resolution $^{+}$ESI-MS of reaction of Zn(**L1**)$_2$ with proposed NS-mimic. Isotopic bundle ([M]$^+$ 455.00) of interest highlighted in blue

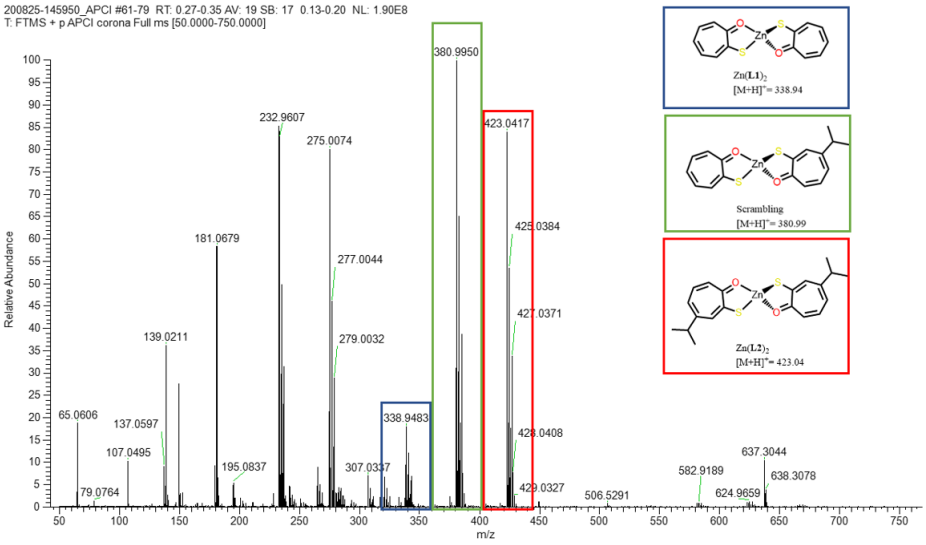

Figure B.12: High resolution $^{+}$APCI-MS the reaction of Zn(**L1**)$_2$ with Zn(**L2**)$_2$ in DCM with isotopic bundles of interest highlighted Zn(**L1**)$_2$ in blue (Calc. for [M+H]$^+$ 338.94), Zn(**L1**)(**L2**) in green (Calc. for [M+H]$^+$ 380.99), and Zn(**L2**)$_2$ in red (Calc. for [M+H]$^+$ 423.04).

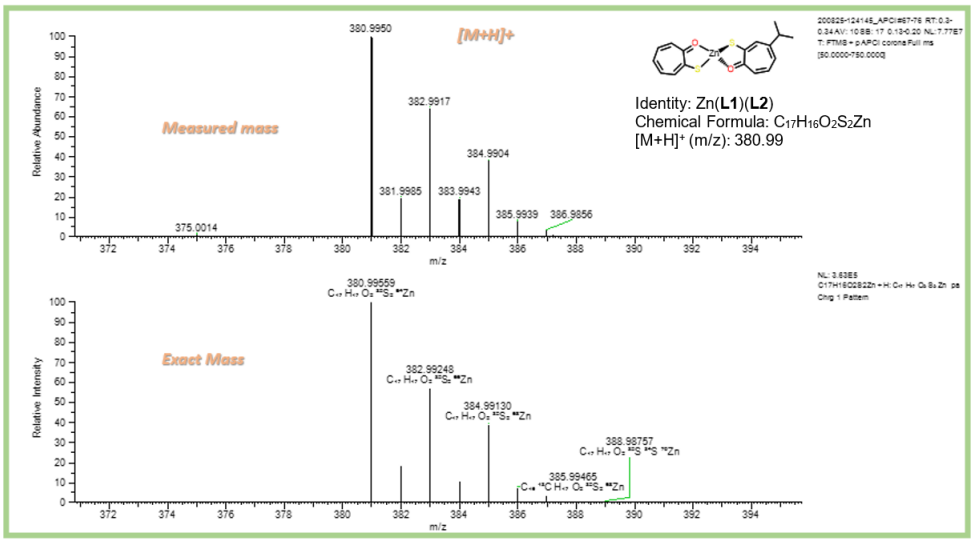

Figure B.13: Isotopic bundle of scrambling product Zn(**L1**)(**L2**) (Calc. for [M+H]$^+$ 380.99) from previous Figure (green box) enlarged for clarity.

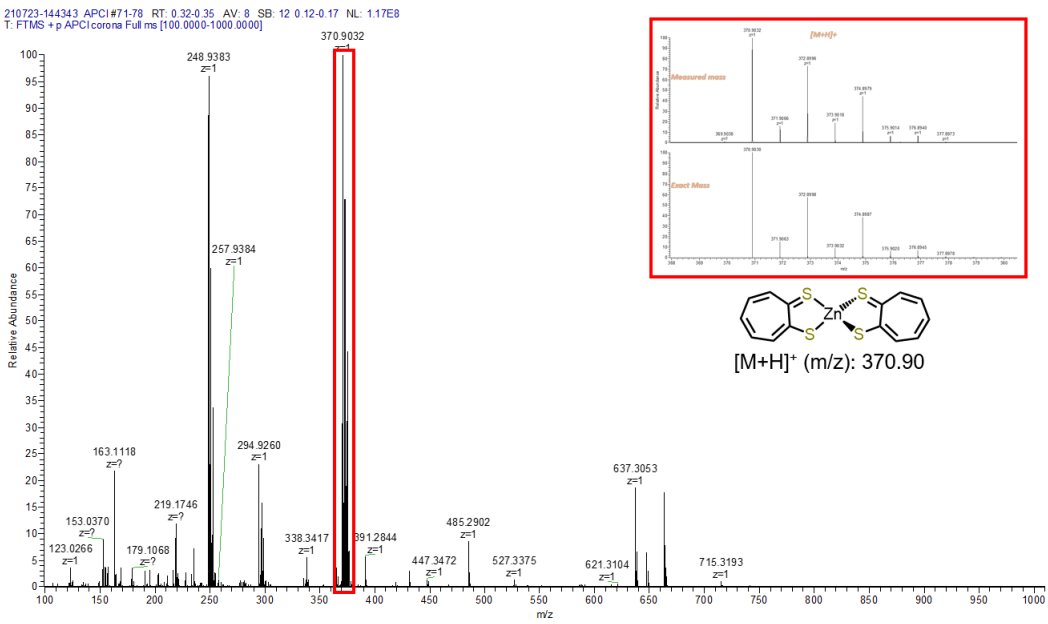

Figure B.14: High resolution $^{+}$ACPI-MS of Zn(**L4**)$_2$ in DCM with isotopic bundles of interest ([M+H]$^+$ 370.90) highlighted in highlighted in red.

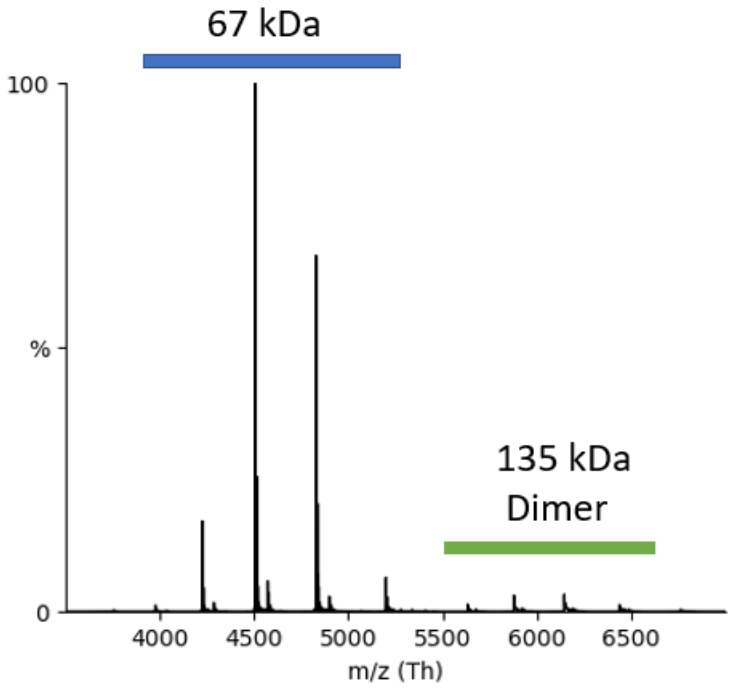

Figure B.15: Native MS of SC2M^{pro}, with isotopic bundle of monomeric (blue) and dimeric (green) SC2M^{pro} highlighted for clarity.

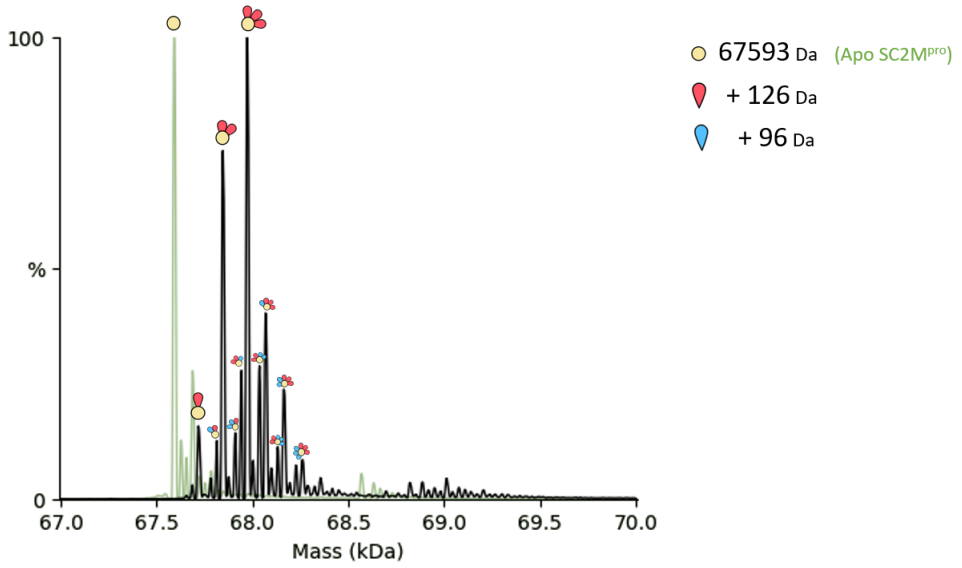

Figure B.16: Native MS of SC2M^{pro} (green) overlayed with that of the reaction product of SC2M^{pro} and Zn(PT)$_2$ (black). New mass shifts appearing upon reaction are indicated on the spectra with mass shifts given.

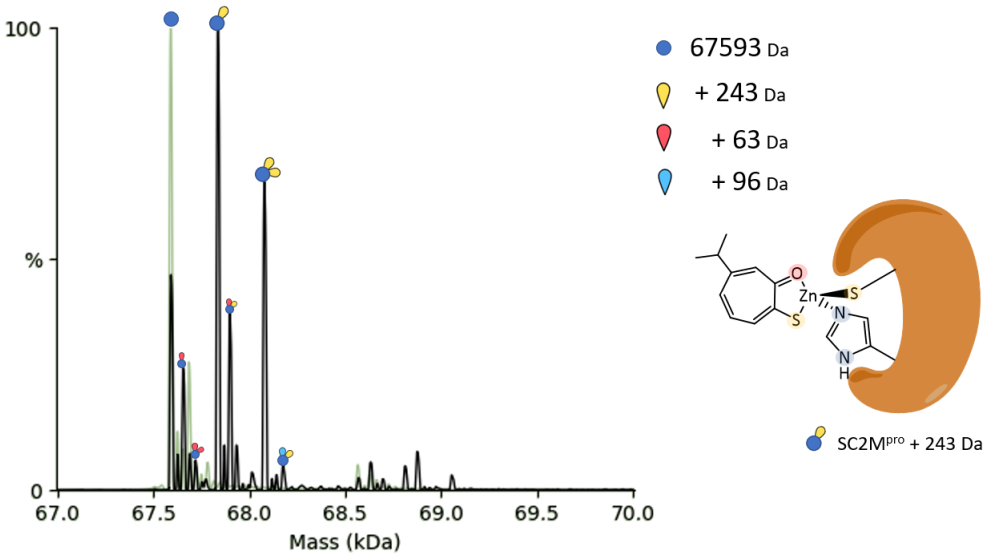

Figure B.17: Native MS of SC2M^{pro} (green) overlayed with that of the reaction product of SC2M^{pro} and Zn(**L2**)$_2$ (black). New mass shifts appearing upon reaction are indicated on the spectra with mass shifts given. A potential structure of the bound Zn(**L2**)$^+$ fragment is presented on the right.

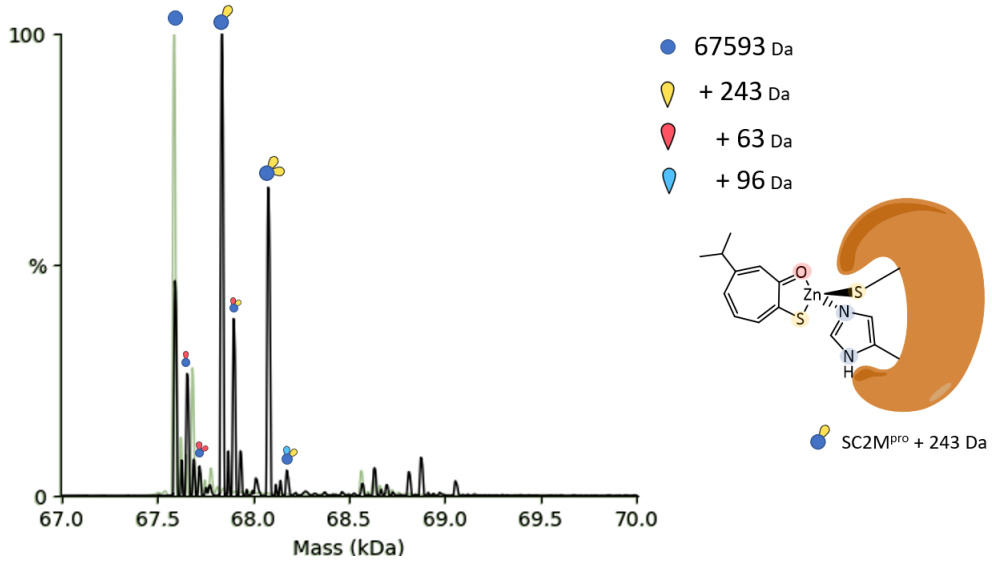

Figure B.18: Native MS of SC2M^{pro} (green) overlayed with that of the reaction product of SC2M^{pro} and Zn(**L3**)$_2$ (black). New mass shifts appearing upon reaction are indicated on the spectra with mass shifts given. A potential structure of the bound Zn(**L3**)$^+$ fragment is presented on the right.

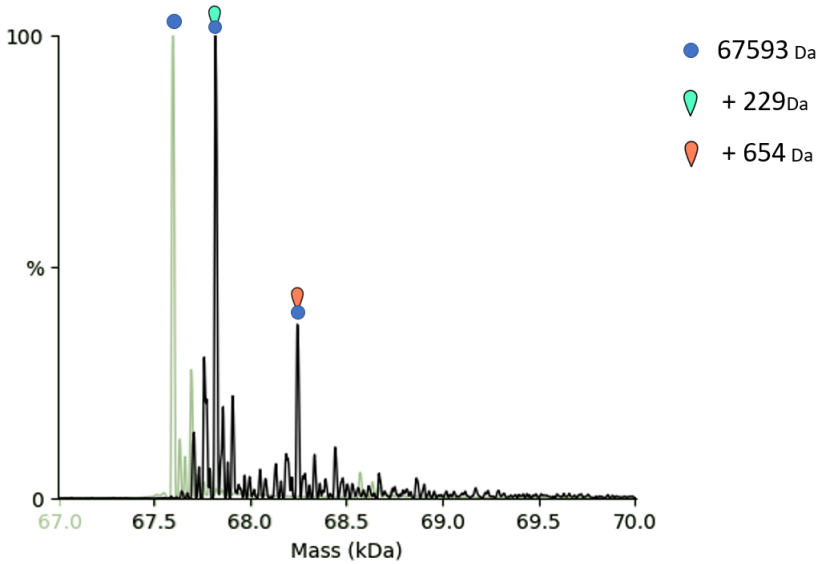

Figure B.19: Native MS of SC2M^{pro} (green) overlayed with that of the reaction product of SC2M^{pro} and TG-DNIC (black). New mass shifts appearing upon reaction are indicated on the spectra with mass shifts given.

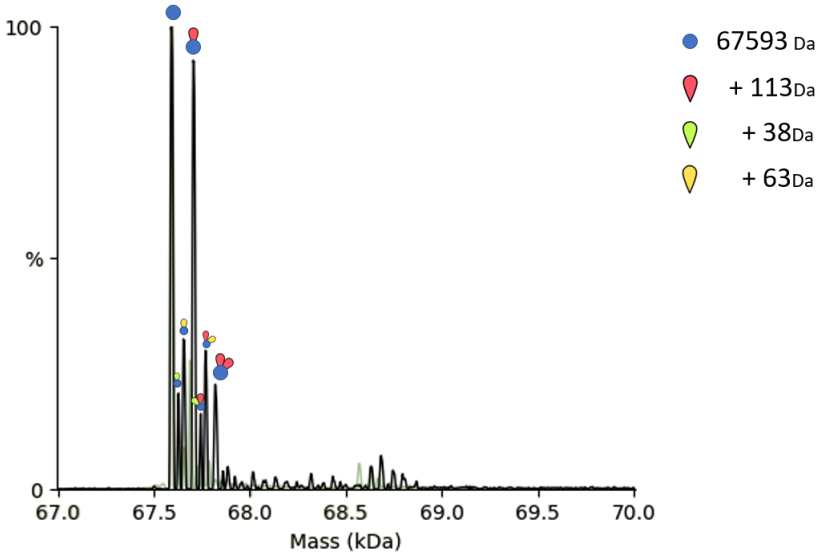

Figure B.20: Native MS of SC2M^{pro} (green) overlayed with that of the reaction product of SC2M^{pro} and TGTA-DNIC (black). New mass shifts appearing upon reaction are indicated on the spectra with mass shifts given.

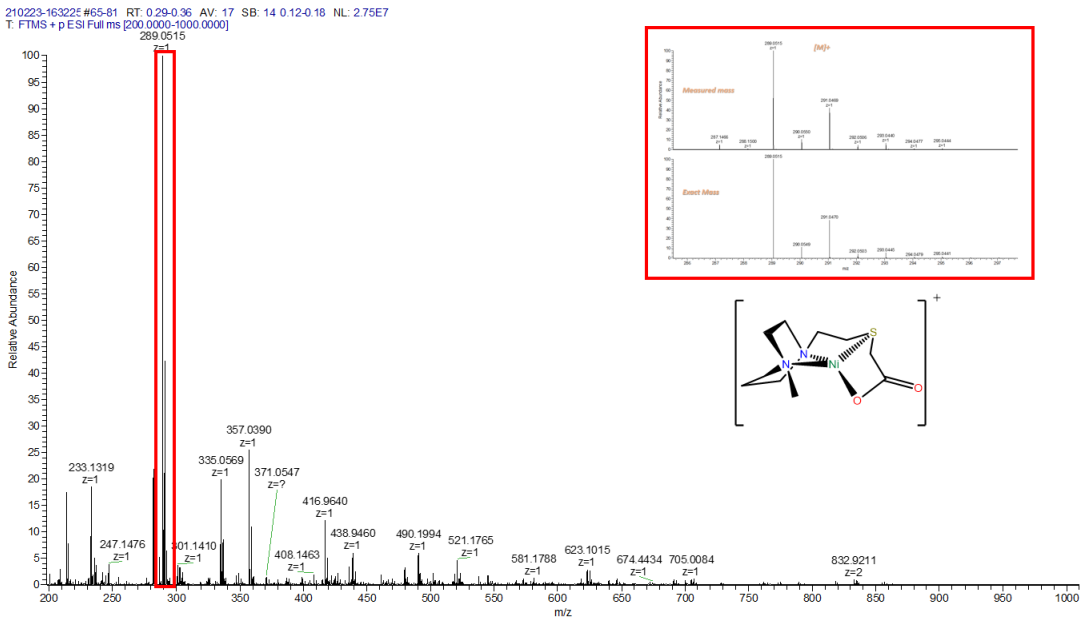

Figure B.21: High resolution $^{+}$ESI-MS of [**Ni-I**]^{0} in MeCN. Major peak [M-I]$^{+}$ is highlighted in red.

APPENDIX C

UV & IR SPECTRA

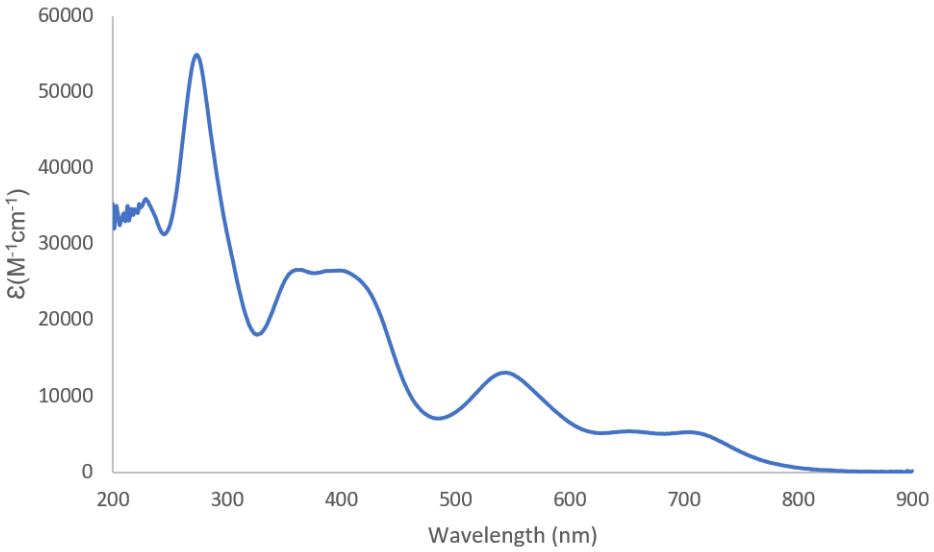

Figure C.1: UV-Vis spectra of Fe(**L1**)$_3$ in DCM.

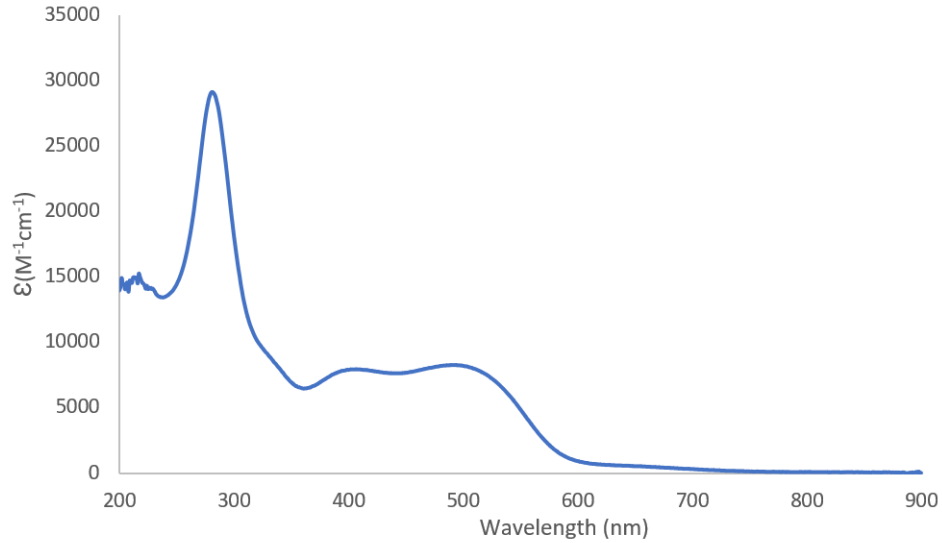

Figure C.2: UV-Vis spectra of Co(**L1**)$_3$ in DCM.

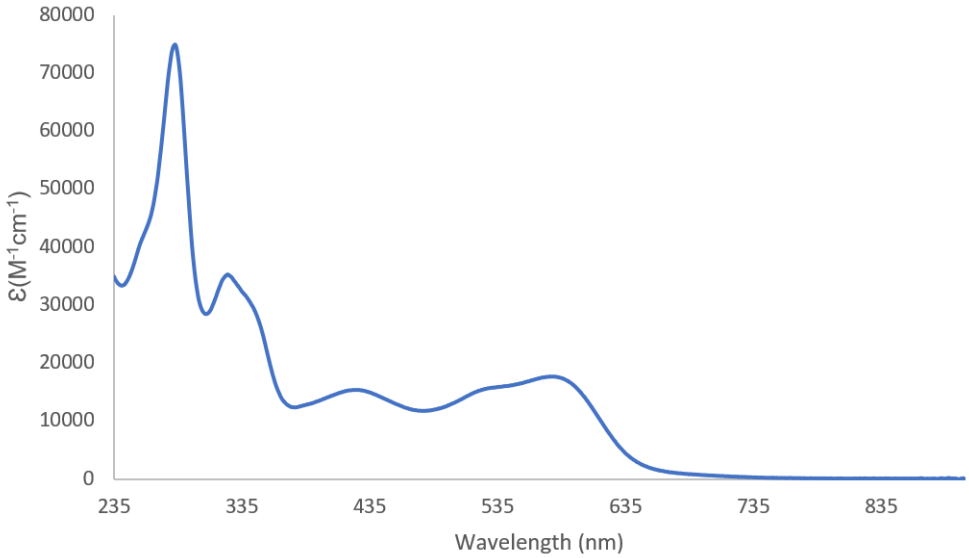

Figure C.3: UV-Vis spectra of Ni(**L1**)$_2$ in DCM.

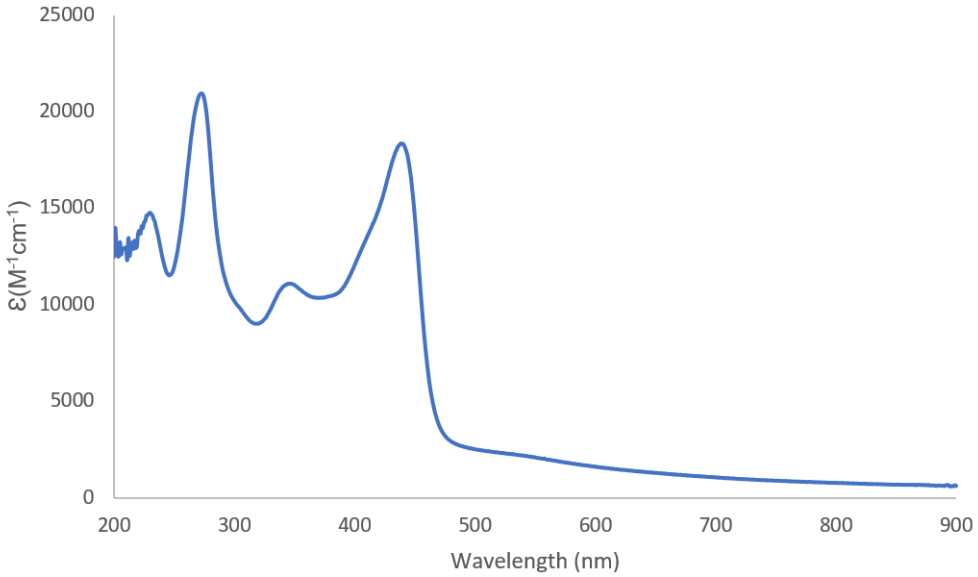

Figure C.4: UV-Vis spectra of Cu(**L1**)$_2$ in DCM.

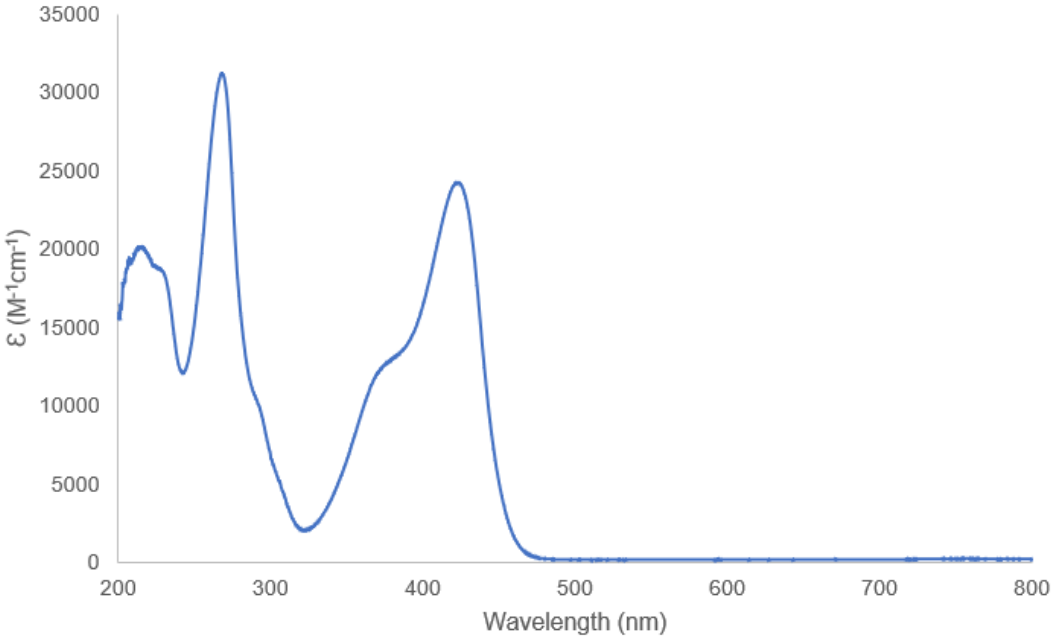

Figure C.5: UV-Vis spectra of Zn(**L1**)$_2$ in DCM.

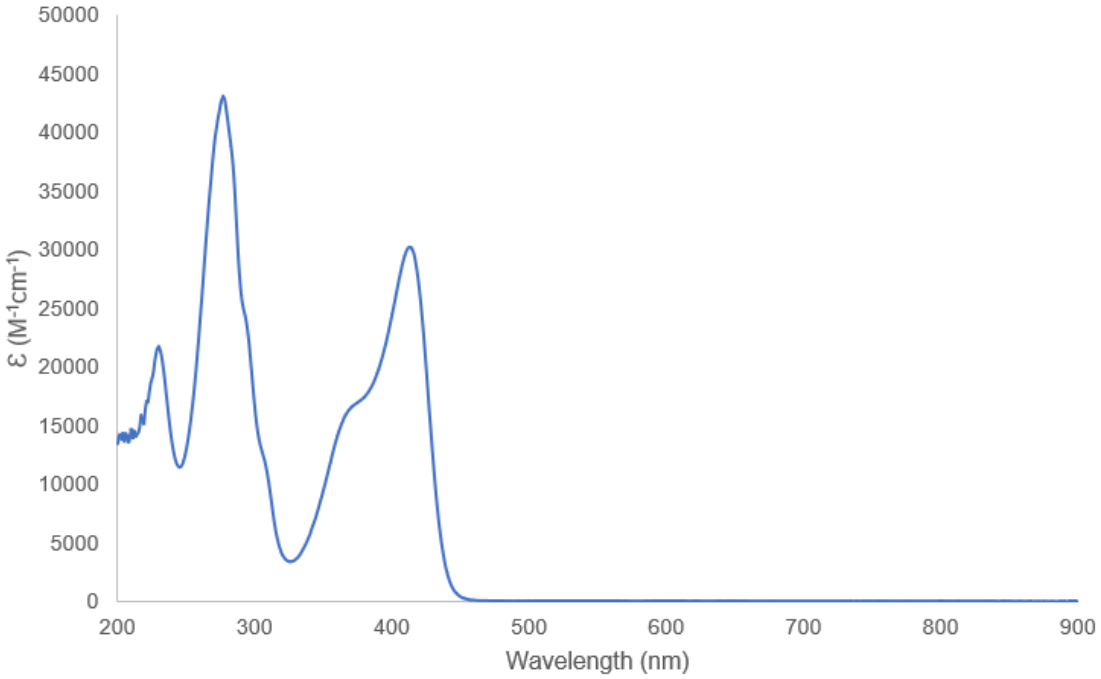

Figure C.6: UV-Vis spectra of Zn(**L2**)$_2$ in DCM.

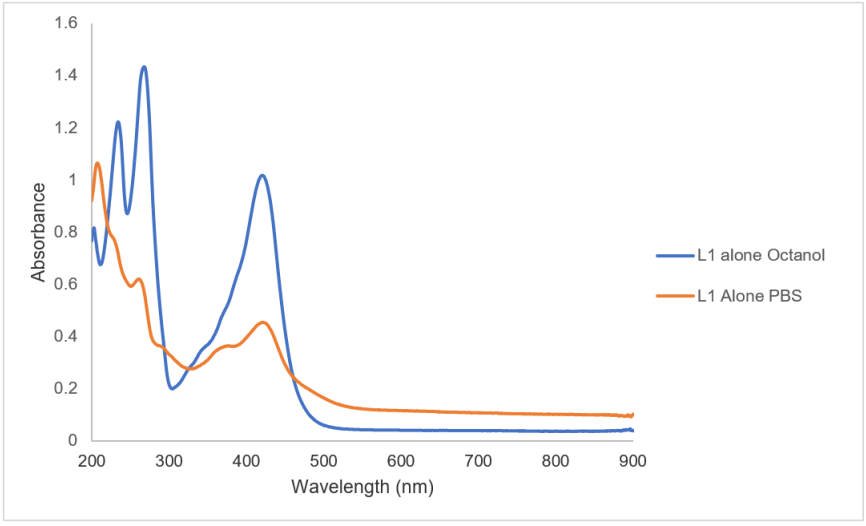

Figure C.7: Overlay of UV-Vis spectra of 1-octanol layer before (blue) and after (orange) partition experiment with **L1** alone.

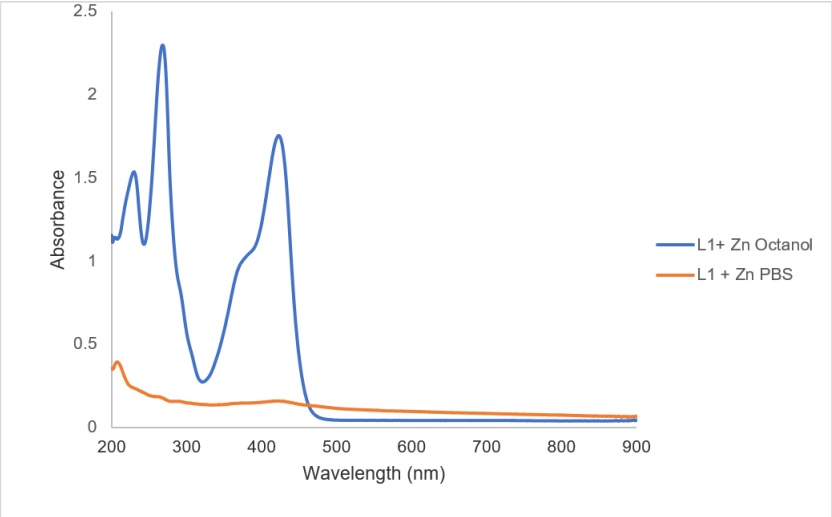

Figure C.8: Overlay of UV-Vis spectra of 1-octanol layer before (blue) and after (orange) partition experiment with **L1** + 0.5 $Zn(OAc)_2$.

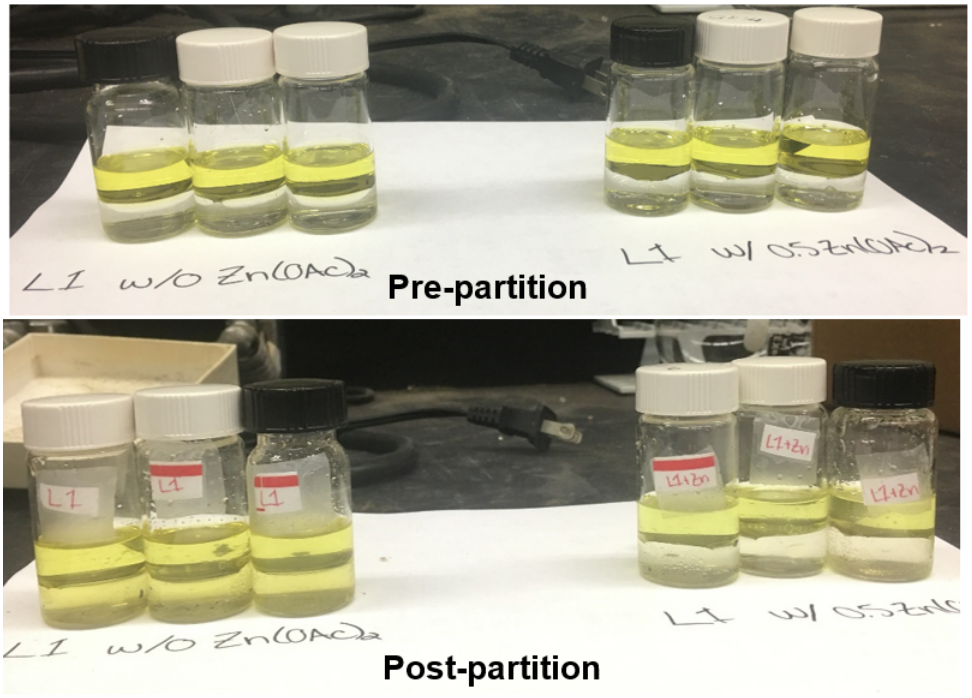

Figure C.9: Picture of the vials containing **L1** dissolved in 1-octanol before (top) and after (bottom) shaking for 1 hour followed by separation of the phases. Vials on the left were shaken with an equal volume of PBS pH = 7.4 while those on the right were shaken with PBS containing 0.5 eq. of $Zn(OAc)_2$.

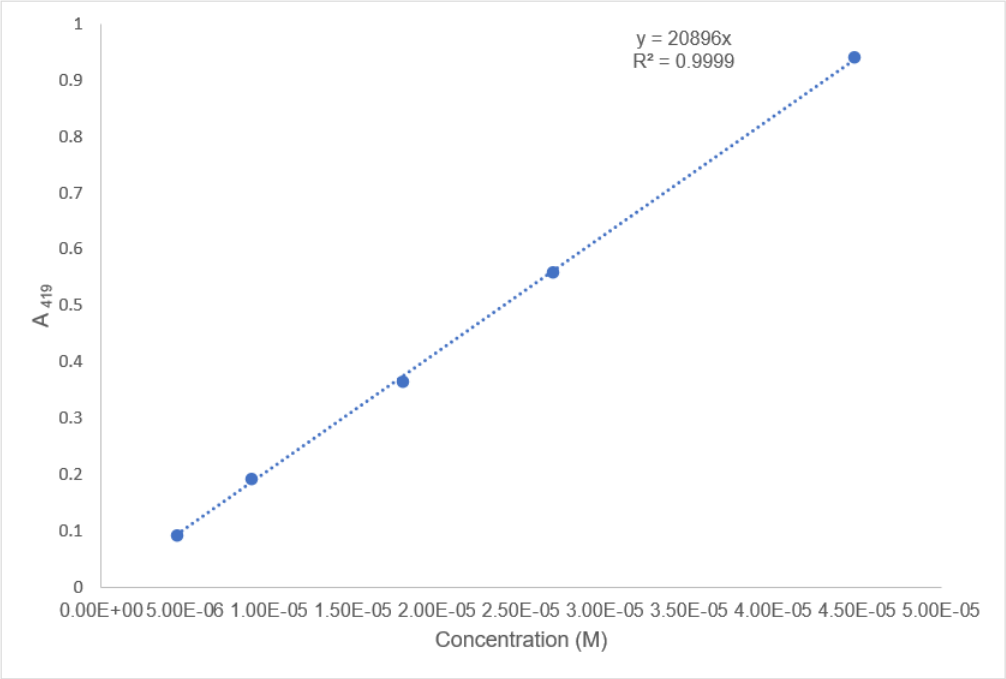

Figure C.10: Calibration curve of Zn($\mathbf{L1}_2$ in 1-octanol pre-equilibrated with phosophate buffered saline pH = 7.4 at 423 nm.

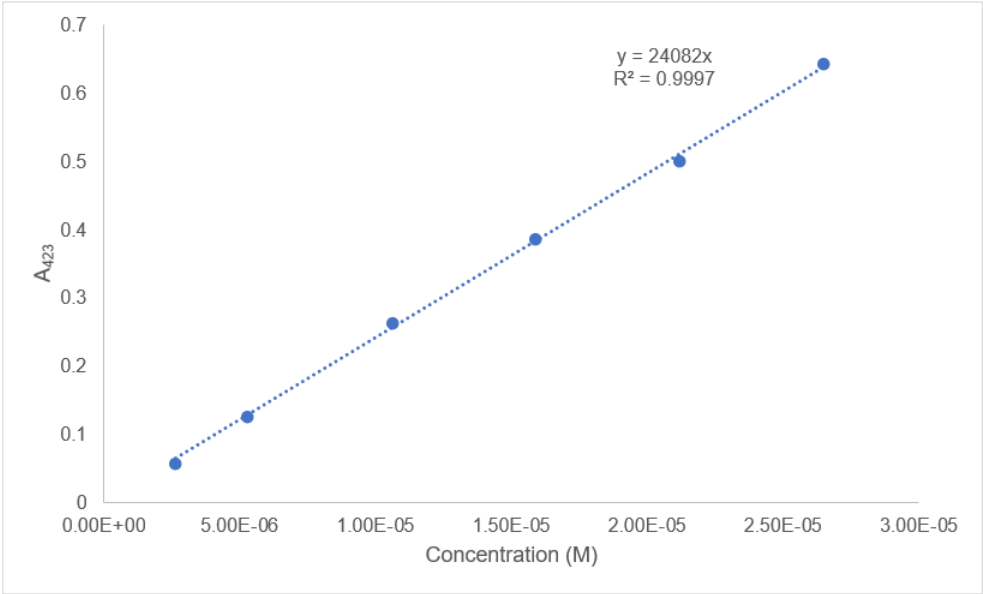

Figure C.11: Calibration curve of Zn($\mathbf{L2}_2$ in 1-octanol pre-equilibrated with phosophate buffered saline pH = 7.4 at 423 nm.

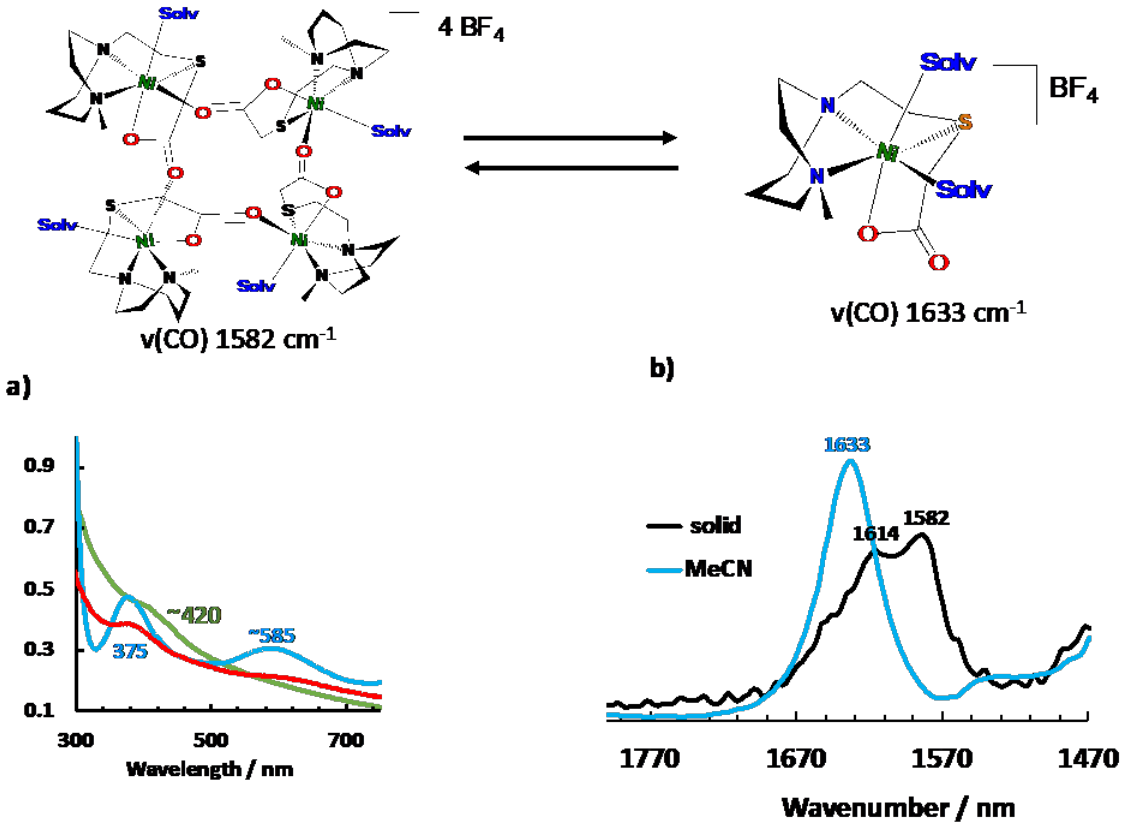

Figure C.12: The two forms of [**Ni-Solv**]$^+$; a) shows the vis-UV spectra of [**Ni-Solv**]$^+$ in different solvents; b) displays the IR spectra of [**Ni-Solv**]$_4{}^{4+}$ in solid and [**Ni-Solv**]$^+$ in MeCN solution within the 1600 cm^{-1} ν(C=O) range.

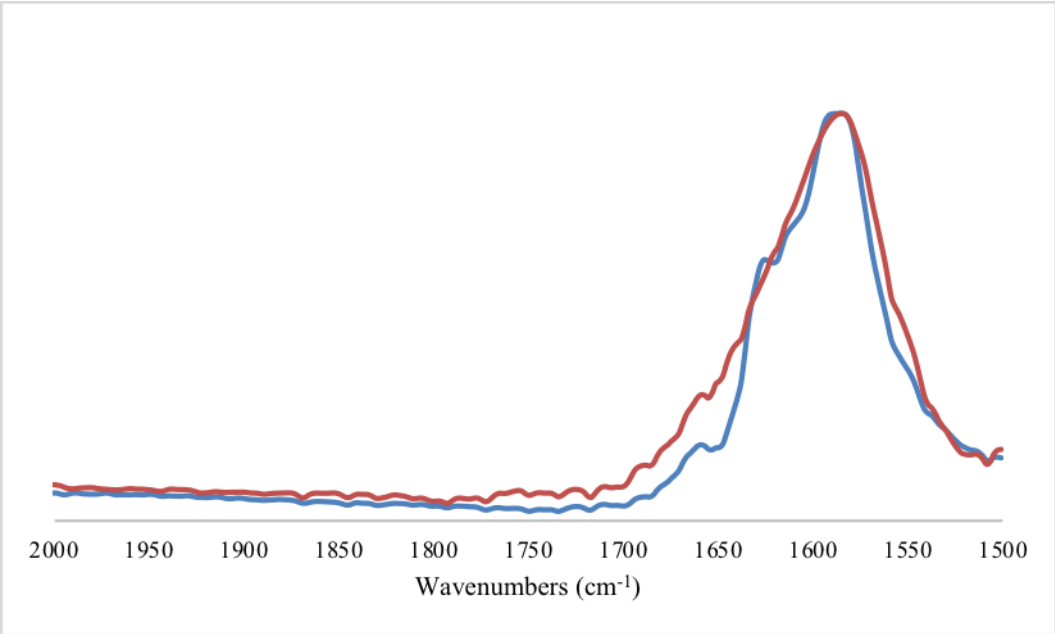

Figure C.13: ATR-IR in the ν(C=O) region of [**Ni-I**]$_4{}^0$ (red) and $NiN_2S'_2O_2$ (blue).

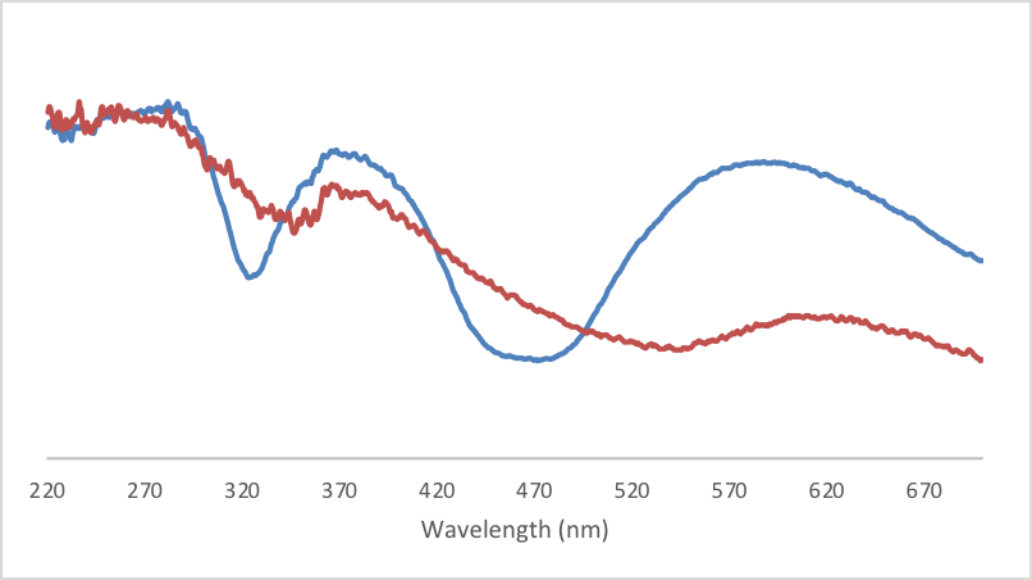

Figure C.14: Normalized Absorbance of solid-state UV-Vis of [**Ni-I**]$_4{}^0$ (red) and $NiN_2S_{/2}O_2$ (blue).

APPENDIX D

MOLECULAR STRUCTURES

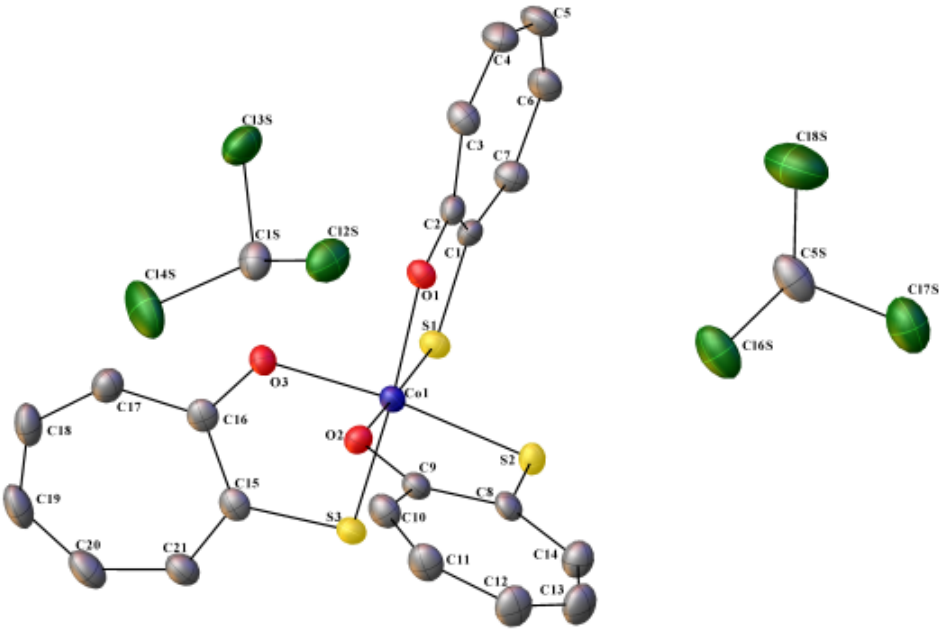

Figure D.1: Molecular structure of Co(**L1**)$_3$ co-crystallized with solvent molecule ($CDCl_3$) as determined by X-Ray Diffraction. H-atoms omitted for clarity.

Identification code	co3l1	
Empirical formula	C23 H17 Cl6 Co O3 S3	
Formula weight	709.17	
Temperature	110.0 K	
Wavelength	0.71073 Å	
Crystal system	Monoclinic	
Space group	P 1 21/n 1	
Unit cell dimensions	a = 15.8130(9) Å	α= 90°.
	b = 10.5298(5) Å	β= 100.594(2)°.
	c = 17.3447(9) Å	γ = 90°.
Volume	2838.8(3) $Å^3$	
Z	4	
Density (calculated)	1.659 Mg/m^3	
Absorption coefficient	1.416 mm^{-1}	
F(000)	1424	
Crystal size	0.352 x 0.146 x 0.016 mm^3	
Theta range for data collection	1.928 to 24.137°.	
Index ranges	-18<=h<=18, -12<=k<=12, -19<=l<=19	
Reflections collected	60602	
Independent reflections	4527 [R(int) = 0.0897]	
Completeness to theta = 24.137°	99.8 %	
Absorption correction	Semi-empirical from equivalents	
Max. and min. transmission	0.4166 and 0.3603	
Refinement method	Full-matrix least-squares on F^2	
Data / restraints / parameters	4527 / 0 / 325	
Goodness-of-fit on F^2	1.070	
Final R indices [I>2sigma(I)]	R1 = 0.0325, wR2 = 0.0678	
R indices (all data)	R1 = 0.0561, wR2 = 0.0809	
Extinction coefficient	n/a	
Largest diff. peak and hole	0.489 and -0.539 $e.Å^{-3}$	

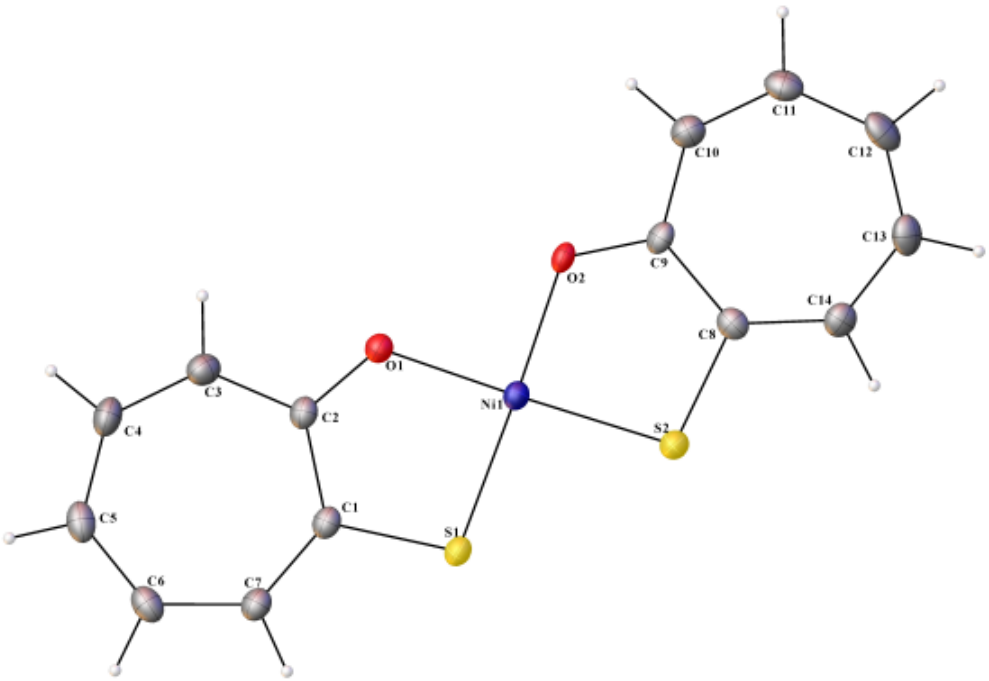

Figure D.2: Molecular Structure of of Ni(**L1**)$_2$ as determined by X-ray Diffraction.

Identification code	ni2l1a	
Empirical formula	C14 H10 Ni O2 S2	
Formula weight	333.05	
Temperature	110.0 K	
Wavelength	0.71073 Å	
Crystal system	Orthorhombic	
Space group	Pbca	
Unit cell dimensions	a = 7.3421(6) Å	α= 90°.
	b = 14.7591(11) Å	β= 90°.
	c = 23.5527(17) Å	γ = 90°.
Volume	2552.2(3) $Å^3$	
Z	8	
Density (calculated)	1.734 Mg/m^3	
Absorption coefficient	1.839 mm^{-1}	
F(000)	1360	
Crystal size	0.362 x 0.263 x 0.012 mm^3	
Theta range for data collection	2.893 to 27.653°.	
Index ranges	-9<=h<=9, -19<=k<=19, -30<=l<=30	
Reflections collected	38539	
Independent reflections	2963 [R(int) = 0.0584]	
Completeness to theta = 25.242°	99.8 %	
Absorption correction	Semi-empirical from equivalents	
Max. and min. transmission	0.4305 and 0.3113	
Refinement method	Full-matrix least-squares on F^2	
Data / restraints / parameters	2963 / 0 / 172	
Goodness-of-fit on F^2	1.086	
Final R indices [I>2sigma(I)]	R1 = 0.0439, wR2 = 0.1014	
R indices (all data)	R1 = 0.0476, wR2 = 0.1032	
Extinction coefficient	n/a	
Largest diff. peak and hole	0.662 and -0.647 $e.Å^{-3}$	

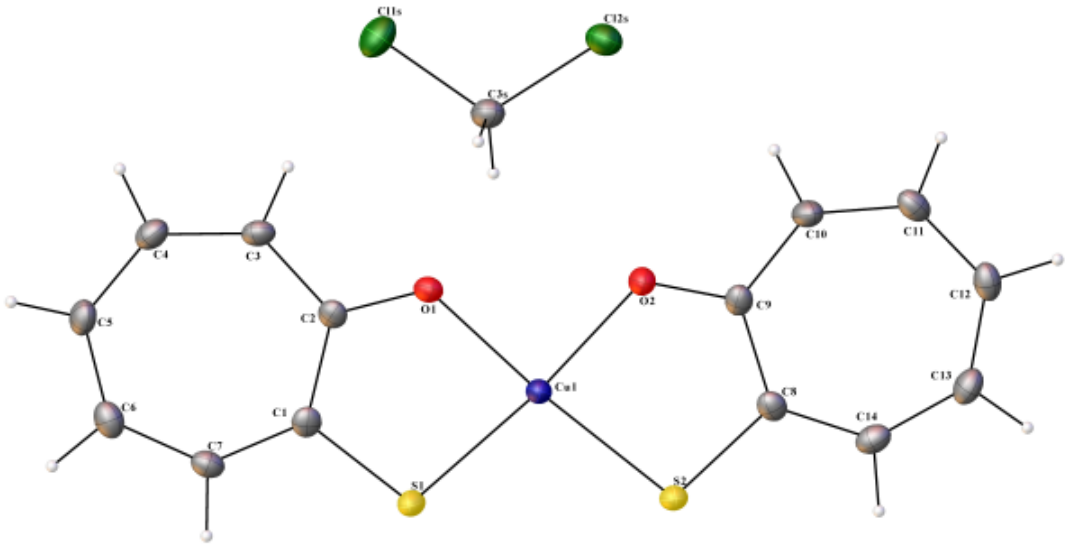

Figure D.3: Molecular structure of Cu(**L1**)$_2$ co-crystallized with solvent molecule (DCM) as determined by X-ray Diffraction.

Identification code	cul1	
Empirical formula	C15 H12 Cl2 Cu O2 S2	
Formula weight	422.81	
Temperature	110.0 K	
Wavelength	1.54178 Å	
Crystal system	Monoclinic	
Space group	P 1 21/n 1	
Unit cell dimensions	a = 3.9287(4) Å	α= 90°.
	b = 27.902(3) Å	β= 92.513(7)°
	c = 14.6962(16) Å	γ = 90°.
Volume	1609.5(3) $Å^3$	
Z	4	
Density (calculated)	1.745 Mg/m^3	
Absorption coefficient	7.420 mm^{-1}	
F(000)	852	
Crystal size	0.217 x 0.024 x 0.018 mm^3	
Theta range for data collection	3.168 to 70.114°.	
Index ranges	-4<=h<=4, -33<=k<=33, -17<=l<=17	
Reflections collected	22336	
Independent reflections	3045 [R(int) = 0.0398]	
Completeness to theta = 67.679°	99.9 %	
Absorption correction	Semi-empirical from equivalents	
Max. and min. transmission	0.4684 and 0.2204	
Refinement method	Full-matrix least-squares on F^2	
Data / restraints / parameters	3045 / 0 / 199	
Goodness-of-fit on F^2	1.101	
Final R indices [I>2sigma(I)]	R1 = 0.0259, wR2 = 0.0664	
R indices (all data)	R1 = 0.0269, wR2 = 0.0670	
Extinction coefficient	n/a	
Largest diff. peak and hole	0.371 and -0.302 $Å^{-3}$	

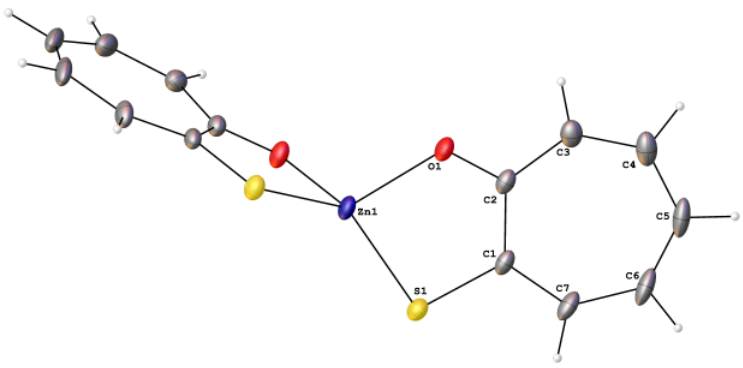

Figure D.4: Molecular structure of Zn(**L1**)$_2$ as determined by X-Ray Diffraction.

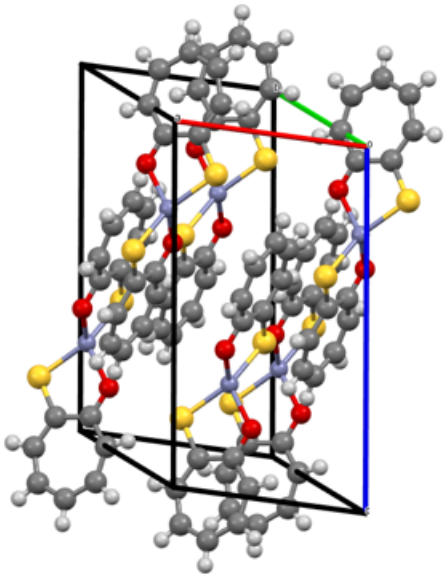

Figure D.5: Crystal packing of Zn(**L1**)$_2$ as determined by X-Ray Diffraction. Image generated using Mercury.

Identification code	zn2merc	
Empirical formula	C14 H10 O2 S2 Zn	
Formula weight	339.71	
Temperature	110.0 K	
Wavelength	0.71073 Å	
Crystal system	Monoclinic	
Space group	C 1 2/c 1	
Unit cell dimensions	a = 7.5612(6) Å	α= 90°.
	b = 12.5681(10) Å	β= 100.036(3)°.
	c = 13.8362(11) Å	γ = 90°.
Volume	1294.73(18) $Å^3$	
Z	4	
Density (calculated)	1.743 Mg/m^3	
Absorption coefficient	2.211 mm^{-1}	
F(000)	688	
Crystal size	0.507 x 0.342 x 0.206 mm^3	
Theta range for data collection	2.990 to 33.106°.	
Index ranges	-11<=h<=11, -19<=k<=19, -21<=l<=21	
Reflections collected	22216	
Independent reflections	2400 [R(int) = 0.0491]	
Completeness to theta = 25.242°	99.4 %	
Absorption correction	Semi-empirical from equivalents	
Max. and min. transmission	0.3399 and 0.1826	
Refinement method	Full-matrix least-squares on F^2	
Data / restraints / parameters	2400 / 0 / 87	
Goodness-of-fit on F^2	1.192	
Final R indices [I>2sigma(I)]	R1 = 0.0499, wR2 = 0.1337	
R indices (all data)	R1 = 0.0534, wR2 = 0.1378	
Extinction coefficient	n/a	
Largest diff. peak and hole	1.444 and -0.559 $e.Å^{-3}$	

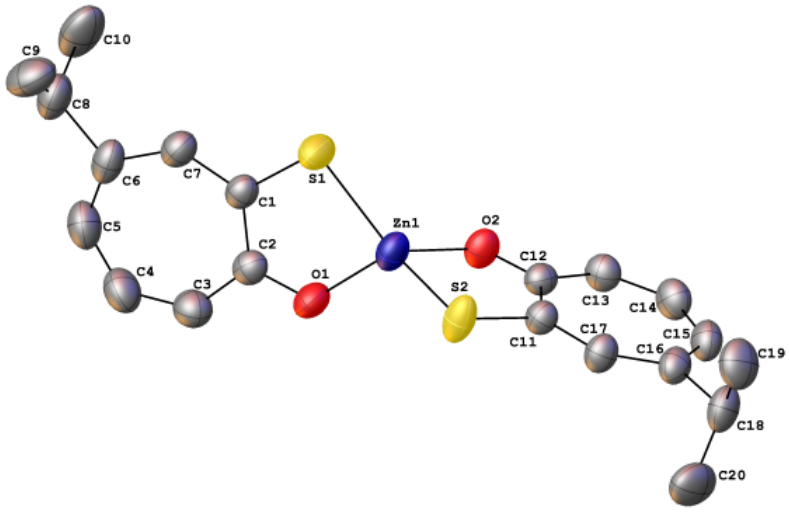

Figure D.6: Molecular structure of Zn(**L2**)$_2$ as determined by X-Ray Diffraction with H-atoms omitted for clarity.

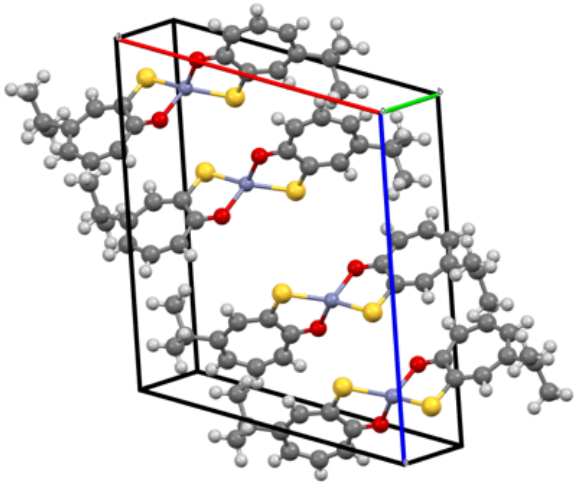

Figure D.7: Crystal packing of Zn(**L2**)$_2$ as determined by X-Ray Diffraction. Image generated using Mercury.

Identification code	znshk2	
Empirical formula	C20 H22 O2 S2 Zn	
Formula weight	423.86	
Temperature	110.0 K	
Wavelength	0.71073 Å	
Crystal system	Monoclinic	
Space group	P 1 21/n 1	
Unit cell dimensions	a = 12.4848(14) Å	α= 90°.
	b = 10.5019(12) Å	β= 108.319(4)°.
	c = 15.6976(19) Å	γ = 90°.
Volume	1953.9(4) $Å^3$	
Z	4	
Density (calculated)	1.441 Mg/m^3	
Absorption coefficient	1.481 mm^{-1}	
F(000)	880	
Crystal size	0.487 x 0.044 x 0.031 mm^3	
Theta range for data collection	2.373 to 27.656°.	
Index ranges	-16<=h<=16, -13<=k<=13, -20<=l<=20	
Reflections collected	47157	
Independent reflections	4541 [R(int) = 0.0442]	
Completeness to theta = 25.242°	99.7 %	
Absorption correction	Semi-empirical from equivalents	
Max. and min. transmission	0.4305 and 0.3490	
Refinement method	Full-matrix least-squares on F^2	
Data / restraints / parameters	4541 / 0 / 230	
Goodness-of-fit on F^2	1.024	
Final R indices [I>2sigma(I)]	R1 = 0.0365, wR2 = 0.0881	
R indices (all data)	R1 = 0.0572, wR2 = 0.1016	
Extinction coefficient	n/a	
Largest diff. peak and hole	0.710 and -0.300 $e.Å^{-3}$	

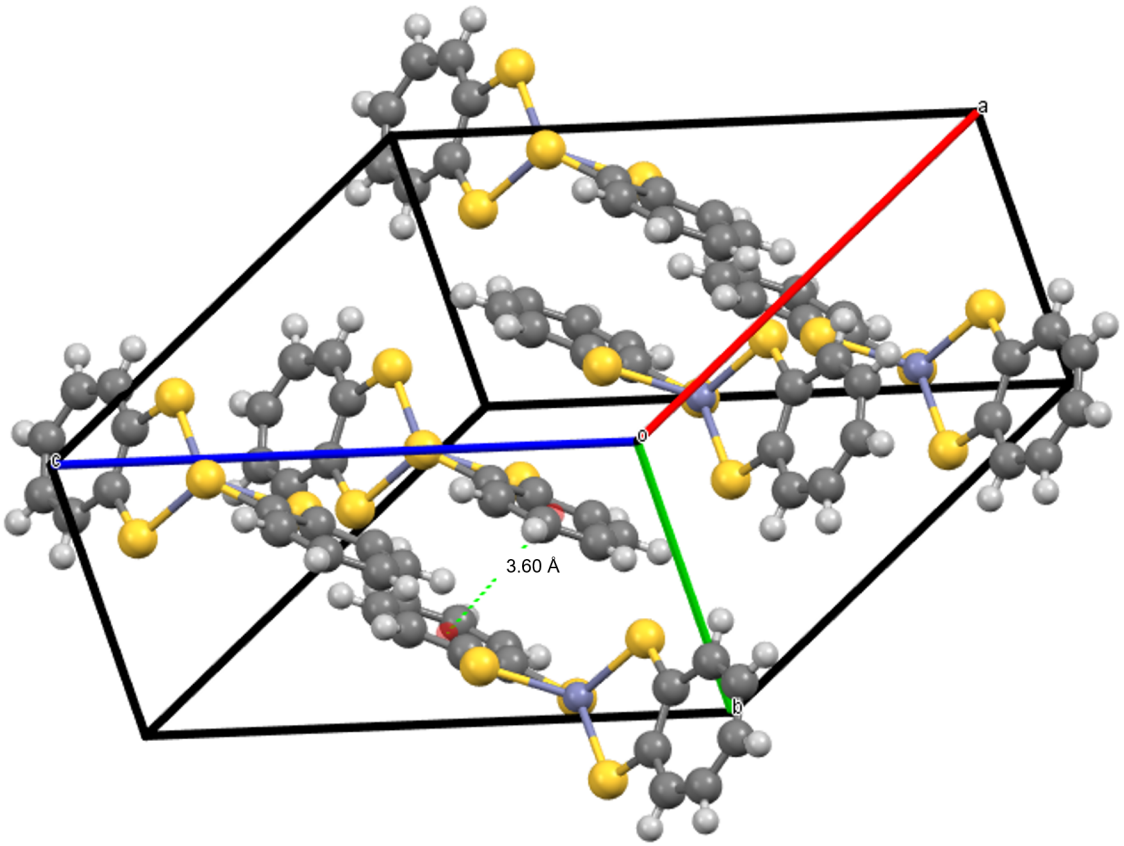

Figure D.8: Crystal packing of Zn(**L4**)$_2$ as determined by X-Ray Diffraction. π-centroids are used to visualize π-π stacking interactions present in the solid-state. Image generated using Mercury

Identification code	cdzn2l4	
Empirical formula	C14 H10 S4 Zn	
Formula weight	371.83	
Temperature	110.0 K	
Wavelength	0.71073 Å	
Crystal system	Monoclinic	
Space group	C 1 2/c 1	
Unit cell dimensions	a = 13.2383(3) Å	α= 90°.
	b = 7.4060(2) Å	β= 105.1910(10)°.
	c = 14.8269(3) Å	γ = 90°.
Volume	1402.88(6) $Å^3$	
Z	4	
Density (calculated)	1.760 Mg/m^3	
Absorption coefficient	2.325 mm^{-1}	
F(000)	752	
Crystal size	0.389 x 0.253 x 0.207 mm^3	
Theta range for data collection	2.847 to 30.513°.	
Index ranges	-18<=h<=18, -10<=k<=10, -21<=l<=21	
Reflections collected	19973	
Independent reflections	2126 [R(int) = 0.0300]	
Completeness to theta = 25.242°	99.4 %	
Absorption correction	Semi-empirical from equivalents	
Max. and min. transmission	0.2657 and 0.1399	
Refinement method	Full-matrix least-squares on F^2	
Data / restraints / parameters	2126 / 0 / 87	
Goodness-of-fit on F^2	1.075	
Final R indices [I>2sigma(I)]	R1 = 0.0222, wR2 = 0.0503	
R indices (all data)	R1 = 0.0237, wR2 = 0.0509	
Extinction coefficient	n/a	
Largest diff. peak and hole	0.607 and -0.518 $e.Å^{-3}$	

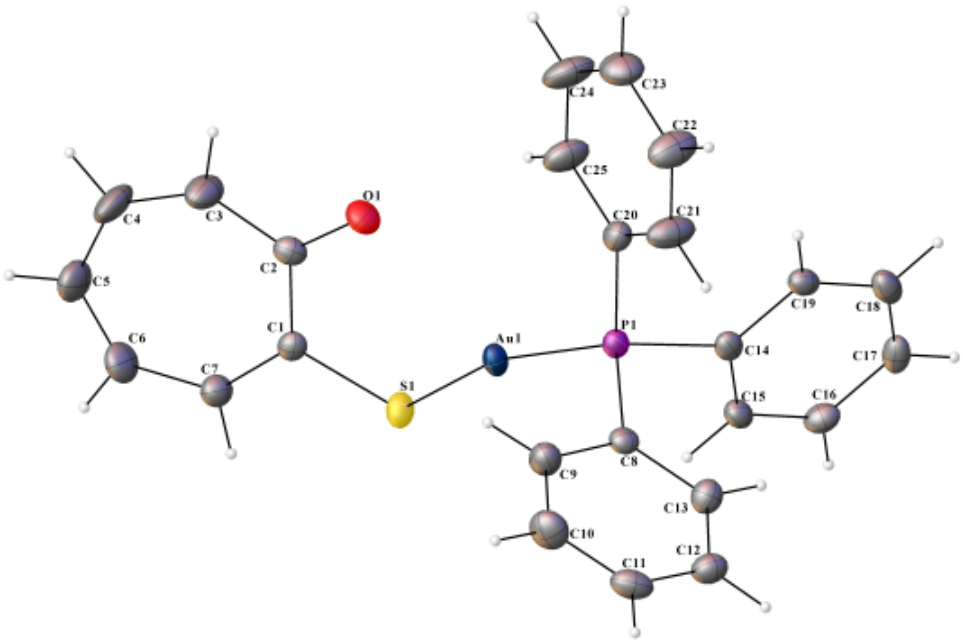

Figure D.9: Molecular structure of $Au(PPh_3)$(**L1**) as determined by X-Ray Diffraction.

Identification code	aupph3l1	
Empirical formula	C25 H20 Au O P S	
Formula weight	596.41	
Temperature	110.0 K	
Wavelength	0.71073 Å	
Crystal system	Triclinic	
Space group	P-1	
Unit cell dimensions	a = 11.2207(9) Å	α= 67.416(2)°.
	b = 13.5830(10) Å	β= 76.003(3)°.
	c = 15.5109(12) Å	γ = 88.799(3)°.
Volume	2111.1(3) $Å^3$	
Z	4	
Density (calculated)	1.876 Mg/m^3	
Absorption coefficient	7.157 mm^{-1}	
F(000)	1152	
Crystal size	0.142 x 0.082 x 0.037 mm^3	
Theta range for data collection	2.070 to 27.620°.	
Index ranges	-14<=h<=14, -17<=k<=17, -20<=l<=20	
Reflections collected	98958	
Independent reflections	9759 [R(int) = 0.0755]	
Completeness to theta = 25.242°	99.9 %	
Absorption correction	Semi-empirical from equivalents	
Max. and min. transmission	0.3169 and 0.2375	
Refinement method	Full-matrix least-squares on F^2	
Data / restraints / parameters	9759 / 0 / 523	
Goodness-of-fit on F^2	1.076	
Final R indices [I>2sigma(I)]	R1 = 0.0283, wR2 = 0.0499	
R indices (all data)	R1 = 0.0415, wR2 = 0.0538	
Extinction coefficient	n/a	
Largest diff. peak and hole	1.068 and -0.828 $e.Å^{-3}$	

APPENDIX E

INHIBITION CURVES

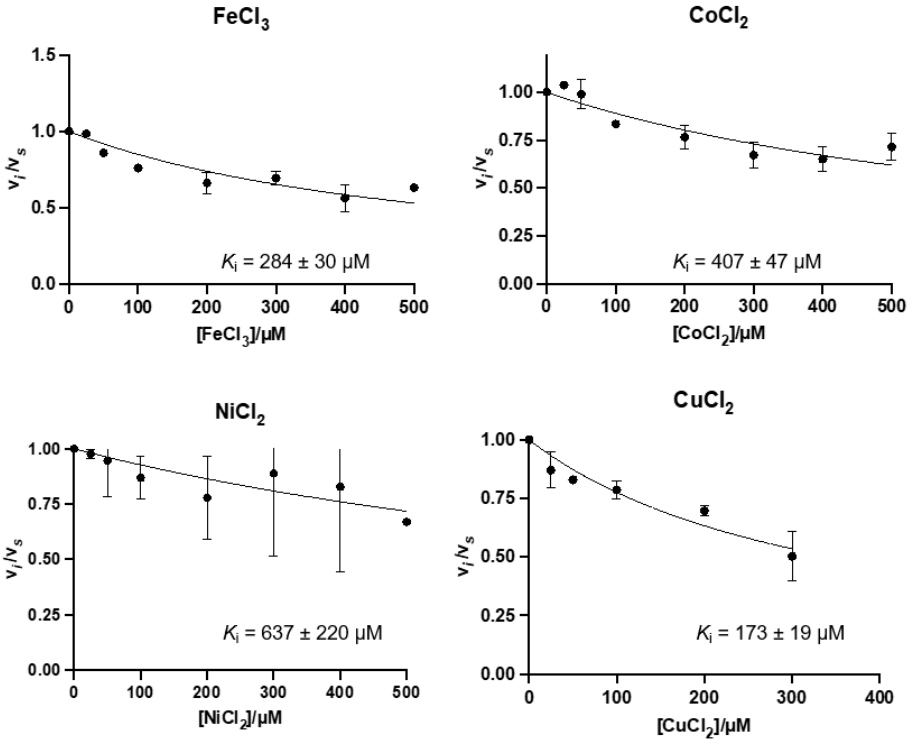

Figure E.1: Kinetic analysis of $FeCl_3$, $CoCl_2$, $NiCl_2$, and $CuCl_2$ against $SC2M^{pro}$ from Chapter IV.

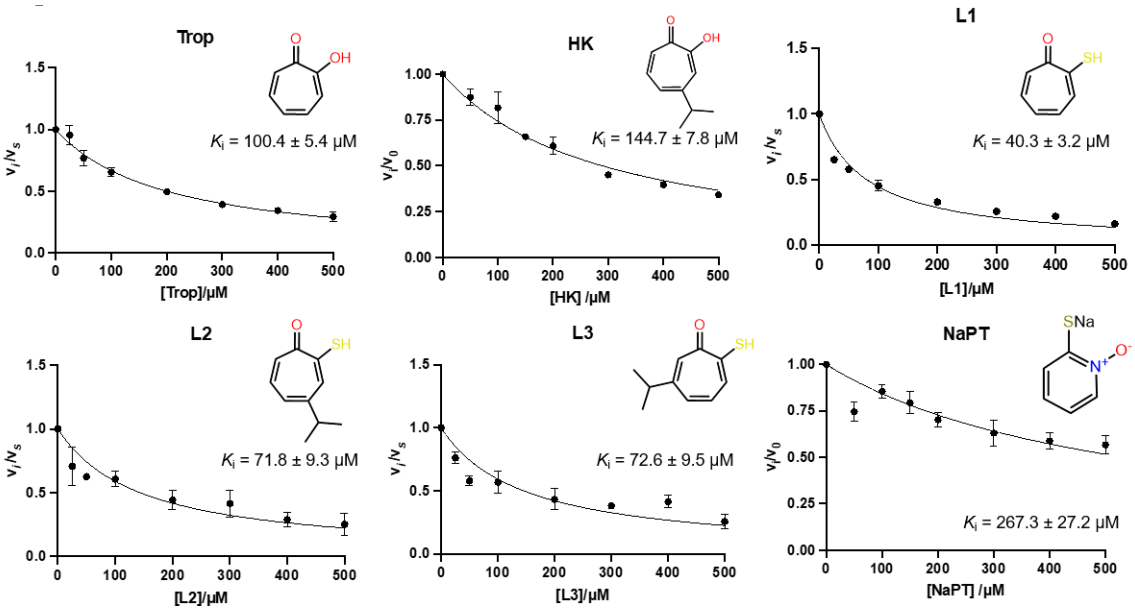

Figure E.2: Kinetic analysis of tropolone, hinokitiol, **L1**, **L2**, **L3**, and sodium pyrithione against SC2M^{pro} from Chapter IV.

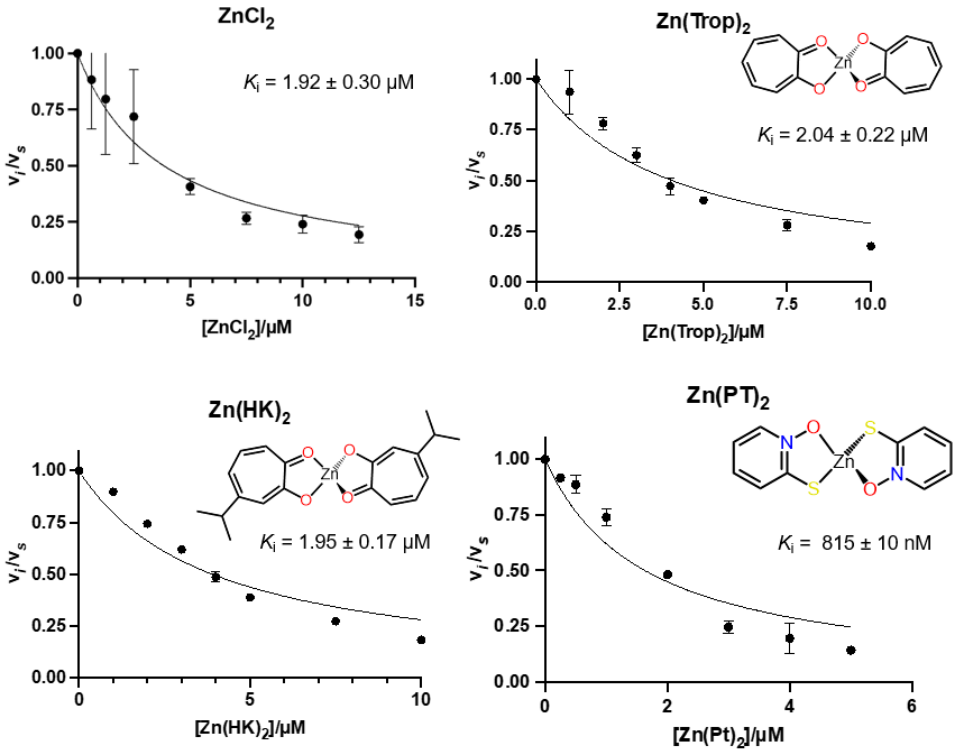

Figure E.3: Kinetic analysis of $Zn(Cl)_2$, $Zn(trop)_2$, $Zn(HK)_2$, and $Zn(PT)_2$ against SC2M^{pro} from Chapter IV.

APPENDIX F

SUPPLEMENTARY TABLES

Compound	λ_{max} (nm)	ϵ ($M^{-1}cm^{-1}$)	λ_{max} (nm)	ϵ ($M^{-1}cm^{-1}$)
L1	269	11249	422	8813
Zn(**L1**)$_2$	267	32326	416	27800
L2	275	23487	421	15194
Zn(**L2**)$_2$	277	43004	413	30188

Table F.1: Summary of UV-Vis absorbance features of **L1**, **L2**, Zn(**L1**)$_2$ and Zn(**L2**)$_2$ in DCM from Chapter III.

Compound	K_i (μM)
Trop	100 ± 5
HK	144.7 ± 7.8
PT	267.3 ± 27.2
L1	40.2 ± 3.2
L2	71.8 ± 9.3
L3	72.6 ± 9.5

Table F.2: Table Summarizing the K_i values for the Ligands tested in Chapter IV.

Compound	K_i (μM)
$FeCl_3$	284 ± 30
$CoCl_2$	407 ± 47
$NiCl_2$	637 ± 220
$CuCl_2$	173 ± 19
$ZnCl_2$	1.92 ± 0.30

Table F.3: Table Summarizing the K_i values for the MCl_x salts tested in Chapter IV.

Compound	K_i (μM)	Coordination Mode
$Zn(Trop)_2$	2.04 ± 0.22	O4
$Zn(HK)_2$	1.95 ± 0.17	O4
$Zn(PT)_2$	0.82 ± 0.10	S2O2
$Zn(\mathbf{L1})_2$	0.43 ± 0.04	S2O2
$Zn(\mathbf{L2})_2$	0.90 ± 0.09	S2O2
$Zn(\mathbf{L3})_2$	0.85 ± 0.19	S2O2
$Zn(\mathbf{L4})_2$	40.6 ± 3.4	S4

Table F.4: Table Summarizing the K_i values for the zinc complexes investigated in Chapter IV.

Compound	K_i (μM)
$Fe(\mathbf{L1})_3$	30.0 ± 2.2
$Co(\mathbf{L1})_3$	52.6 ± 4.2
$Ni(\mathbf{L1})_2$	72.4 ± 9.4
$Cu(\mathbf{L1})_2$	65.8 ± 7.9

Table F.5: Table Summarizing the K_i values for the non-Zn Metal-**L1** complexes tested in Chapter IV.

Compound	K_i (μM)
TG	NA
TGTA	NA
$NaNO_2$	NA
TG-DNIC	33 ± 2
TGTA-DNIC	38 ± 2

Table F.6: Table Summarizing the K_i values for the DNIC complexes and the associated controls investigated in Chapter IV.

Solvent	δ (ppm)	r_H (Å)	δ (ppm)	r_H (Å)	$r_{H\ avg}$ (Å)
D_2O	2.81	4.39 ± 0.08	2.25	4.00 ± 0.05	4.20 ± 0.07
CD_2Cl_2	3.34	3.35 ± 0.10	2.10	4.35 ± 0.06	3.35 ± 0.08

Table F.7: Summary of ^{1}H NMR DOSY results of [**Ni-I**]^0 in D_2O and CD_2Cl_2 from Chapter V. Hydrodynamic radius (r_H) derived from experimentally determined diffusional coefficients (D) using the Stokes-Einstein Equation.